Universität Hamburg
DER FORSCHUNG | DER LEHRE | DER BILDUNG

FAKULTÄT
FÜR MATHEMATIK, INFORMATIK
UND NATURWISSENSCHAFTEN

PHOTONICALLY REFERENCED MICROWAVE SIGNAL SYNTHESIS FOR HIGH-PRECISION TIMING AND FREQUENCY APPLICATIONS

Dissertation

zur Erlangung des Doktorgrades
an der Fakultät für Mathematik, Informatik und Naturwissenschaften
Fachbereich Physik
der Universität Hamburg

vorgelegt von

Erwin Agustin Cano Vargas

B.Sc. in Electronics and Telecommunications Engineering, Universidad Autonoma del Caribe, 2009
M.Sc. in Microelectronics and Microsystems, Technische Universität Hamburg, 2018

Hamburg, Februar 2025

Gutachter der Dissertation: Prof. Dr. Franz Kärtner
Prof. Dr. Tobias Herr

Zusammensetzung der Prüfungskommission: Prof. Dr. Franz Kärtner
Prof. Dr. Tobias Herr
Prof. Dr. Oliver Gerberding
Prof. Dr. Ralf Riedinger
Prof. Dr. Daniela Pfannkuche

Vorsitzende der Prüfungskommission: Prof. Dr. Daniela Pfannkuche

Datum der Disputation: 23.04.2025

Vorsitzender Fach-Promotionsausschusses Physik: Prof. Dr. Wolfgang J. Parak
Leiter des Fachbereichs Physik: Prof. Dr. Markus Drescher
Dekan der Fakultät MIN: Prof. Dr.-Ing. Norbert Ritter

EIDESSTATTLICHE VERSICHERUNG

Hiermit versichere ich an Eides statt, die vorliegende Dissertationsschrift selbst verfasst und keine anderen als die angegebenen Hilfsmittel und Quellen benutzt zu haben. Sofern im Zuge der Erstellung der vorliegenden Dissertationsschrift generative Künstliche Intelligenz (gKI)-basierte elektronische Hilfsmittel verwendet wurden, versichere ich, dass meine eigene Leistung im Vordergrund stand und dass eine vollständige Dokumentation aller verwendeten Hilfsmittel gemäß der Guten wissenschaftlichen Praxis vorliegt. Ich trage die Verantwortung für eventuell durch die gKI generierte fehlerhafte oder verzerrte Inhalte, fehlerhafte Referenzen, Verstöße gegen das Datenschutz- und Urheberrecht oder Plagiate.

Hamburg, den 01. Februar 2025.

ERWIN CANO VARGAS

Erwin Agustin Cano Vargas

SUMMARY

Ultra-stable microwave signals are essential for a variety of high-precision applications, including time and frequency metrology, large-scale photon science facilities, global navigation satellite systems, and quantum computing. Traditional electronic oscillators face inherent limitations in phase noise performance and long-term stability. This dissertation explores the photonic approaches to generate ultra-stable microwave signals leveraging mode-locked lasers and pure optical reference modules to achieve unprecedented frequency stability and phase noise performance.

This dissertation provides a comprehensive study of photonic timing instrumentation and microwave synthesis, detailing key components, measurement techniques, and system-level innovations. It then presents the design and experimental implementation of a certain specific photonic microwave oscillator architecture named PRESTO, which incorporates a fiber delay line for self-referencing and stabilization. A feedback control system is introduced to suppress phase noise and improve frequency stability. Experimental validation of PRESTO demonstrates a significant reduction in the phase noise of the output microwave signal, achieving integrated timing jitter of less than 30 fs down to 1 Hz.

The findings of this research demonstrate that PRESTO is a promising solution for next-generation photonic microwave oscillators, offering superior stability and spectral purity. The first lab prototype exhibits an outstanding phase noise performance comparable to other state-of-the-art photonic microwave oscillators, including the optical frequency division methods and delay-line based oscillators with opportunities for further advancements in this field.

ZUSAMMENFASSUNG

Ultrastabile Mikrowellensignale sind für eine Vielzahl von Hochpräzisionsanwendungen unerlässlich, z. B. für die Zeit- und Frequenzmetrologie, Großforschungseinrichtungen, globale Satellitennavigationssysteme und Quantencomputer. Herkömmliche elektronische Oszillatoren unterliegen in Bezug auf das Phasenrauschen und die Langzeitstabilität inhärenten Beschränkungen. In dieser Dissertation werden photonische Methoden zur Erzeugung ultrastabiler Mikrowellensignale untersucht, bei denen modengekoppelte Laser und rein optische Referenzmodule eingesetzt werden, um eine hohe Frequenzstabilität und niedriges Phasenrauschen zu erreichen.

Diese Dissertation bietet eine umfassende Studie über photonische Timing-Instrumente und Mikrowellensynthese, wobei Schlüsselkomponenten, Messverfahren und Innovationen auf Systemebene detailliert beschrieben werden. Anschließend wird der Entwurf und die experimentelle Umsetzung einer bestimmten photonischen Mikrowellenoszillatorarchitektur namens PRESTO vorgestellt, die eine Faserverzögerungsleitung zur Selbstreferenzierung und Stabilisierung enthält. Ein rückgekoppeltes Kontrollsystem wird eingeführt, um das Phasenrauschen zu unterdrücken und die Frequenzstabilität zu verbessern. Die experimentelle Validierung von PRESTO zeigt eine signifikante Verringerung des Phasenrauschens des Mikrowellenausgangssignals, wobei ein integrierter Timing-Jitter von weniger als 30 fs bis zu 1 Hz erreicht wird.

Die Ergebnisse dieser Forschung zeigen, dass PRESTO eine vielversprechende Lösung für Mikrowellenoszillatoren der nächsten Generation ist, die eine überlegene Stabilität und spektrale Reinheit bietet. Der erste Laborprototyp zeigt ein hervorragendes Phasenrauschen, das mit dem anderer moderner photonischer Mikrowellenoszillatoren vergleichbar ist, einschließlich optischer Frequenzteilungsmethoden, und bietet Möglichkeiten für weitere Fortschritte in diesem Bereich.

FOREWORD AND ACKNOWLEDGEMENTS

'We inhabit time as fish live in water. Our being is indivisible from time. Time is not something that passes, it is something we are made of.' – Carlo Rovelli, The Order of Time [1]

Time is an elusive entity, both an enigma and a construct that we navigate daily. Sometimes, I am acutely aware of it, feeling its relentless pressure dictating deadlines, structuring progress, and measuring achievements. At other times, it fades into the background, an abstraction that's hard to grasp when moments slip by unnoticed. The whole process of working on this dissertation has been interwoven with these two faces of time, much as my journey through academia: one face of discipline, rigor, and structured effort; and the other, waiting, uncertainty, and fluidity.

This journey was a lengthy process, partly reflecting the complexities of the research issue at hand but also reflecting the burdens of trying to balance both life and bureaucratic aspects of academic procedures. But through long hours of experimentation, periods of self-doubt, and stretches of waiting, there was one constant in the resolve to move forward. Where often it seemed like time was my adversary, perseverance and the enduring support of loved ones allowed me finally to arrive at this point.

Let me say that this is not my work alone, but it is standing on the shoulders of the people who kept me going during this journey. I am especially grateful to my advisor Franz Kärtner for guidance, patience, and insight during the shaping phases of this research. I'm also deeply thankful to my colleagues at Cycle GmbH and mentors Kemal Şafak and Anan Dai, for both introducing me and training me in the world of optics and helping me throughout the full completion of this work. To my colleagues in the UFOX group who provided intellectual discourse and encouragement along the way, special shoutouts to my former officemate Elias, which make this process more sane throughout insanity, Miguel for always keeping the laughs, Fabian for keeping the party going, Marvin for keeping me company in the lab and helping me out with fiber technology and to Lu, Igor, Anchita, Kathinka, Anna who encouraged me along the way, and with many others which I shared coffees, stories and laughter. To all the remarkable scientific colleagues with whom I have engaged in stimulating discussions and shared memorable moments at conferences and collaborative events around the world, your insights and camaraderie have enriched my journey and filled me with hope for our global future. I am also particularly grateful for the administrative support of Uta Freydank.

I would also like to acknowledge the generous financial support by DESY and the Deutsche Forschungsgemeinschaft (DFG), and PIER Graduate School, which made this research possible. Their funding and resources played a crucial role in the successful completion of this work.

I am eternally grateful to my friends, who provided laughter and perspective when the burden of research seemed unbearable. Carlos and Juan Felipe for being my sidekicks in the streets, my gym buddy Julien for being my motivation to train, Olga, Alma, Carlos and Laura for keeping the gossip flowing and my heart guarded, and so many more that if I would just write about every single one of them, and all our stories, then this thesis would be at least 200 pages of acknowledgement and anecdotes.

The biggest acknowledgment to my family: my parents Agustin and Nancy, whose belief in me never wavered and who helped sustain my motivation. To Lennart for being my pillar throughout this time and welcoming me to his family with open arms in Germany. To my nieces and nephews who I always aimed to serve as inspiration for achieving bigger and greater things in life. To my brothers and sisters Mario, Vladimir, Agustin, Luisa, Diana and Natali, which I keep always in my heart. Finally, to my grandma Elizabeth, from which I inherited the will to pursue knowledge and the passion for academia, and to my brother Cosme, who helped shape this little kid's path into the adult I am right now, it is painfully sad I no longer can share this moment with you, but your legacy lives on with me.

CONTENTS

Eidesstattliche Versicherung i

Summary ii

Zusammenfassung iii

Foreword and Acknowledgements iv

Contents vi

List of Publications x

List of Figures xii

List of Tables xvi

List of Abbreviations xvii

1. Introduction 1
   - 1.1. A Brief Travel Through Time (Keeping) 1
   - 1.2. Photonic Microwave Oscillators based on CW Lasers 4
     - 1.2.1. Optoelectronic Oscillators 5
     - 1.2.2. Microcombs 8
     - 1.2.3. Electro-Optical Combs 9
   - 1.3. Photonic Microwave Oscillators based on MLLs 10
   - 1.4. Motivation for Photonic Microwave Oscillators 14
     - 1.4.1. Time and Frequency Metrology 14
     - 1.4.2. Large Photon Science Facilities 15
     - 1.4.3. Space Applications 15
     - 1.4.4. Radar Systems 16

1.4.5. Quantum Computing 16

1.5. Scope of the Dissertation 17

2. Timing Characterization Toolbox 18

2.1. Balanced Optical Cross-Correlator 18

2.1.1. Free-Space Bulk Optics BOC 20

2.1.2. Integrated Waveguide-based BOC 21

2.1.3. Timing Sensitivity Characterization 23

2.1.4. Noise Floor Characterization 25

2.2. Balanced Optical Microwave Phase Detector 27

2.2.1. Operation Principle 28

2.2.2. Timing Sensitivity Characterization 33

2.2.3. Noise Floor Characterization 35

2.2.4. Residual Timing Jitter Characterization 36

3. Mode-Locked Laser Characterization and Microwave Synthesis 38

3.1. Timing Jitter Characterization of Mode-Locked Lasers 38

3.1.1. Microwave Phase Detection upon Photodetection Method 39

3.1.2. Optical Timing Detection Method 41

3.1.3. Optical Delay-Line Method 46

3.1.4. Optical Timing Jitter Methods Compared 47

3.2. Microwave Synthesis from Mode-Locked Lasers 49

3.2.1. Photodiodes 49

3.2.2. Photodetection of Ultrashort Optical Pulses 52

3.2.3. Noise Sources during Photodetection 56

3.2.4. AM-PM Conversion 60

3.2.5. Photodiode Types ... 61

3.2.6. Photodiodes under Test ... 63

4. Photonically Referenced Extremely Stable Oscillator (PRESTO) ... 69

4.1. PRESTO: Concept and Design ... 70

4.1.1. Feedback Loop Model ... 71

4.1.2. Fiber Delay-Line Reference ... 79

4.2. PRESTO: Implementation and Experimental Results ... 88

4.2.1. Experimental Setup ... 88

4.2.2. Experimental Setup 2.0 ... 93

4.2.3. Microwave Relative Timing Jitter to the Laser Source ... 97

5. Conclusions and Outlook ... 100

5.1 Summary of Research and Key Findings ... 100

5.2 Comparative Analysis and Impact of PRESTO ... 101

5.3 Outlook ... 102

5.4 Concluding Remarks ... 104

Appendix: Phase Noise and Stability in Oscillators ... 105

A.1. Phase Noise and Timing Jitter ... 105

A.2. Phase Noise Instrumentation for Microwave Oscillators ... 109

A.3. Signal Source Analyzer: R&S®FSWP ... 109

A.3.1. Principle of Operation ... 110

A.3.2. R&S®FSWP: Phase Noise Specifications ... 111

Appendix: Insights on Mode-Locked Lasers for PRESTO ... 113

B.1. Noise in Mode-Locked Lasers ... 113

B.1.1. Quantum Noise and Spontaneous Emission ... 113

B.1.2. Timing Jitter and Gordon-Haus Effect 114

B.1.3. Frequency Pulling and Repetition Rate Stability 115

B.1.4. Optical Phase Noise and the Kramers-Kronig Relations 115

B.1.5. Environmental and Thermal Effects 115

B.1.6. Offset and Repetition Frequency Control 116

B.1.7. Noise Suppression Techniques 116

B.2. Mode-Locked Laser Characteristics 117

B.2.1. MENHIR-1550 (SN 4409001) 117

B.2.2. MENHIR-1550 (SN 4409002) 118

Bibliography 119

LIST OF PUBLICATIONS

PUBLICATIONS IN REFEREED JOURNALS

1. Kemal Şafak, Erwin Cano Vargas, Anan Dai, Marvin Edelmann, Florian Emaury, Karolis Balskus, Benjamin Rudin, Philip Battle, Tony D. Roberts, Bradley Slezak, Todd Hawthorne, and Franz X. Kärtner, "Photonically referenced extremely stable oscillator," *Optics Letters* 49, 977-980, 2024
2. Marvin Edelmann, Malek M. Sedigheh, Yi Hua, Erwin Cano Vargas, Mikhail Pergament, and Franz X. Kärtner, "Large-mode-area soliton fiber oscillator mode-locked using NPE in an all-PM self-stabilized interferometer," *Applied Optics* 62, 2023

PROCEEDINGS OF REFEREED CONFERENCES

1. K. Şafak, et al., "Optical-to-microwave clock synchronization with few-femtosecond residual timing jitter for space ground segments", *Proc. SPIE 13100, Advances in Optical and Mechanical Technologies for Telescopes and Instrumentation* VI, 131002K, 2024
2. E. Cano Vargas et al., "Low Noise Photonic Microwave Oscillator Based on a Novel Repetition Rate Stabilization," *2023 Joint Conference of the European Frequency and Time Forum and IEEE International Frequency Control Symposium (EFTF/IFCS)*, Toyama, Japan, 2023
3. E. Cano Vargas et al., "Photonic Microwave Oscillator based on Fiber Delay Stabilization using a Waveguide Balanced Cross-Correlator," in *Conference on Lasers and Electro-Optics 2023*, Technical Digest Series, 2023
4. K. Şafak et al., “Balanced Optical-Microwave Phase Detector for 800-nm Pulsed Lasers with Sub-Femtosecond Resolution,” *Proceedings of the 39th Free Electron Laser Conference*, vol. FEL2019, p. 3 pages, 2019
5. E. Cano Vargas et al., “Timing Stability Comparison Study of RF Synthesis Techniques,” *Proceedings of the 39th Free Electron Laser Conference*, vol. FEL2019, p. 3 pages, 2019
6. K. Şafak et al., "Single-Mode Fiber Based Pulsed-Optical Timing Link with Few-Femtosecond Precision in SwissFEL," in *Conference on Lasers and Electro-Optics*, OSA, 2019

7. H. P. H. Cheng et al., "Commissioning of a Fully Automated, Pulsed Optical Timing Distribution System at Dalian Coherent Light Source," *in Conference on Lasers and Electro-Optics*, OSA, 2018
8. K. Şafak et al., "Large-Scale Turnkey Timing Distribution System for Attosecond Photon Science Facilities," in *Conference on Lasers and Electro-Optics*, San Jose, California: OSA, 2017

AWARDS

1. Best Student Paper Competition Winner in 2023 Joint Conference of the IEEE International Frequency Control Symposium and the European Frequency and Time Forum, received for the conference paper, poster and presentation "Low Noise Photonic Microwave Oscillator Based on a Novel Repetition Rate Stabilization ".

LIST OF FIGURES

Figure 1-1. A millennium-long progression of timekeeping methods and mechanisms throughout history. 2
Figure 1-2. Basic feedback loop for frequency-stabilized oscillators.......... 4
Figure 1-3. Conceptual overview of the components inside a photonic microwave oscillator. 5
Figure 1-4. Basic Concept of the Optoelectronic Oscillator (OEO). 6
Figure 1-5. Single-sideband phase noise of a 10 GHz OEO.......... 6
Figure 1-6. Single side band Phase Noise from COEO and Dual-Delay OEO. 7
Figure 1-7. General representation of microcomb generation from a CW laser-driven microresonator. 8
Figure 1-8. Single side-band phase noise scaled to 10 GHz of a free-running 20 GHz microcomb. 9
Figure 1-9. (a) Architecture of electro-optical frequency division (eOFD) based on dual laser reference electro-optical frequency comb, (b) single side band phase noise achieved by this technique. 10
Figure 1-10. Ultra-short pulses generation inside a mode-locked laser cavity. 11
Figure 1-11. Time and frequency domain representation of the pulse train generated by a mode-locked laser. 11
Figure 1-12. Optical frequency comb as a clockwork bridge between optical and microwave domains. 12
Figure 1-13. Optical frequency division from optical cavities using an optical frequency comb from a MLL.......... 13
Figure 2-1. Principle of timing detection using a Balanced Optical Cross-Correlator (BOC). 19
Figure 2-2. Free-space type-II second harmonic generation BOC for 1550nm optical pulses..... 20
Figure 2-3. Fiber-coupled waveguide-based BOC for 1550nm optical pulses. 22
Figure 2-4. Physical implementations of the BOC with size comparisons.......... 23
Figure 2-5. BOC sensitivity characterization experimental setup. 24

Figure 2-6. Timing sensitivity comparison between bulk BOC and waveguide BOC using a OneFive 216.66 MHz mode-locked laser. S-curve traces at the output of (a) the waveguide BOC and (b) the bulk BOC. (c) Responses when scaled together. 25
Figure 2-7. Jitter Spectral Density corresponding to the electronic noise floor of the Waveguide BOC. 25
Figure 2-8. Operation of the balanced-optical microwave phase detector. 29
Figure 2-9. BOMPD setup operating as an optoelectronic PLL for RF synthesis with VCO. 30
Figure 2-10. Operation principles of the BOMPD and Sagnac Loop Interferometer (SGI). 31
Figure 2-11. Timing sensitivity characterization for the BOMPD. 34
Figure 2-12. Measured BOMPD timing sensitivity at different microwave frequencies. 35
Figure 2-13. Measured BOMPD noise floor scaled at different microwave frequencies. 36
Figure 2-14. Measured residual timing jitter between the optical and RF signals at different frequencies. 37
Figure 3-1. Schematic representation of direct phase noise measurement. 39
Figure 3-2. Noise floor for phase noise measurement using the R&S® FSWP Signal Source Analyzer at various carrier frequencies. 40
Figure 3-3. Experimental setup for phase noise measurement using a BOC as a timing detector with two synchronized mode-locked lasers. 41
Figure 3-4. Feedback loop model for laser synchronization using a BOC as the error signal generator. 42
Figure 3-5. Locking bandwidth dependance on P gain and I frequency corner for the timing jitter characterization of two identical 1 GHz repetition rate mode-locked lasers. 44
Figure 3-6. Measured jitter spectral density and integrated timing jitter for a 1 GHz mode-locked laser characterized using the optical timing detector method. 45
Figure 3-7. Timing jitter measurement setup using delay line phase noise method. 47
Figure 3-8. Measured phase noise spectra of a mode-locked laser at 10 GHz carrier using (i) a commercial phase noise analyzer, (ii) the timing-detector method and (iii) the timing-delay method. 48
Figure 3-9. Photoelectric phenomena (photoeffect) in photodiodes. Modified from [89]. 50
Figure 3-10. I-V characteristics of the photoconductive operation mode on photodiodes, without a load (left) and with a series load in the circuit (right). 51

Figure 3-11. Time and Frequency representation of optical and photodetected pulse trains. 53
Figure 3-12. Noise sources during photodetection. Adapted from [89]. 57
Figure 3-13. Phase noise contributions from different noise sources on a single frequency from a photodetected signal... 59
Figure 3-14. Band diagrams of PIN, DDR and MUTC photodiodes.. 61
Figure 3-15. Photocurrent RF power for the fundamental harmonic frequency at 1 GHz vs. incoming average optical power for PIN and MUTC photodiodes. 64
Figure 3-16. Photocurrent RF power for the 10th harmonic frequency at 10 GHz vs. incoming average optical power for PIN and MUTC photodiodes. 64
Figure 3-17. Optical spectrum of photocurrent pulse for the MUTC photodiode illuminated by a 400 MHz repetition rate mode/locked laser. 66
Figure 3-18. Optical spectrum of photocurrent pulse for the MUTC photodiode illuminated with a 1 GHz repetition rate mode/locked laser. 67
Figure 4-1: General configuration for the Photonically Referenced Extremely Stable Oscillator (PRESTO). 70
Figure 4-2. Integration of spontaneous emission noise over each round-trip in a mode-locked laser. 72
Figure 4-3. Feedback loop model for PRESTO. 72
Figure 4-4. Timing noise written into the timing jitter of the mode-locked laser. 75
Figure 4-5. Feedback loop model from PRESTO with increasing proportional gain of the PI loop controller. 78
Figure 4-6. Fiber optic gyroscope coil element used as fiber-delay line for PRESTO. 80
Figure 4-7. Feedback model simulation for PRESTO for increasing fiber-delay length. 81
Figure 4-8: Single mode fiber length mismatch effects on the timing sensitivity due to dispersion compensation within the fiber delay line. 83
Figure 4-9. Expected Thermal Phase Noise from Fiber Delay Line of 2 km length in PRESTO. 87
Figure 4-10. Schematic of the experimental implementation for PRESTO. 88
Figure 4-11. In-loop timing jitter of the PRESTO setup as a function of increasing feedback loop gain.. 91
Figure 4-12. Characterization of 10 GHz microwave output from PRESTO. 92

Figure 4-13. Schematic of the experimental implementation for PRESTO with a double feedback scheme.. 93
Figure 4-14. In-loop timing jitter of the PRESTO setup for single and dual feedback loop........ 95
Figure 4-15. Characterization of 10 GHz microwave output from PRESTO for Single and Dual Feedback Loop.. 96
Figure 4-16. Out-of-loop optical to microwave timing jitter characterization setup................... 97
Figure 4-17. BOMPD Sensitivity Measurement at the Zero-Crossing from a 100 Hz Beat Note Signal. 98
Figure 4-18.Relative Timing Jitter Measurements from the Photonic Microwave Oscillator in Comparison with the Stabilized Optical Source. 99
Figure 5-1. Comparison of PRESTO's phase noise performance with other photonic microwave oscillators. 102
Figure 5-2. Further implementation of PRESTO in a 6U rack unit... 103
Figure 0-1. Ideal and real representation of a sinusoidal continuous signal in time and frequency 106
Figure 0-2. Phase noise spectrum as function of the offset frequency. 108
Figure 0-3. Phase noise measurement performed by FSWP using cross-correlations. 111
Figure 0-4. Noise floor for phase noise measurement using the R&S®FSWP Signal Source Analyzer at various carrier frequencies. 112
Figure 0-1. Schematic representation of noise sources, coupling mechanisms, and their effects in the timing of mode-locked lasers. 114
Figure 0-2. Mode-locked laser MENHIR-1550 (SN 4409001): (a) Optical power spectrum, (b) pulse shape and duration at the fiber output. 117
Figure 0-3. Mode-locked laser MENHIR-1550 (SN 4409002): (a) Optical power spectrum, (b) pulse shape and duration at the fiber output. 118

LIST OF TABLES

Table 2-1. Integrated RMS Timing Jitter at the balanced photodetector for different offset frequencies and at different bandwidths. 26
Table 4-1. PRESTO feedback loop model parameters for loop gain effects. 76
Table 4-2. SMF parameters used in thermal phase noise model. 86
Table 4-3. Mode-locked laser specifications for PRESTO. 89
Table A-1. Phase noise sensitivity with R&S®FSWP (correlations = 1) for 10 GHz input. 111
Table B-1. Specifications of main MENHIR-1550 laser for PRESTO. 117
Table B-2. Specifications of backup MENHIR-1550 laser for laser characterization. 118

LIST OF ABBREVIATIONS

ALMA	Atacama large millimeter/submillimeter array
AM	Amplitude modulation
ASE	Amplified spontaneous emission
BOC	Balanced optical cross-correlator
BOMPD	Balanced-optical microwave oscillator
BPD	Balanced photodetector
COEO	Coupled optoelectronic oscillator
CW	Continuous wave
DBS	Dichroic beam splitter
DCF	Dispersion-compensating fiber
DDR	Dual-depletion region
EDFA	Erbium-Doped Fiber Amplifier
eOFD	Electro-optical frequency division
EOM	Electro-optical modulator
EOM-PM	Electro-optical phase modulator
FEL	Free-electron laser
FM	Frequency modulation
FOG	Fiber optic gyroscope
FSR	Free spectral range
GNSS	Global navigation satellite systems
GPS	Global positioning system
GVD	Group velocity dispersion
MDL	Motorized delay line stage
MLL	Mode-locked lasers
MUTC	Modified uni-traveling carrier PD
OEO	Optoelectronic oscillator
OFD	Optical frequency division
PBC	Polarization beam combiner
PBS	Polarization beam splitter
PD	Photodiode
PI	Proportional-integral
PIN	p-intrinsic-n photodiodes
PLL	Phase-locked loop
PM	Polarization maintaining
PM	Phase modulation
PMO	Photonic microwave oscillator
PPKTP	Periodically poled potassium titanyl phosphate
PRESTO	Photonically Referenced Extremely Stable Oscillator

PSD	Power spectral density
PZT	Piezoelectric transducer
RF	Radio frequency
RIN	Relative intensity noise
RMS	Root-mean square
SAR	Synthetic aperture radar
SGI	Sagnac interferometer
SH	Second harmonic
SHG	Second harmonic generation
SMF	Single mode fiber
SNR	Signal-to-noise ratio
SPM	Self-phase modulation
SSA	Signal source analyzer
TOC	Thermo-optical coefficient
UTC	Uni-traveling modified carrier PD
VCO	Voltage-controlled oscillator
VLBI	Very long baseline interferometry
WBOC	Waveguide-based BOC
WDM	Wavelength division multiplexer
µC	Microcomb

1. INTRODUCTION

Oscillators are the fundamental building block of precise timing and synchronization systems, which are essential for a wide range of scientific, industrial, and technological applications. From global navigation satellite systems (GNSS) and radio detection and ranging (RADAR) to quantum computing and large-scale photon science facilities, the demand for ultra-stable microwave sources continues to grow. However, traditional electronic oscillators face limitations in achieving the required stability and low phase noise for next-generation systems.

Photonic microwave oscillators (PMOs) offer a compelling alternative by leveraging optical frequency references and ultrafast mode-locked lasers (MLLs) to generate exceptionally stable microwave signals. This dissertation introduces PRESTO (Photonically Referenced Extremely Stable Oscillator), a novel PMO architecture based on a mode-locked laser self-referenced via a fiber delay-line. By further direct photodetection of ultrashort pulses, PRESTO achieves ultra-low phase noise and high spectral purity, bridging the gap between optical and microwave domains.

To contextualize this research, let’s start by exploring the historical evolution of oscillators and timekeeping, from early mechanical systems to modern optical frequency standards. Understanding this progression highlights the motivation behind photonic microwave synthesis and the impact of transferring optical sources stability to the RF domain.

1.1. A BRIEF TRAVEL THROUGH TIME (KEEPING)

Ever since the rise of civilization, human beings have been struggling with understanding and measurement of time, with the realization that it is basic to the structuring of everyday life and technological development. Time has often been regarded as a one-way arrow defining past, present, and future, where its direction emerges from the increase of entropy [1]. Additionally, time has been considered an added dimension of reality, shaping our experience of change and causality [2]. In this work, however, time is viewed from a physical perspective, based on periodic stable oscillations/cycles, enabling precise measurement and synchronization [3].

Figure 1-1. A millennium-long progression of timekeeping methods and mechanisms throughout history. [1]

Time progression from water clocks, sundials, sand clocks, celestial object frequency standards, pendulums, mechanical clocks, quartz crystal clocks, atomic clocks and ultimately optical clocks in the modern time.

Historically, timekeeping was derived from astronomical observations and natural cycles. Early methods were pioneered by ancient civilizations such as the Egyptians and Babylonians; these included sundials to divide daylight into hours and water clocks for measuring short time intervals at night [1]. However, its dependence on the Sun's motion meant that sundials could not function effectively under varying seasonal conditions or diverse geographical locations. The Babylonians developed the sexagesimal or base-60 system that provided the basis for the modern division of an hour into 60 minutes and a minute into 60 seconds [4], which is still followed today. The hours of the day were progressively accommodated to the natural motion of celestial bodies, from Earth's rotation, followed by its rotation around the Sun; both of which were an unreliable long-term standard, due to irregularities in the Earth's rotational speed caused by tidal forces, atmospheric dynamics, seismic activity, and variations in mass distribution within the planet.

As civilizations developed further, the need for more accurate timekeeping became essential for navigation, commerce, and, to some extent, scientific research. The first significant discovery were mechanical clocks, invented in the 13th century, which used escapement mechanisms to regulate time intervals [4]. These devices provided more consistent timekeeping, although with limitations in accuracy. The 17th century saw the development of pendulum clocks, pioneered by Christiaan Huygens, which significantly improved precision, achieving accuracies within seconds per day.

The transition to electronic timekeeping began in 1927 with the invention of the quartz oscillator, which exploited the piezoelectric properties of quartz crystals to achieve far greater stability than mechanical clocks. Quartz clocks reached frequency instabilities as low as 10^{-9}, making them

---

[1] Created with images under CC0 Public Domain license

suitable for scientific and industrial applications. However, environmental conditions and variations in crystal structure introduced limitations in long-term stability [4].

A revolutionary leap in precision came with the advent of atomic clocks in the mid-20th century, which could measure time using the natural oscillations of atomic transitions. First proposed by Lord Kelvin in 1879, this was realized in practice with the cesium-133 atomic clock in 1955. The second was then redefined in 1967 as 9,192,631,770 cycles of the hyperfine transition of cesium-133 [5]. With the frequency instabilities as low as 10^{-16} achieved for current atomic clocks, they became essential for applications such as global positioning systems (GPS), deep-space navigation, and fundamental physics research [6].

Today, the frontier of timekeeping is moving towards optical frequency standards, offering even greater precision than microwave-based atomic clocks. To date, optical lattice clocks based on elements like strontium and ytterbium, have reached instabilities below 10^{-18}, thus opening possibilities for redefining the SI second by 2030 [7]. However, direct counting of optical frequencies, oscillating at rates much higher than those in microwave-based atomic clocks, still represents a challenge. This is overcome by the invention of optical frequency combs, a breakthrough technology that allows direct phase-coherent division of optical frequencies into the microwave domain [8-10]. Combined with optical frequency standards, such frequency combs allow for optical clock systems which outperform state-of-the-art cryogenic microwave atomic clocks [11] even down to instabilities down of 10^{-19} [12-16].

The transition from mechanical to electronic and, ultimately, optical timekeeping technologies represents an exponential improvement in stability and precision. Figure 1-1 illustrates this historical progression, highlighting key innovations through time.

Ultimately, optical clocks, while extraordinarily precise, operate at frequencies too high to be directly utilized in many conventional systems. The ability to transfer the precision of optical clocks into the microwave domain has led to the emergence of photonic microwave oscillators (PMOs), which utilize optical frequency stability to generate ultra-stable microwave signals. By down converting their stability into the microwave range, PMOs can exceed phase noise and stability of more stringent conventional microwave oscillators, enabling a whole dimension in their applications spectrum. The following sections will explore how these technologies are being developed, shaping the future of precision time and frequency distribution.

1.2. PHOTONIC MICROWAVE OSCILLATORS BASED ON CW LASERS

Stand-alone microwave oscillators, despite their ability to achieve low phase noise, are inherently limited by environmental and technical factors that affect their stability. Temperature fluctuations, mechanical vibrations, and electromagnetic interference can introduce signal variations, degrading performance over time. Furthermore, the thermal noise of electronic components imposes a fundamental constraint on phase noise, making it difficult to achieve both low phase noise and high stability simultaneously [17] (see Appendix 1 for a primer on Phase Noise).

In contrast, optical sources exhibit significantly greater stability due to their extremely high-quality factors (Q-factors), given by the inherently high frequencies in the optical domain, combined with very narrow linewidths. Optical resonators can achieve Q-factors exceeding 10^{11} [13], with fractional frequency instabilities falling below 5×10^{-17} at one second [18]—several orders of magnitude better than the best conventional microwave oscillators. Photonic oscillators harness this optical stability to generate highly stable microwave signals by transferring the superior timing characteristics of optical sources to the microwave domain [19].

To achieve high stability, oscillators are often locked to a more stable frequency reference. Figure 1-2 illustrates a basic oscillator stabilization scheme, where an oscillator operating at a frequency ν is referenced to a more stable frequency standard. A frequency interrogation mechanism, for example a phase detector, continuously measures the frequency deviation, providing feedback to actively stabilize the oscillator's frequency and align it to that of the frequency standard reference.

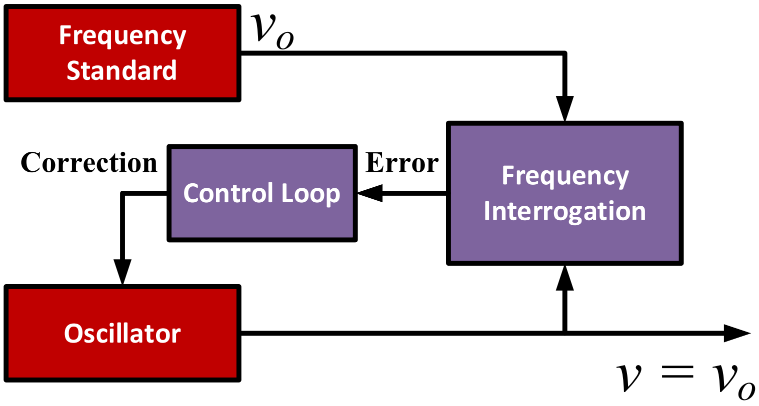

Figure 1-2. Basic feedback loop for frequency-stabilized oscillators.

In PMOs, the main oscillator is an optical source, which is typically stabilized using either an optical resonator cavity or a fiber-optical delay line as a frequency standard [20]. Through optoelectronic conversion, a highly stable microwave signal is synthesized from this optical source, effectively transferring the superior timing stability of the frequency standard into the RF domain. Figure 1-3 illustrates this conceptual overview of PMOs, highlighting the key components involved in this process.

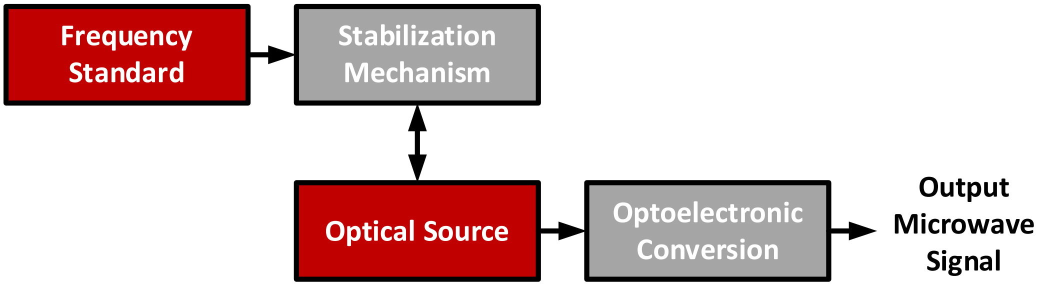

Figure 1-3. Conceptual overview of the components inside a photonic microwave oscillator.

Several PMO architectures exist, differing mainly in their choice of optical source and stabilization method. The next sub-sections will focus on state-of-the-art continuous-wave laser-based PMOs, followed by a detailed discussion of mode-locked lasers and frequency combs, and their critical role in achieving ultra-stable photonic microwave generation.

1.2.1. Optoelectronic Oscillators

Optoelectronic oscillators (OEOs) are a class of PMOs in which a continuous-wave (CW) laser serves as the optical source. OEOs integrate microwave and photonic technologies to generate self-sustained microwave oscillations [19].

Figure 1-4 illustrates the general implementation of an OEO, as initially introduced in [20]. The process begins with light coming from a CW laser passing through an electro-optical modulator, modulating its amplitude. This modulated light is then detected by a photodetector. A critical component in this setup is the long, low-loss fiber delay line, which serves as the reference element and provides a high-quality factor optical storage medium. The electrical signal produced by the photodetector is filtered by a narrow band-pass filter, isolating the desired microwave mode from the detected electrical signal. This is then amplified and fed into the electro-optical modulator, forming a closed optoelectronic feedback loop within the OEO cavity. Microwave oscillations arise when the gain within this loop exceeds its inherent losses, enabling the system to maintain oscillations by converting the filtered noise into a coherent signal.

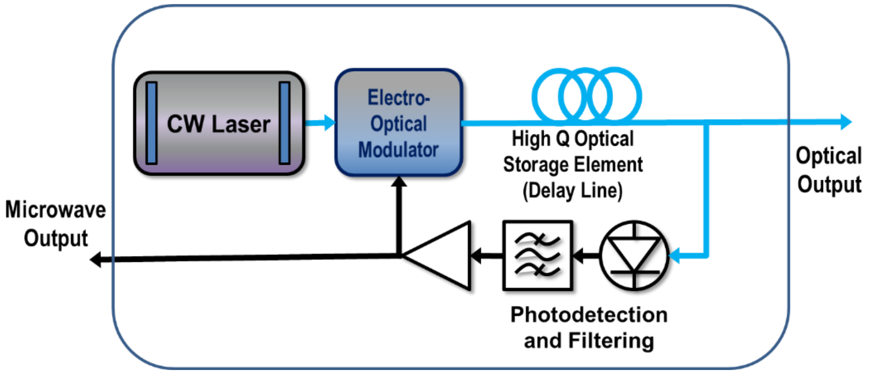

Figure 1-4. Basic Concept of the Optoelectronic Oscillator (OEO).

OEOs can achieve lower phase noise by increasing the length of the fiber delay cavity, but this also reduces the free spectral range (FSR)—meaning the separation between the modes within the cavity—making single-mode selection more challenging [21]. For example, Figure 1-5.a illustrates the phase noise characteristics of an OEO using a 16 km fiber delay line, demonstrating remarkable phase noise in the 10 Hz – 10 kHz range [22]. However, this configuration results in an FSR of approximately 12.8 kHz, which introduces harmonic spurs that degrade the overall spectral purity of the microwave signal, by increasing its phase noise, as depicted in Figure 1-5.b.

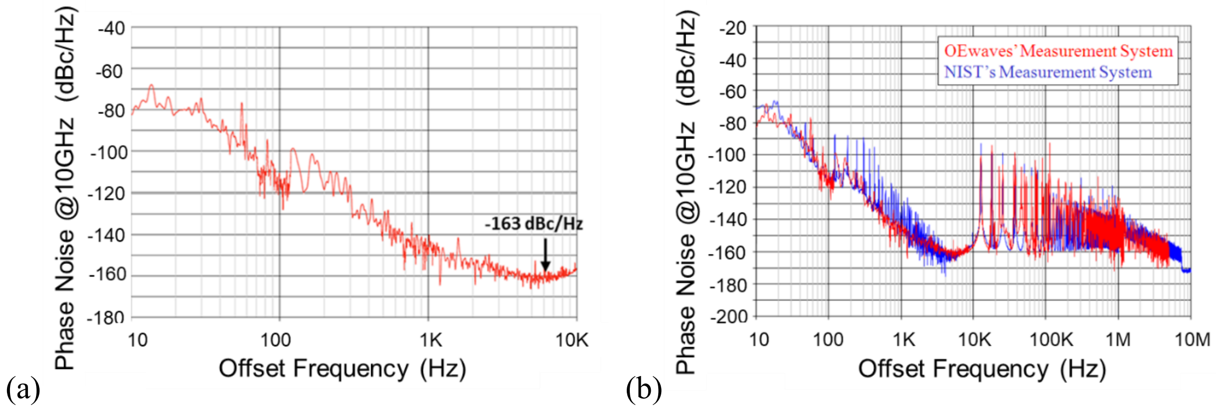

Figure 1-5. Single-sideband phase noise of a 10 GHz OEO.

(a) Demonstrating excellent performance at 10 Hz – 10 kHz offset. (b) Offset frequency from 10 Hz – 10 MHz, depicting free spectral range limitations due to long fiber delay lines, leading to harmonic spurs. Adapted from [22]

This could be ideally surpassed by using a loop filter with a 3 dB bandwidth less than 12.8 kHz for single-mode selection, but creating such a filter is difficult, especially at high center frequencies. For instance, a high-quality electrical filter at 10 GHz typically has a 3 dB bandwidth of 10 MHz. Using such a wider bandwidth filter leads to these unwanted side modes and degrades the spectral purity of the generated signal.

Several modifications to the traditional OEO have been proposed to mitigate the limitations imposed by fiber delay lines. Figure 1-6 presents two significant advancements:

- The Coupled OEO (COEO) which utilizes an optical loop amplification combined with an optoelectronic feedback loop to enhance stability [22].
- Dual-Delay OEO: Incorporates two fiber delay lines (short and long) along with RF injection to improve phase noise while maintaining single-mode operation [23], [24].

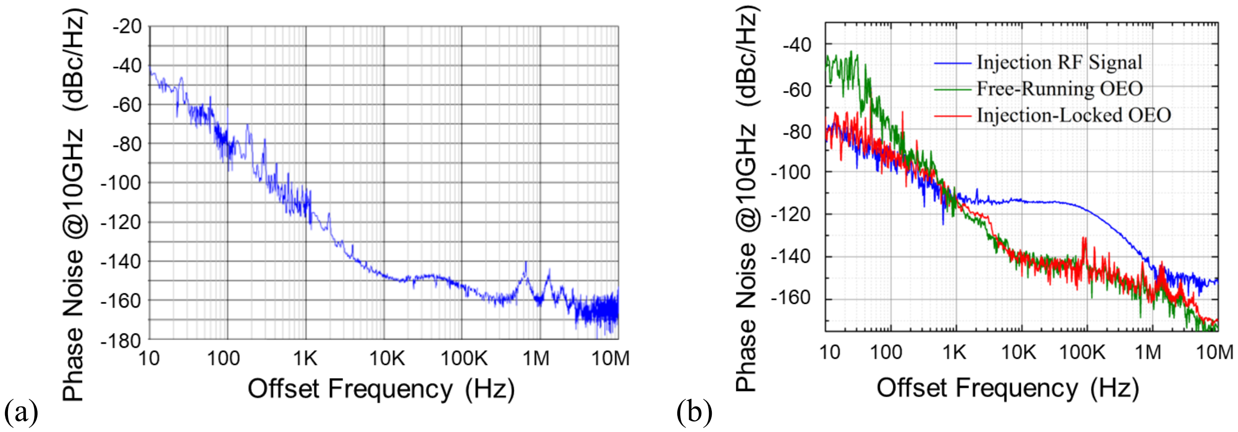

Figure 1-6. Single side band Phase Noise from COEO and Dual-Delay OEO.

(a) Coupled OEO, using an optical loop plus an optoelectronic loop, (b) OEO using double fiber delay line references and an RF injection mechanism. Adapted from [22], [24].

These two approaches reach about -148 and -140 dBc/Hz phase noise at 10 kHz for a 10 GHz carrier, which is remarkable in these types of applications.

1.2.2. Microcombs

Microcombs and electro-optical combs (EO combs) are technologies that enable the generation of highly stable, spectrally pure microwave signals but are not PMOs per se. Instead, they serve as essential tools for optical frequency division and photonic microwave synthesis [25].

Microcombs are generated when a CW laser interacts with a high-Q microresonator, leading to the formation of an optical frequency comb via nonlinear Kerr effects [26]. These microresonators are compact optical cavities that efficiently confine light, enabling significant nonlinear interactions. The resulting microcomb consists of a set of evenly spaced optical frequencies, which can be used for frequency synthesis and metrology applications. Figure 1-7 illustrates the spectral and temporal characteristics of microcomb generation. The cavity resonances correspond to microwave frequencies, making microcombs highly attractive for generating signals in the GHz to THz range [27].

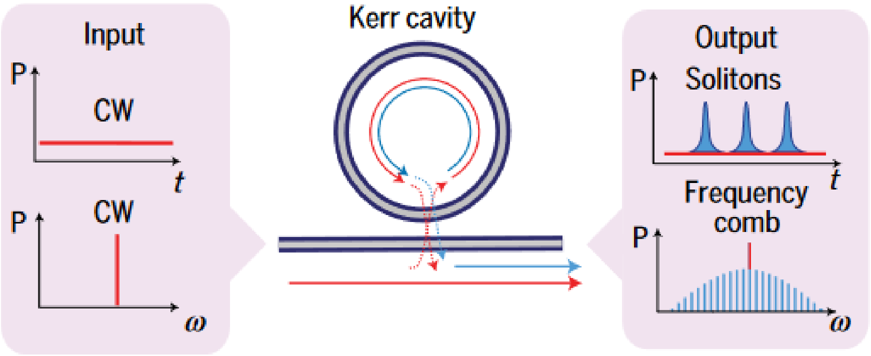

Figure 1-7. General representation of microcomb generation from a CW laser-driven microresonator. Taken from [27]

Recent advancements in photonic microwave oscillators utilizing microresonators, such as the work reported in [28], have demonstrated phase noise levels of approximately -138 dBc/Hz at a 10 kHz offset for a 10 GHz-equivalent microwave signal. Figure 1-8 illustrates the phase noise performance achieved in this study.

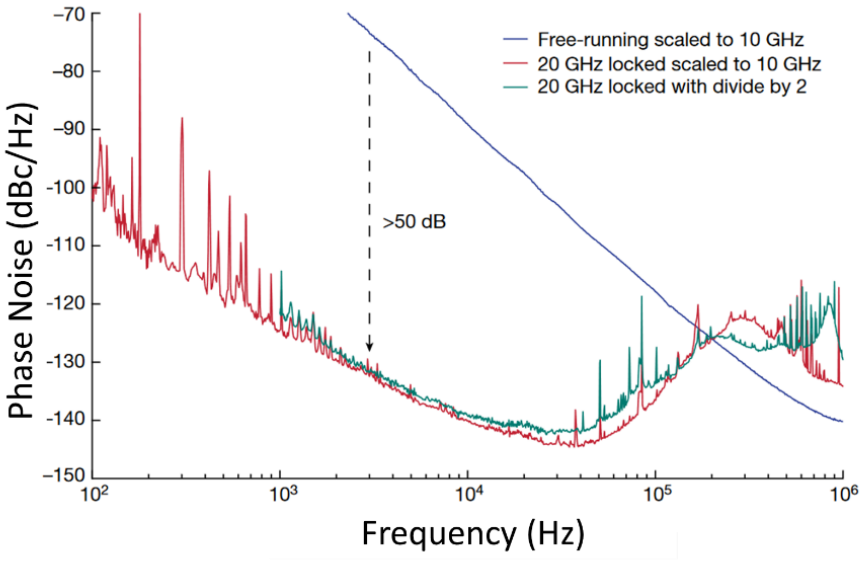

Figure 1-8. Single side-band phase noise scaled to 10 GHz of a free-running 20 GHz microcomb.

Free-running noise (blue) locked 20 GHz microwave (red) and locked 20 GHz microwave after regenerative frequency division by two (green). Adapted from [28].

Microcombs offer a compact, chip-scale solution for generating ultra-stable microwave signals, enabling wide frequency tunability, low phase noise, and integration into photonic circuits for high-precision applications. Despite this promise, microcombs face challenges such as fabrication complexity, temperature sensitivity, and high-power requirements.

1.2.3. Electro-Optical Combs

EO combs, in contrast, are generated using an electro-optical modulator driven by a microwave signal, producing a frequency comb whose characteristics depend on the modulation parameters [29]. Unlike coupled optoelectronic oscillators (COEOs), EO combs do not have an internal feedback loop, making them more susceptible to microwave noise that can degrade phase stability. To address this limitation, advanced stabilization techniques, such as the dual-laser reference approach, have been proposed [30]. Figure 1-9.a illustrates the architecture of electro-optical frequency comb generation for microwave synthesis, while Figure 1-9.b presents the achieved phase noise levels for a 10 GHz carrier.

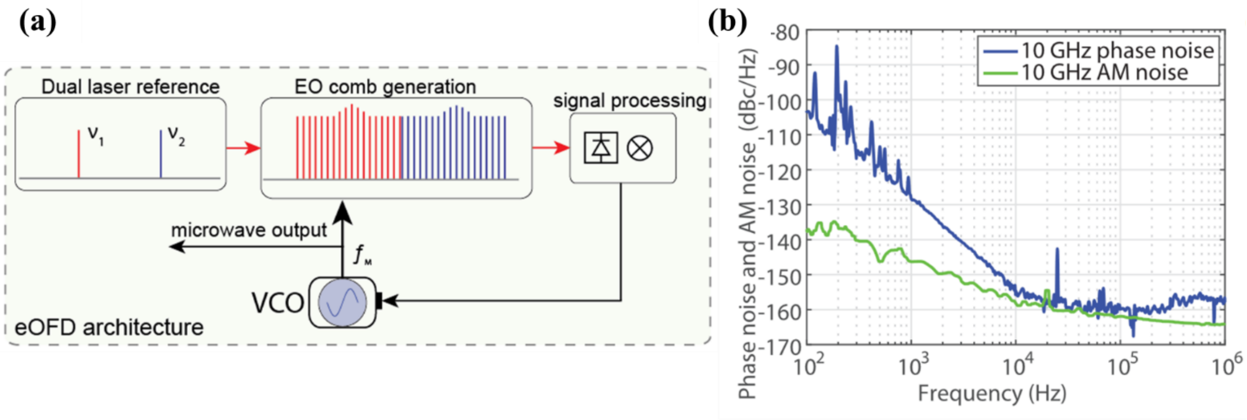

Figure 1-9. (a) Architecture of electro-optical frequency division (eOFD) based on dual laser reference electro-optical frequency comb, (b) single side band phase noise achieved by this technique.

Adapted from [30].

These developments illustrate the expanding role of frequency comb technology in photonic microwave synthesis, bridging the gap between optical and microwave domains and enabling new high-performance frequency sources.

1.3. PHOTONIC MICROWAVE OSCILLATORS BASED ON MLLS

Having reviewed PMOs that utilize CW lasers as their optical source, this section shifts focus to mode-locked lasers (MLLs) as a key enabling technology for PMOs.

Mode-locked lasers are a specialized type of laser designed to generate ultra-short optical pulses, typically in the picosecond to femtosecond range, with exceptionally high peak power. This performance is achieved through a process known as mode-locking, which synchronizes the phases of all longitudinal modes oscillating within the laser's resonant cavity. As a result, these synchronized modes interfere constructively at regular intervals, producing a stable train of pulses with a repetition rate defined by the cavity length. Figure 1-10 illustrates the process of ultra-short pulse generation inside a mode-locked laser cavity [31].

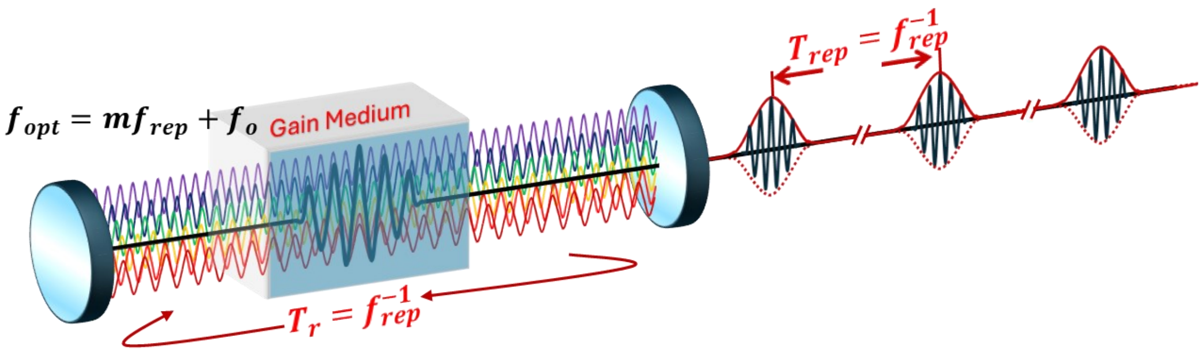

Figure 1-10. Ultra-short pulses generation inside a mode-locked laser cavity.

Mode-locking can be achieved using either active or passive techniques:

- Active mode-locking employs an external optical modulator, such as an acousto-optic or electro-optic modulator, to impose periodic modulation on the intracavity light, aligning the phases of the modes.
- Passive mode-locking uses a saturable absorber, a material whose absorption decreases with increasing light intensity, favoring the formation of high-intensity pulses spontaneously.

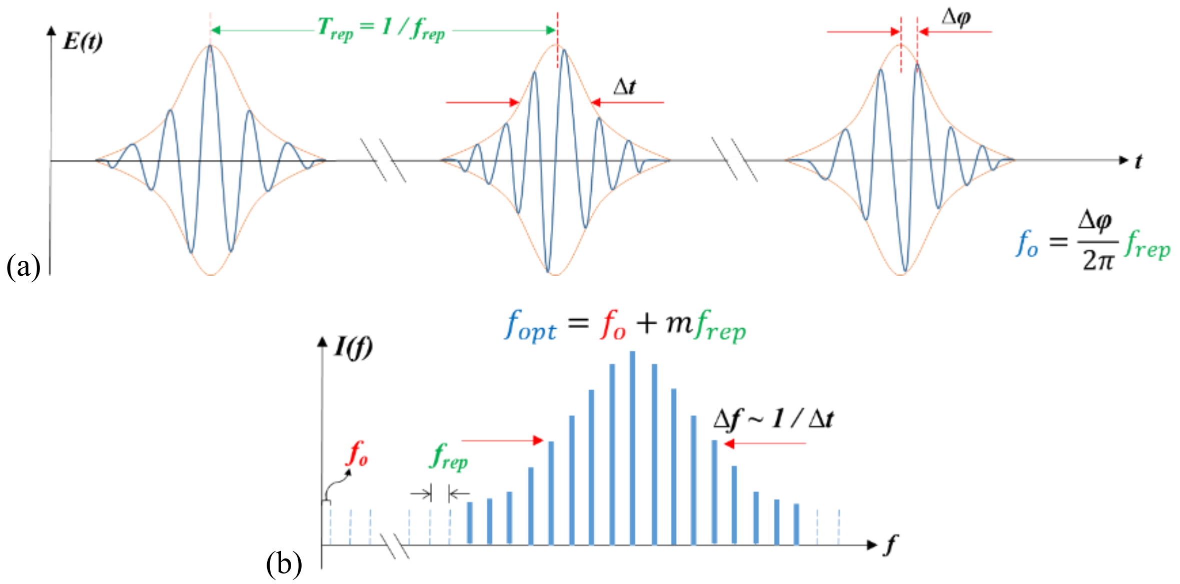

Figure 1-11. Time and frequency domain representation of the pulse train generated by a mode-locked laser.

(a) Time representation of the train pulse created by a few in-phase modes transmitted in a mode-locked laser at a repetition rate f_{rep}. The phase difference between the carrier and the envelope represents the offset frequency (f_o) (b). Optical spectrum of a mode-locked laser, also known as frequency comb.

These mode-locking techniques allow for precise control over the pulse generation process, enabling the production of pulses with exceptional temporal precision and peak power. Figure 1-11.a illustrates the pulse train output of a mode-locked laser in the time domain, showing both the carrier wave and the pulse envelope. Each pulse is separated by the repetition period determined by the repetition frequency (f_{rep}). Figure 1-11.b illustrates the frequency domain representation of the pulse train, commonly referred to as a frequency comb. This term arises because the optical frequencies are separated by multiples of the laser's repetition rate, corresponding to the harmonics of the resonator cavity's longitudinal modes. Each optical frequency component f_{opt} is then composed of the m^{th} harmonic of the pulse repetition rate (f_{rep}) and the carrier envelope offset frequency (f_o).

The characteristic spectrum of a mode-locked laser establishes a crucial link between optical frequencies and radio frequencies (RF), serving as a bidirectional frequency measurement tool [32]. Figure 1-12 illustrates how an optical frequency comb functions as a "clockwork" mechanism, enabling precise and direct access to optical frequencies from the microwave domain or synthesizing microwave signals using optical references.

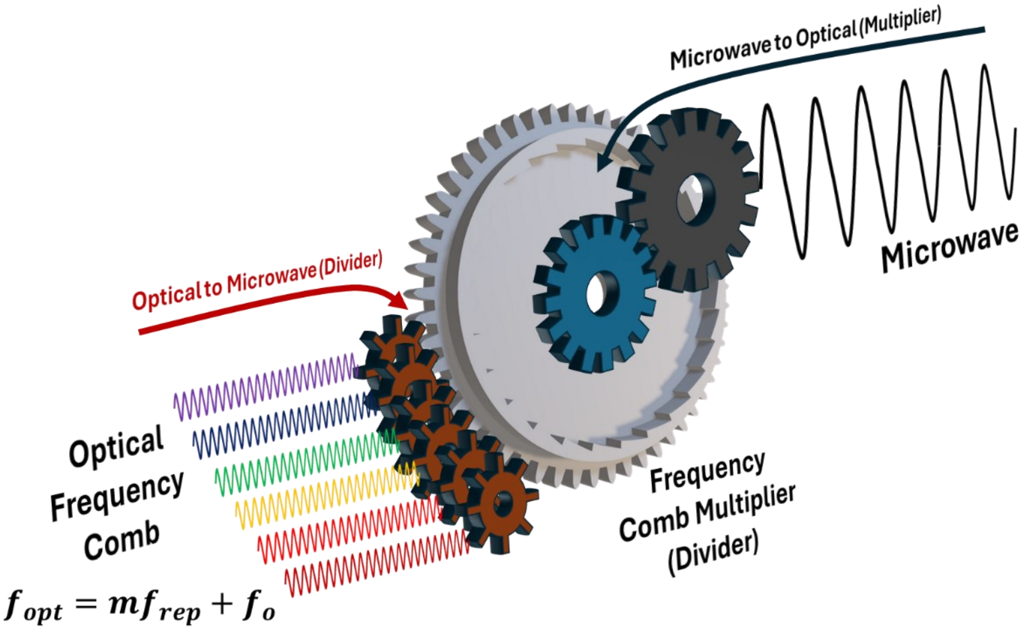

Figure 1-12. Optical frequency comb as a clockwork bridge between optical and microwave domains.

.

By tracking and stabilizing both the pulse repetition rate (f_{rep}) and the carrier-envelope offset frequency (f_o) to a microwave standard, such as an atomic clock, arbitrary optical frequencies can be precisely measured [33]. Additionally, the stability of optical frequencies can be translated into the synthesis of RF signals through direct photodetection of the optical pulse train [34].

State-of-the-art ultrashort pulsed mode-locked lasers continue to push performance boundaries in pulse duration, repetition rate, spectral bandwidth, energy, and timing stability. Recent advancements have demonstrated pulse durations below 5 femtoseconds [35], optical spectra spanning over an octave (600 nm to 1200 nm), repetition rates exceeding 100 GHz [36], sub-femtosecond timing jitter in free-running operation [37], and residual carrier-envelope offset phase jitter below 20 attoseconds (10^{-18} s) [38].

Mode-locked lasers stabilized by ultra-stable optical cavities have demonstrated unprecedented phase stability and spectral purity, leveraging optical frequency division (OFD) techniques. This method, described in [39] and illustrated in Figure 1-13, enables the generation of an ultra-stable 10 GHz microwave signal directly derived from an optical reference. This approach has achieved phase noise levels as low as -104 dBc/Hz at 1 Hz offset and -153 dBc/Hz at 10 kHz offset, significantly outperforming conventional microwave oscillators.

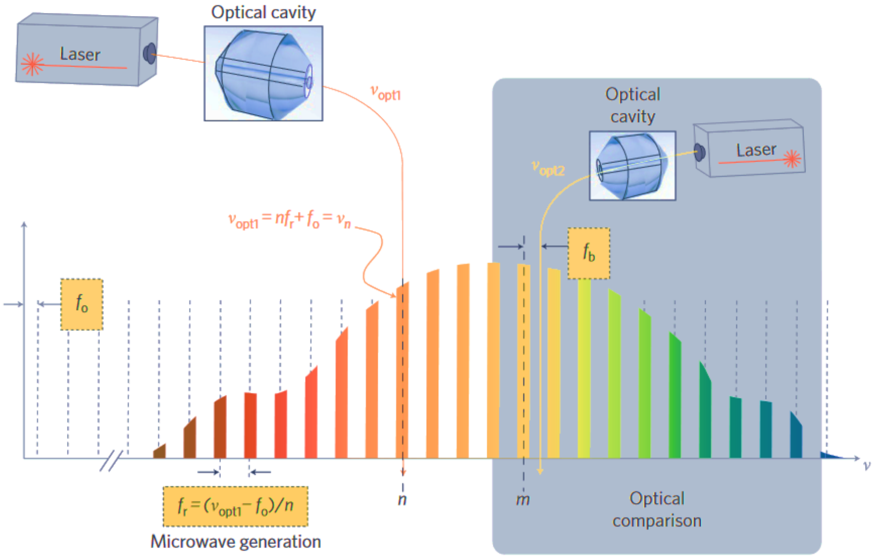

Figure 1-13. Optical frequency division from optical cavities using an optical frequency comb from a MLL.

The OFC spectrum is stabilized by phase-locking the n^{th} comb element to an optical reference n_{opt1} while simultaneously stabilizing the laser offset frequency f_o. Taken from [39]

Further advancements, such as the transfer oscillator technique introduced in [40], have successfully suppressed additive noise in optical frequency combs, resulting in absolute phase noise levels below -106 dBc/Hz at 1 Hz offset. This improvement enhances long-term frequency stability but comes with a trade-off, with phase noise reaching -145 dBc/Hz at 10 kHz offset.

Recent work in this area, as reported in [41], presents a relatively compact approach to OFD, achieving a remarkable absolute phase noise of -164 dBc/Hz at 10 kHz offset, albeit with an increased phase noise of -80 dBc/Hz at 1 Hz offset.

These findings reinforce that OFD-based PMOs surpass conventional microwave oscillators and optoelectronic oscillators (OEOs) based on CW lasers in multiple aspects, offering an unparalleled level of phase stability. Mode-locked lasers play a crucial role in this development, serving as the primary optical source. The PMO developed in this thesis follows a similar conceptual framework, although employing a different stabilization method, while leveraging the inherent advantages of mode-locked laser architectures for ultra-stable microwave generation.

1.4. MOTIVATION FOR PHOTONIC MICROWAVE OSCILLATORS

As previously discussed, photonic microwave oscillators have emerged as essential components in high-precision applications due to their superior phase noise performance, frequency stability, and tunability. This section highlights key applications where PMOs provide significant advantages, emphasizing their specific timing requirements.

1.4.1. Time and Frequency Metrology

PMOs play a crucial role in precision time and frequency metrology. Their ability to operate in both the optical and microwave domains facilitates the long-distance transmission of photonic microwave signals, essential for optical clock synchronization. This capability supports applications such as high-fidelity calibration of microwave clocks and the advancement of next-generation optical atomic clocks. These developments are particularly relevant for the ongoing efforts to redefine the SI second [7], [42].

For such applications, stringent timing precision and stability are required, often necessitating frequency measurements with uncertainties below 10^{-12}.

1.4.2. Large Photon Science Facilities

In large-scale photon science facilities, such as particle accelerators and Free-Electron Lasers (FELs), precise RF synchronization is critical for accurate control of particle beams and laser pulses. PMOs provide the high stability and low phase noise needed to enhance beam quality and overall system performance [43].

- Particle Accelerators: The synchronization of RF cavities requires femtosecond to picosecond-level timing precision to ensure consistent particle acceleration, beam coherence, and minimal emittance growth [44], [45].
- Free-Electron Lasers (FELs): These systems rely on precise synchronization between electron bunches and electromagnetic fields. PMOs ensure femtosecond to attosecond-level timing stability, crucial for generating coherent radiation pulses [46], [47]. This enables high-resolution imaging techniques such as ultrafast spectroscopy, which captures chemical and physical processes at subatomic scales [48], [49].

In both cases, PMOs provide a critical backbone for laser-microwave timing synchronization, pushing the boundaries of precision and reliability in scientific research and industrial applications [50].

1.4.3. Space Applications

PMOs are fundamental to space-based applications, particularly in radio astronomy and interferometry. Their superior phase noise and frequency stability are crucial for detecting faint astronomical signals and ensuring precise data correlation across vast distances.

- Radio Telescopes: Facilities like ALMA (Atacama Large Millimeter/submillimeter Array) require timing precision at the 40-femtosecond level to ensure coherent operation of multiple antennas as a single telescope [51].
- Very Long Baseline Interferometry (VLBI): This technique, which involves multiple telescopes spanning thousands of kilometers, depends on ultra-stable photonic microwave signals for high-resolution imaging of cosmic sources [52].

- Space VLBI: Future missions incorporating space-based radio telescopes require sub-picosecond timing accuracy, which PMOs provide, enhancing baseline precision and coherence for deep-space observations [53], [54].

1.4.4. Radar Systems

Radar systems, particularly coherent radars used in synthetic aperture radar (SAR) and Doppler radar, demand precise and stable microwave signals. PMOs contribute by significantly reducing phase noise, improving the accuracy and resolution of radar imaging and velocity measurements [55], [56], [57].

- High-Resolution Imaging: Low phase noise improves range resolution and Doppler sensitivity, crucial for applications such as earth observation, military surveillance, and autonomous navigation.
- Precision Timing: Advanced radar systems require timing stability at the picosecond to sub-picosecond level to ensure accurate distance and velocity measurements [58].

1.4.5. Quantum Computing

Quantum computing relies on precise control and synchronization of operations to maintain qubit coherence and minimize errors. PMOs support high-fidelity qubit manipulation by providing ultra-stable clock signals [59].

- Qubit Operations: Quantum gate operations demand timing precision at the sub-nanosecond level to reduce phase decoherence and enhance computational accuracy.
- Quantum Networks: PMOs facilitate synchronization in distributed quantum computing and quantum communication networks, improving the stability of entangled qubit operations [60].

1.5. SCOPE OF THE DISSERTATION

This dissertation provides a comprehensive study of photonic timing instrumentation and microwave synthesis, detailing key components, measurement techniques, and system-level innovations. The research is structured as follows:

- Chapter 2 presents the core timing instrumentation tools developed within the research group. It introduces balanced optical cross-correlators (BOCs), describing their design, various implementations—including a novel integrated version—and their role in high-precision timing systems. A detailed characterization of their timing sensitivity and noise floor is provided. The chapter then discusses the balanced-optical microwave phase detector (BOMPD), which enables precise characterization of timing jitter between optical and microwave signals, along with an evaluation of its performance in terms of timing sensitivity and noise characteristics.

- Chapter 3 shifts the focus to mode-locked lasers (MLLs), the core optical source of the system. This chapter reviews different methods for phase noise and timing jitter characterization of MLLs, leveraging the tools from Chapter 2. It also explores the photodetection of ultrashort pulses for microwave synthesis, discussing the underlying physical processes, the role of photodiodes, and the challenges and advantages associated with converting optical pulse trains into stable microwave signals. Various photodiode types, their inherent limitations, and their impact on phase noise and timing stability are analyzed.

- Chapter 4 integrates concepts from the previous sections into the design and realization of the Photonically Referenced Extremely Stable Oscillator (PRESTO). It provides a detailed explanation of the feedback loop model, including its constraints and operational principles. The system's experimental implementation and performance evaluation are thoroughly examined, with an emphasis on stability optimization and noise reduction. The chapter also highlights key challenges and potential improvements to enhance system performance.

- Chapter 5 concludes with a summary of key findings, contextualizing the contributions of this research within the broader state of the art. It also outlines future research directions, addressing open challenges and possible advancements for further refinement of PRESTO and photonic microwave oscillator technologies.

2. TIMING CHARACTERIZATION TOOLBOX

This chapter introduces the specialized instrumentation used for time and frequency metrology, essential for the characterization of ultra-low-noise optical and microwave sources. The ability to measure and analyze signals on femtosecond or sub-femtosecond time scales requires highly sensitive and precise detectors.

The research presented here highlights the expertise developed by the research group over the past decades. Two key types of timing detectors are explored: one for optical signal characterization and another for the characterization of signals combining optical and microwave components. Each detector is described in detail, covering its operating principles, implementation, and performance characterization.

These detectors serve as the foundation for subsequent chapters, as they are extensively used throughout the development of this thesis to enable high-precision timing analysis and noise characterization.

2.1. BALANCED OPTICAL CROSS-CORRELATOR

The Balanced Optical Cross-Correlator (BOC) is a highly sensitive timing detector widely used for characterizing, measuring, and synchronizing optical pulsed signals [61]. Operating on a nonlinear optical principle, the BOC offers attosecond timing sensitivity, long-term stability, and robustness against amplitude fluctuations in optical signals [62], [63].

Figure 2-1 illustrates the fundamental working principle of the BOC. To measure the relative timing Δt of two optical pulses (depicted as red solid lines), the pulses are orthogonally polarized and directed into a nonlinear crystal arranged in a double-pass configuration. Due to the birefringence in the crystal, the orthogonal pulses traveling at each axes experience differences in their group velocities. These pulses interact inside the crystal, generating sum-frequency light (shown as blue pulses). The intensity of this generated sum-frequency light depends on the temporal overlap of the pulses during both forward and reverse passes.

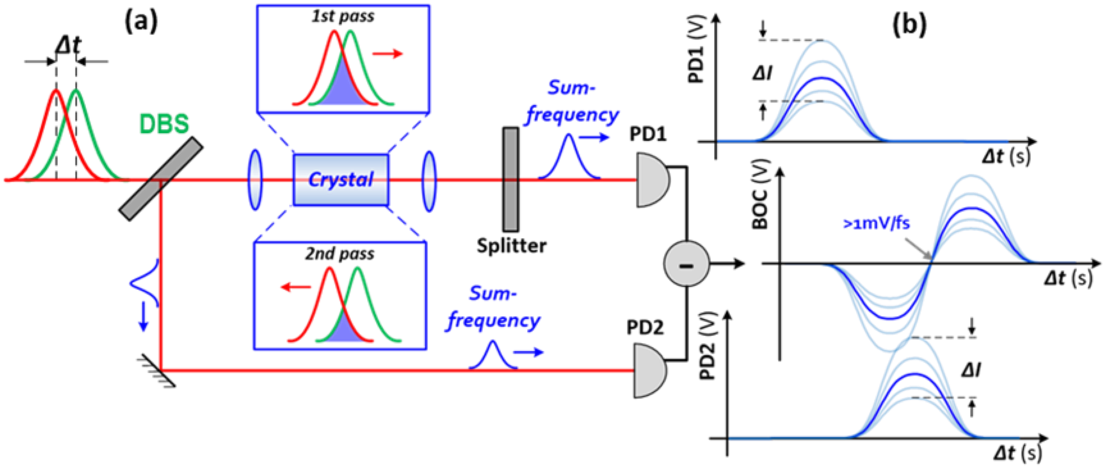

Figure 2-1. Principle of timing detection using a Balanced Optical Cross-Correlator (BOC).
DBS: Dichroic Beam Splitter, PD1 and PD2: Photodetectors in a balanced configuration. Adapted from [64]

After each pass through the nonlinear crystal, dichroic beam splitters (DBS) separate the original pulses from the generated sum-frequency light. This sum-frequency light is then measured by a balanced photodetector (BPD), enhancing the system’s robustness against intensity fluctuations in the input pulses. Each photodetector produces a voltage signal proportional to the relative time delay between the pulses. The detector output exhibits a “zero error” signal for a certain time delay between the two pulses (i.e. before entering the nonlinear) where they generate the same amount of sum frequency light for each pass and a nonzero signal when there is an offset in time.

The right panel of Figure 2-1 illustrates the effect of modulating the energy of one pulse by ΔI while varying the time delay between pulses (Δt). This highlights how sum-frequency generation is influenced by pulse energy variations in the double-pass configuration. Despite these fluctuations, the zero-crossing position ($\Delta t = 0$) remains stable, showcasing the BOC’s inherent robustness against amplitude noise near the zero-crossing boundary of the characteristic S-curve.

To determine the detector’s timing sensitivity, one of the input pulses is delayed with respect to the other, scanning across the full pulse duration. This procedure generates the BOC’s S-curve, where the zero-crossing slope is interpolated to a linear slope, providing a quantitative measure of the detector’s sensitivity.

Due to its attosecond resolution, the BOC has become indispensable in highly demanding applications. It has enabled femtosecond and sub-femtosecond synchronization in large-scale photon science facilities, such as free-electron lasers (FELs) and particle accelerators, where precise optical-to-microwave synchronization is critical [65], [66], [67].

2.1.1. *Free-Space Bulk Optics BOC*

The most common implementation of the BOC relies on type-II second harmonic generation (SHG) in a bulk periodically poled potassium titanyl phosphate (PPKTP) crystal. Various iterations of this technique have been demonstrated in previous studies [68], [69]. Figure 2-2 presents the schematic of this setup.

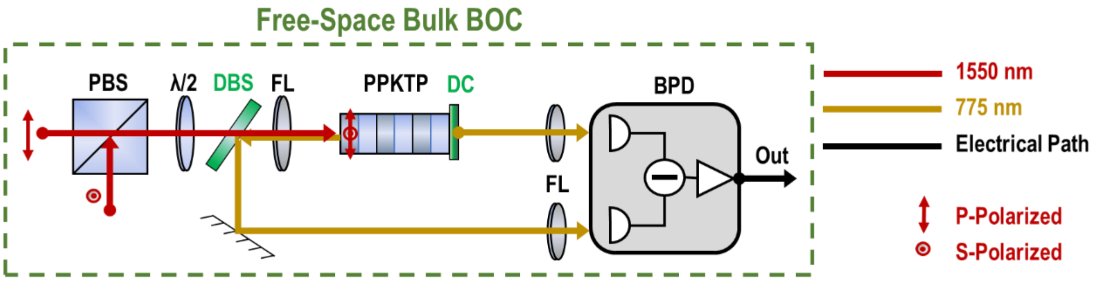

Figure 2-2. Free-space type-II second harmonic generation BOC for 1550nm optical pulses.

PBS: Polarization Beam Splitter; λ/2: Half-wave Plate; DBS: Dichroic Beam-splitter; FL: Focus Lens; DC: Dichroic Coating; PPKTP: Periodically Poled Potassium Titanyl Phosphate Crystal; BPD: Balanced Photodetector.

In this setup, two orthogonally polarized optical pulses are first combined using a polarization beam splitter (PBS). A half-wave plate (λ/2) aligns the ordinary and extraordinary axes of the PPKTP crystal with the incoming pulses to maximize second harmonic generation (SHG) efficiency. Due to the birefringence of the crystal, one pulse propagates faster than the other, leading to a temporal separation. The time difference in their propagation is given by:

$$\Delta T_0 = T_p - T_s = L/v_{g,p} - L/v_{g,s}$$

Equation 2-1

where L is the effective length of the crystal, and $v_{g,p}$and $v_{g,s}$ are the group velocities of the two principal axes. The crystal length of a few millimeters is sufficient to induce a significant pulse walk-off, comparable to the pulse duration. During this temporal walk-off, the PPKTP crystal generates a second harmonic (SH) signal whose intensity correlates with the degree of pulse overlap.

The incoming fundamental pulses are focused into the crystal, where they travel in a 2-pass configuration. This is accomplished using a dichroic coating (DC) at the end of the crystal that is highly reflective for 1550 nm pulses and anti-reflective for the 775 nm SH pulses.

This first SH pulse is separated, and the fundamental pulses are reflected for a second pass through the crystal in the opposite direction. This second pass produces an additional SH pulse that is further separated from the fundamental pulses by a dichroic beam splitter (DBS) highly reflective for incoming 775 nm pulses at 45° angles of incidence.

Both SH pulses are then detected using a balanced photodetector (BPD), which outputs a voltage proportional to the difference in SH power between the two passes. This differential detection enhances common-mode noise rejection, significantly improving timing jitter sensitivity and robustness against intensity fluctuations.

2.1.2. Integrated Waveguide-based BOC

With the increasing demand for advanced timing detectors, particularly in applications requiring synchronization across multiple fiber links, the alignment process from the bulk BOC can become increasingly challenging when managing numerous devices. Additionally, certain applications impose size constraints and pulse energy limitations, necessitating the development of compact and practical solutions.

Over the past decade, significant efforts have been made to develop an integrated version of the BOC based on segmented PPKTP waveguide technology, pioneered by former group collaborators at the MIT and AdvR in Montana, USA [70], [71]. Fiber-coupled waveguides offer the advantage of significantly enhanced second-harmonic conversion efficiency, leading to improved timing sensitivity while reducing the size and power requirements of timing detectors. However, early implementations faced challenges such as excessive signal coupling losses, which stemmed from the absence of a dichroic waveguide splitter, inadequate dielectric coatings, and difficulties in fiber coupling to Type-II second harmonic generation (SHG) waveguides. Addressing these technical limitations was essential to unlocking the full potential of integrated waveguide-based timing detectors.

Recent advancements have mitigated these issues, primarily through the integration of a wavelength division multiplexer (WDM), which enhances coupling efficiency for both fundamental and second-harmonic pulses within the waveguide.

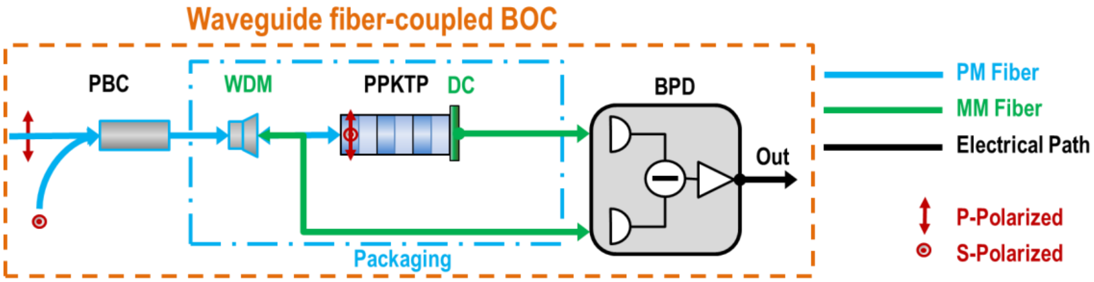

Figure 2-3. Fiber-coupled waveguide-based BOC for 1550nm optical pulses.

BOC; PBC: Polarization Beam Combiner; WDM: Wavelength Division Multiplexer; DC: Dichroic Coating; PPKTP: Periodically Poled Potassium Titanyl Phosphate Crystal; BPD: Balanced Photodetector; PM: Polarization Maintaining Fiber; MM: Multimode

The fiber-coupled integrated waveguide BOC (WBOC) is schematically depicted in Figure 2-3. The back facet of the PPKTP chip is coated with a dichroic material that is anti-reflective at 775 ± 25 nm and highly reflective at 1550 ± 50 nm. The device's input consists of a standard polarization-maintaining (PM) fiber, with its fast and slow axes aligned to the main axes of the crystal.

The input optical pulses are directed into the PPKTP waveguide using a WDM, which functions as a fiber-coupled dichroic beam splitter. The WDM separates the input pulses and directs them into the PPKTP waveguide for cross-correlation. The SH signals generated in both forward and backward directions are then separated from the fundamental optical pulses using the dichroic coating and WDM, respectively. Finally, these separate signals are detected by the BPD to extract the relative time delay information.

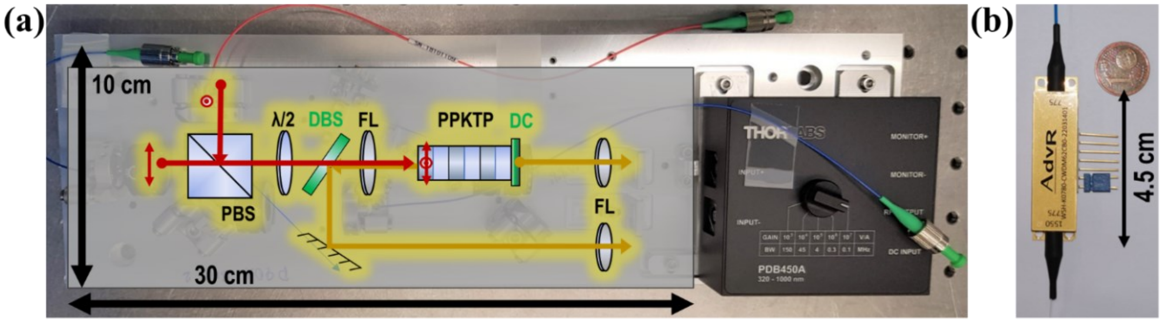

Figure 2-4. Physical implementations of the BOC with size comparisons.

(a) Free-space bulk optics BOC setup, (b) Fiber-coupled integrated waveguide BOC

The WBOC offers significant advantages over its bulk optics counterpart. Firstly, the waveguide cross-sectional area is approximately 100 times smaller than the beam spot size in bulk BOC crystals, leading to 100× higher SHG efficiency and an expanded dynamic range.

Additionally, Figure 2-4 illustrates the contrast in size between the bulk BOC and the fiber-coupled WBOC, highlighting the latter's significant size reduction. This makes the WBOC ideal for compact and integrated applications, where free-space optical setups would be impractical. Moreover, the WBOC is inherently more resistant to mechanical vibrations and misalignment, as it eliminates the need for free-space optical components.

Despite these advantages, the bulk BOC can be still preferable in specific applications, particularly when high pulse energy is involved. In such cases, high-intensity pulses can induce nonlinearities in the fiber or even exceed the damage threshold of integrated waveguides, making free-space optics a more suitable choice for handling high-power optical pulses.

2.1.3. Timing Sensitivity Characterization

Figure 2-5 illustrates the experimental setup designed to characterize the timing sensitivity of the two BOCs. In this setup, the output pulses from a mode-locked laser are split into two paths using a PBS. One path includes a motorized delay line stage (MDL) to introduce a controlled relative delay between the two pulse trains. The pulses are then recombined with orthogonal polarizations inside the BOC using the integrated PBC.

The motorized delay line systematically scans over the full pulse duration to determine the timing sensitivity of each BOC. The characteristic S-curve is acquired by monitoring the voltage output of the BOC on an oscilloscope. To ensure a fair performance comparison, all experimental parameters, including optical power levels and detection conditions, remain consistent between both implementations. This approach enables an accurate evaluation of the sensitivity and robustness of each BOC under identical operating conditions.

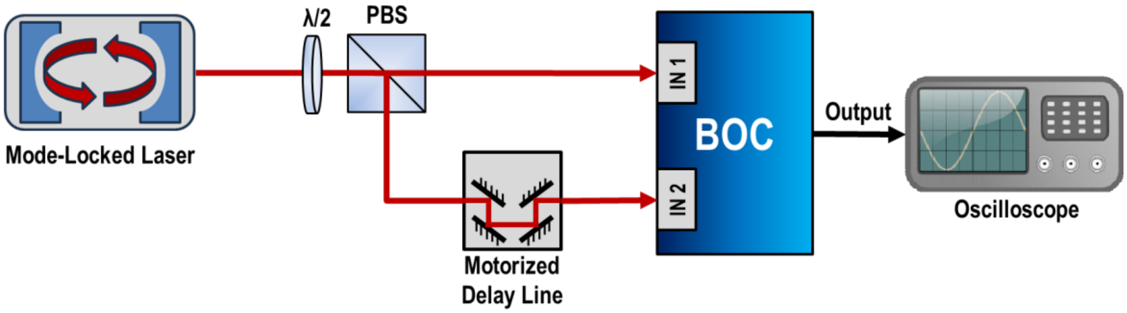

Figure 2-5. BOC sensitivity characterization experimental setup.

Figure 2-6 presents the results of the timing sensitivity measurements performed using a OneFive 1550 nm mode-locked laser operating at 216.66 MHz with a pulse duration of approximately 200 fs. The total average optical power at the input of both BOCs is maintained at 10 mW (distributed as 5 mW per orthogonal beam). The balanced photodetector is set to a 4 MHz bandwidth, corresponding to a trans-impedance gain of 10^5 V/A.

The zero-crossing slope of the S-curve represents the timing sensitivity of each BOC. By interpolating multiple measurements, the WBOC exhibits an average timing sensitivity of approximately 15 mV/fs (±0.1 mV/fs), as shown in Figure 2-6.a. In contrast, the bulk BOC demonstrates a sensitivity of only 0.14 mV/fs (±0.1 mV/fs). This confirms that the WBOC achieves two orders of magnitude higher timing sensitivity, demonstrating its superior resolution and precision.

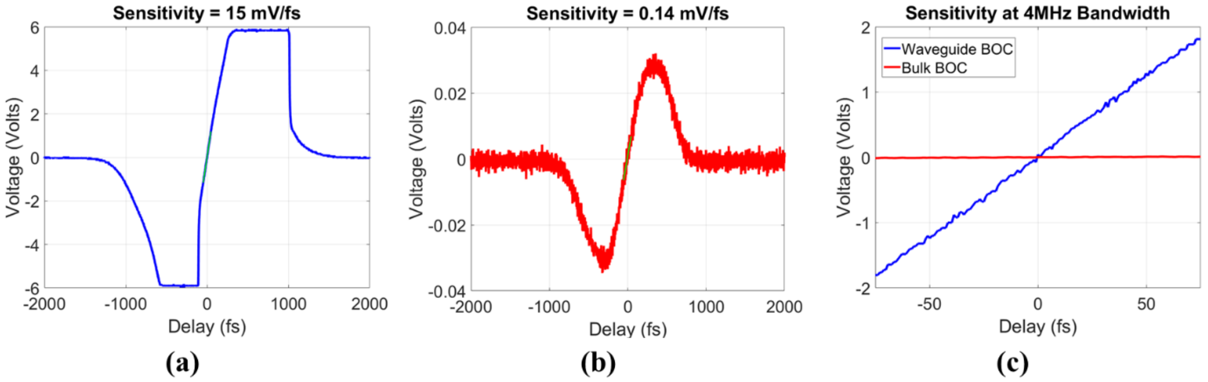

Figure 2-6. Timing sensitivity comparison between bulk BOC and waveguide BOC using a OneFive 216.66 MHz mode-locked laser.

S-curve traces at the output of (a) the waveguide BOC and (b) the bulk BOC. (c) Responses when scaled together.

2.1.4. *Noise Floor Characterization*

To evaluate the intrinsic noise limitations of the WBOC, its high timing sensitivity can be leveraged to measure noise characteristics at the balanced photodetector output. This is achieved by delaying the optical pulses such that they do not temporally overlap, ensuring that the dominant noise contributions arise primarily from electronic noise sources rather than timing fluctuations.

The electronic noise floor is characterized by measuring the baseband noise at the detector output using a signal source analyzer. This baseband noise spectrum is then converted into jitter spectral density using the previously determined timing sensitivity calibration. To determine the minimum attainable timing jitter, the jitter spectral density is integrated over a range of frequency offsets.

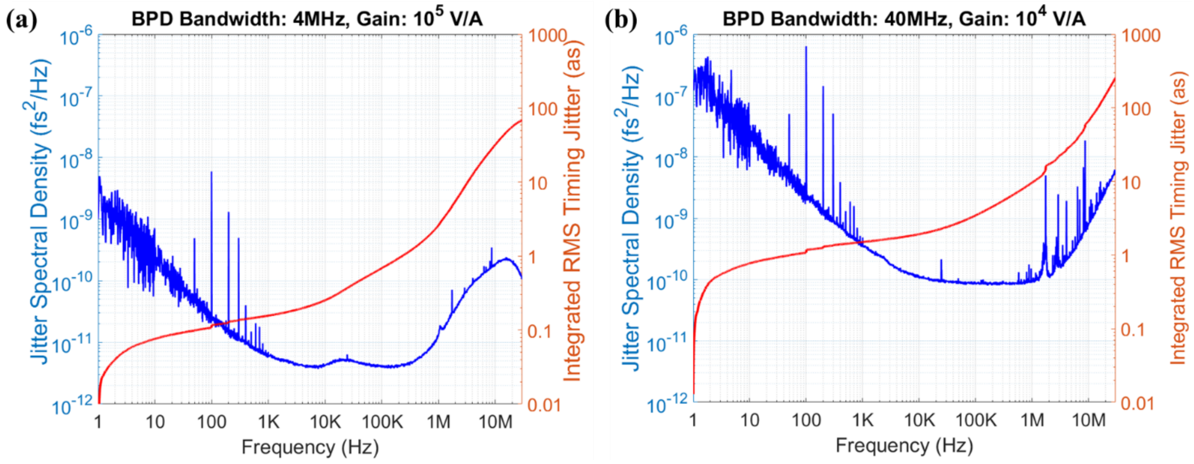

Figure 2-7. Jitter Spectral Density corresponding to the electronic noise floor of the Waveguide BOC.

(a) at a 4 MHz bandwidth and 10^5 V/A transimpedance gain, (b) at a 40MHz bandwidth and 10^4 V/A gain

Figure 2-7 shows the jitter spectral density due to the electronic noise floor, measured at two different bandwidth settings: 4 MHz and 40 MHz. These correspond to timing sensitivities of 25 mV/fs and 2.5 mV/fs, respectively. Table 2-1 summarizes the integrated RMS timing jitter over a range of frequency offsets, starting from 1 Hz.

The results indicate that the total integrated RMS timing jitter from 1 Hz to 4 MHz is approximately 12.68 attoseconds. At a higher bandwidth of 40 MHz, while the system enables measurements in a broader frequency range, it exhibits higher noise levels, resulting in an integrated jitter of 255 attoseconds up to 30 MHz offset.

Table 2-1. Integrated RMS Timing Jitter at the balanced photodetector for different offset frequencies and at different bandwidths.

Offset Frequency (Hz)	**Integrated jitter from 1 Hz (as)**	
	BW: 4 MHz Gain: 10^5 V/A	**BW: 40 MHz Gain: 10^4 V/A**
10	0.07	0.77
100	0.11	1.14
1×10^3	0.15	1.51
1×10^4	0.26	1.92
1×10^5	0.68	3.52
1×10^6	2.62	9.47
4×10^6	12.68	26.3
3×10^7	68.85	255.5

As a key point, the higher timing sensitivity leads to improved measurement resolution. Also, the internal bandwidth of the balanced photodetector plays a critical role in determining the noise floor. Increasing the bandwidth results in reduced gain, affecting timing precision and leading to a tradeoff between bandwidth and noise performance.

2.2. BALANCED OPTICAL MICROWAVE PHASE DETECTOR

Having outlined the characteristics of a timing detector for optical sources, let’s now proceed with a timing detector that is capable of operating with both optical pulsed sources and microwave signals. A widely implemented solution to this problem is the “Balanced Optical-Microwave Phase Detector” (BOMPD) utilizing electro-optic sampling to scan between optical pulse trains and a microwave signal. This is accomplished by employing an integrated, fiber-based interferometer that is equipped with a precisely biased electro-optical phase modulator [72], [73].

Conventional laser-to-microwave characterization systems generally employ photodetection to convert optical signals into electronic signals. However, these systems encounter significant nonlinearities when exposed to the intense, ultra-short optical pulses generated by femtosecond pulsed sources [74], [75]. The phase of the translated optical signal is then compared to the phase of the microwave signal using an electronic mixer [76]. However, the electronic mixer typically produces only a few microvolts of response for a femtosecond-level phase or delay change. As a result, these systems struggle to achieve precise synchronization within a few femtoseconds between optical and microwave sources.

The BOMPD plays a crucial role in this context by utilizing a balanced optical detection scheme to measure the phase difference between a microwave signal and the temporal center of gravity of an optical pulse train [77]. This approach offers significant advantages in two key applications. First, the ability to determine the phase relationship between an optical pulse train and an RF source enables the BOMPD to serve as a characterization tool for assessing the relative timing jitter between these hybrid sources. Second, access to phase and timing difference information allows the BOMPD to facilitate synchronization between RF sources and femtosecond lasers. This is achieved through the implementation of a Phase-Locked Loop (PLL), enabling the transfer of frequency stability from ultra-stable RF sources to the laser, or vice versa.

The main advantage using a BOMPD as phase detector in the optical domain over electronic phase detectors is the avoidance of AM-PM conversion noise [78]. This results in a lower noise floor and increased timing sensitivity compared to electronic techniques. Furthermore, the balanced detection scheme efficiently cancels the contribution of relative intensity noise generated by the laser source to the timing measurement (AM Noise).

This section will outline the basic operation principles of the BOMPD, its use as a phase detector for timing measurements, and the performance achieved when employed in a synchronization system.

2.2.1. Operation Principle

Figure 2-8 illustrates the general operation of a BOMPD as a phase detector, between its two inputs: one from a pulsed laser and the other from an RF signal. The optical pulse train from the laser is divided equally by using a polarization beam splitter and fed into two electro-optical amplitude modulators. These modulators are both driven by the same RF source but having 180º phase difference from one another. The frequency of RF source should be equivalent to the laser's repetition rate or one of its harmonics, for a proper phase relationship and detection. This whole framework leads to a counter-balanced modulation scenario.

The two amplitude-modulated optical pulses are directed into a balanced photodetector, which generates a voltage output proportional to the timing difference Δt (often expressed as the phase difference $\Delta\theta$) between the arrival of the optical pulses and the phase of the RF signal. When the temporal center of gravity of the pulses aligns precisely with the zero-crossings of the RF signal, both pulses experience identical modulation depths. In this condition, the balanced photodetector outputs a zero signal, indicating that the optical pulses are in phase with the RF signal. Any deviation between the optical pulses center of gravity and the zero-crossings of the RF signal results in a non-zero voltage output from the photodetector, which corresponds to the phase or timing difference between the two inputs. An RF phase shifter is employed to ensure that the BOMPD operates at its most sensitive point, where the optical pulses exactly coincide with the zero-crossings of the RF signal.

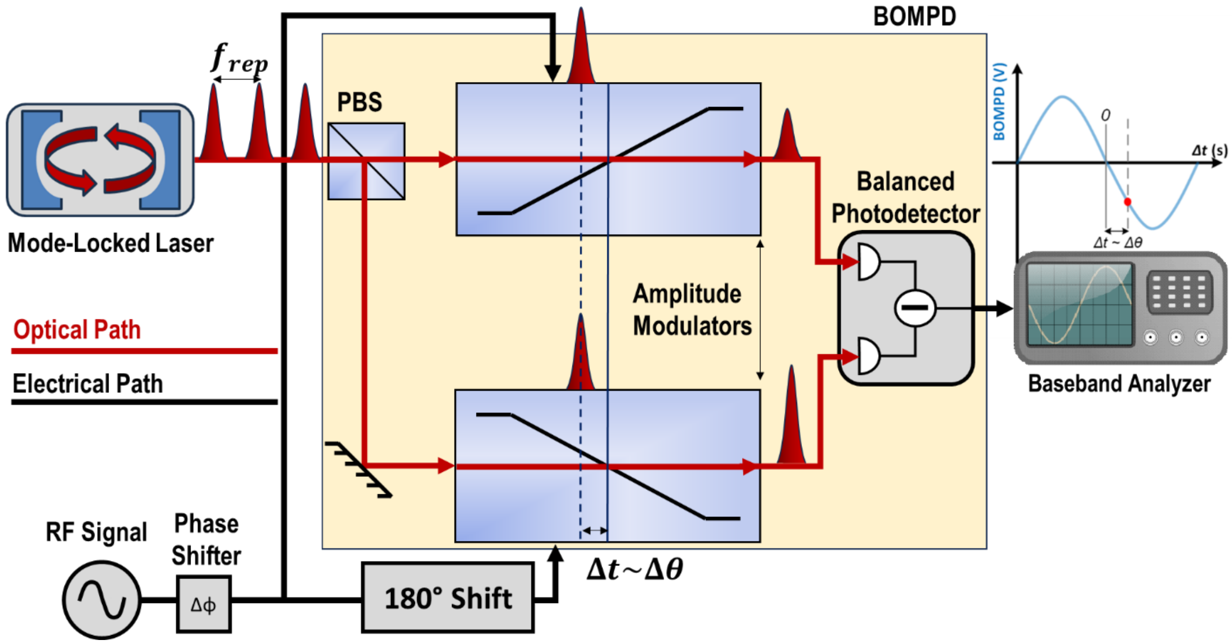

Figure 2-8. Operation of the balanced-optical microwave phase detector.

PBS: Beam splitter; PD: Photodetector; $\Delta\theta$, Δt: Phase/Timing error between Laser and RF Input. Modified from [64]

Figure 2-9 illustrates a second scenario in which the BOMPD is utilized in a synchronization scheme for the generation of optically synchronized RF signals from a voltage-controlled oscillator (VCO). This is facilitated by a PLL, illustrated as the feedback loop between the BOMPD and the VCO. In this configuration, the RF input to the BOMPD is supplied directly by the VCO and is sampled by the optical pulse train generated by the laser. The output of the BOMPD is then fed directly into the feedback loop controlling the VCO's frequency. Any phase or timing error arising from the mismatch between the laser and the VCO is converted into an error voltage signal by the feedback loop. This error signal subsequently adjusts the VCO frequency to align with the repetition rate of the pulsed laser.

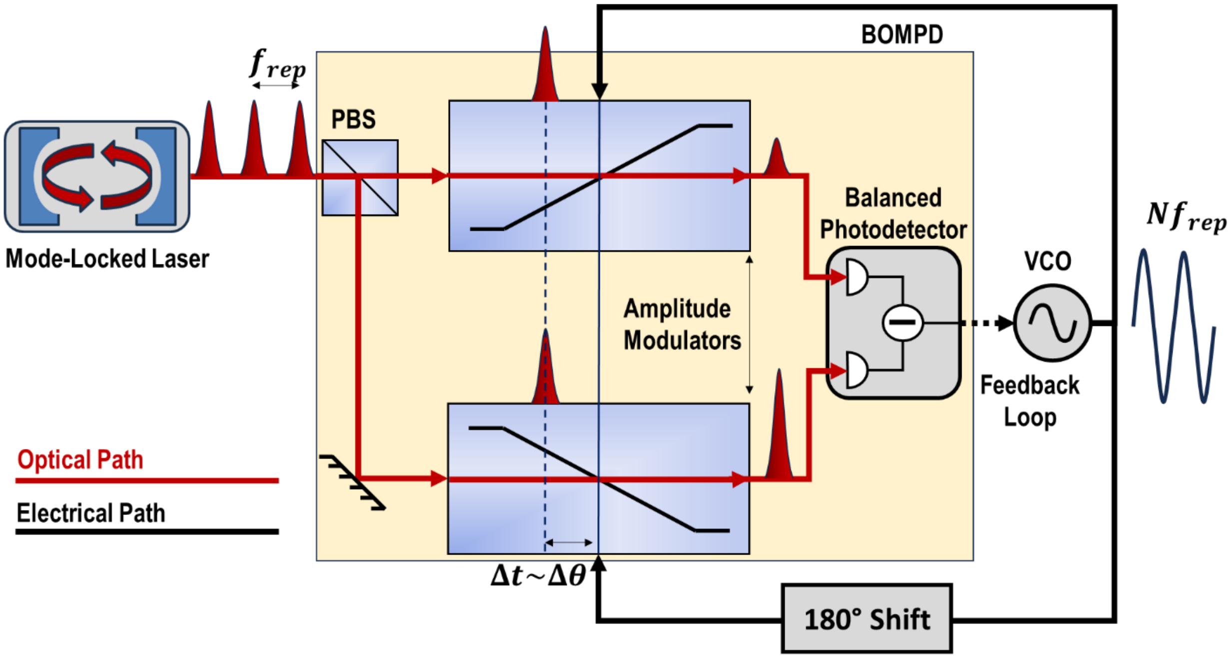

Figure 2-9. BOMPD setup operating as an optoelectronic PLL for RF synthesis with VCO.
PBS: Beam splitter; VCO: Voltage Controlled Oscillator, $\Delta\theta$, Δt: Phase/Timing error between Laser and VCO

A practical implementation of the BOMPD is illustrated in Figure 2-10.a based on [73]. In this setup, the amplitude modulation with a 180° phase shift is done in the optical domain and is achieved by using a Sagnac interferometer (SGI) which incorporates a unidirectional electro-optic phase modulator. The interferometer is constructed with a 50:50 fiber coupler connected to a fiber loop, which ensures a 180° phase shift of the optical pulses when they are recombined at the output. The fiber loop is connected to a unidirectional electro-optic phase modulator, whose unidirectional operation is guaranteed by driving it with a high-frequency RF signal. Furthermore, by splitting the pulses at the input of the Sagnac loop and allowing them to travel in opposite directions, both pulses are subjected to identical environmental fluctuations. During balanced detection, these common noise factors cancel out, resulting in a drift-free bias point.

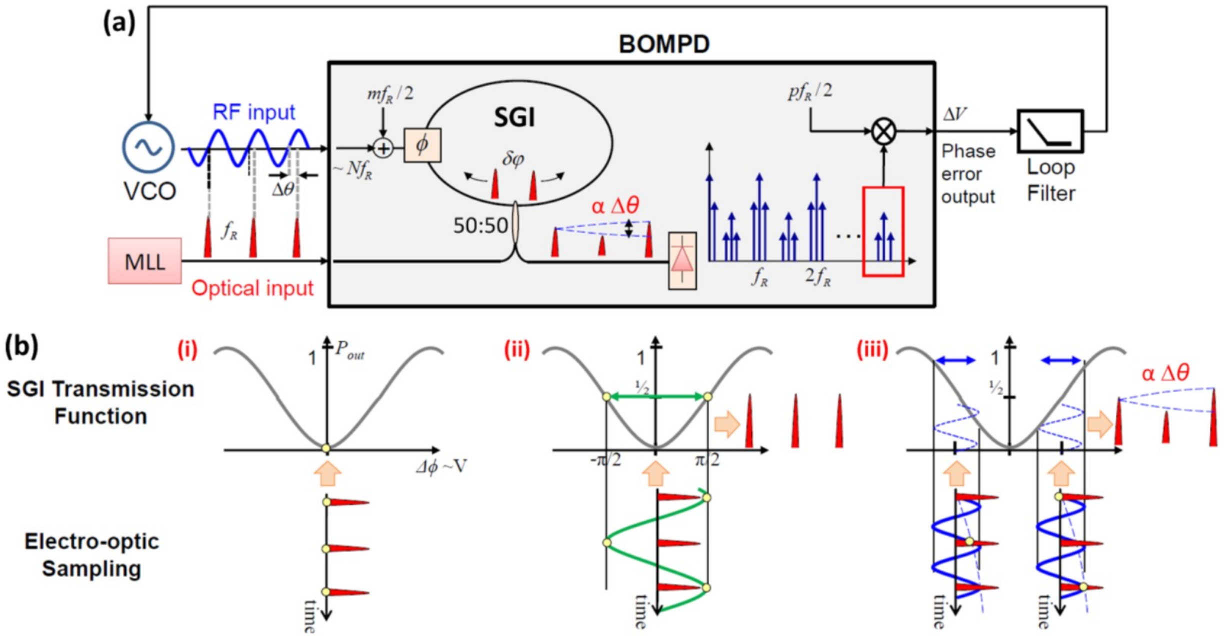

Figure 2-10. Operation principles of the BOMPD and Sagnac Loop Interferometer (SGI).

Taken from [73]. (a) General schematic to synchronize a VCO to a mode-locked laser. (b) Electro-optic sampling in Sagnac-interferometer for different biasing conditions of the phase modulator; (i) no modulation, (ii) modulation at alternating quadrature bias (i.e., $mf_R/2$), (iii) modulation with VCO signal in addition to the quadrature bias. MLL: mode-locked laser; SGI: Sagnac-interferometer; 50:50: fiber coupler; BOMPD: balanced optical-microwave phase detector.

The electro-optical phase modulator (EOM shown as ϕ in Figure 2-10.a) is driven by the target microwave signal from the VCO combined with a bias signal. The bias signal ensures that the detector operates at its most sensitive point. At the BOMPD output, the voltage ΔV represents the phase error $\Delta\theta$ [73], [77].

To provide a more detailed understanding of this phase detection mechanism, an analysis of the SGI in terms of power is presented below. This derivation is based on [64] and is given by Eq. 2-2.

$$P_{out} = P_{in}\sin^2(\varphi/2)$$

Equation 2-2

Here, φ represents the phase difference between the counter-propagating pulses within the SGI. As depicted in Figure 2-10.b, in the absence of modulation (case i, when $\varphi = 0$), destructive interference occurs, resulting in zero output at the SGI.

In the second scenario (case ii), the SGI is driven by the bias signal at its maximum sensitivity point. To determine this point, the phase difference is calculated by setting the derivative of the output power with respect to the phase to zero:

$$\frac{dP_{out}}{d\varphi} = \frac{P_{in}}{2}\sin(\varphi) = 0$$

Equation 2-3

This yields maximum sensitivity when $\varphi = \pm\pi/2$, achieved by applying an alternating quadrature bias. Quadrature bias can be generated by photodetecting an odd harmonic of the mode-locked laser and dividing this frequency by two (mf_R / 2 where m is an odd integer). In this case, the phase component at the electro-optic modulator (EOM) is expressed as:

$$\varphi(t) = V_b \sin(\pi(mf_R)t + \Delta\phi)$$

Equation 2-4

Here, V_b and $\Delta\phi$ denote the amplitude of the bias signal and the fixed relative phase between the pulse train and the derived bias signal, respectively. Consequently, the SGI output will be nonzero for $t_n = n/f_R$ (where n is an integer), as $P_{in}(t_n) \neq 0$. The phase modulation signal simplifies to:

$$\varphi(t) = V_b \sin(\pi(mn) + \Delta\phi) = (-1)^n \sin(\Delta\phi)$$

Equation 2-5

The bias signal ensures constant power at the SGI output when $\varphi(t) = \pm\pi/2$, resulting in:

$$P_{out} = P_{in}\sin^2(\pm\pi/4) = P_{in}/2$$

Equation 2-6

Achieving this requires controlling either the bias voltage or its relative phase. Most BOMPD implementations employ a phase shifter to optimize the sensitivity of the SGI.

In the third scenario (case iii), a microwave signal is applied to the RF input of the BOMPD. The VCO signal must match the laser repetition frequency or one of its harmonics (Nf_R). This signal is combined with the bias signal from the laser and applied to the phase modulator. The modulated phase is then a function of the RF and bias signals:

$$\varphi(t) = V_o \sin(2\pi(Nf_R)t + \Delta\theta) + V_b \sin(\pi(mf_R)t + \Delta\phi)$$

Equation 2-7

Here, V_o and $\Delta\theta$ represent the amplitude of the RF signal and the phase difference between the optical pulse train and the RF signal, respectively. For a small phase difference($\Delta\theta \ll 1$), the modulated phase at the SGI output, after recombination at $t_n = n/f_R$, becomes:

$$\varphi(t) \approx V_o\Delta\theta + (-1)^n\pi/2$$

Equation 2-8

Substituting Eq. 2-8 into Eq. 2-2 yields:

$$P_{out} = P_{in}[1 + (-1)^n \sin(V_o\Delta\theta)]/2$$

Equation 2-9

From Eq. 2-9, it can be observed that the SGI output is an amplitude-modulated signal, with the modulation depth depending on the phase difference between the RF signal at the BOMPD input and the optical pulse train. This phase difference can be extracted via photodetection and filtering of the amplitude modulation sidebands, providing critical information for further characterization or synchronization applications.

2.2.2. Timing Sensitivity Characterization

Having established the BOMPD as a timing detector between optical and microwave signals, it is now essential to characterize its timing sensitivity. To achieve this, the experimental setup shown in Figure 2-11 is used. A mode-locked laser with a 400 MHz repetition rate (MENHIR-1550) and an average output power of 5 mW serves as the optical input. A signal generator (R&S® SMA100B) is used to produce various microwave signals at an RF power level of 13 dBm.

Since the BOMPD is capable of operating with any harmonic of the optical pulse repetition rate, three different microwave frequencies are selected to examine the relationship between the RF frequency at the input and the resulting timing sensitivity. Specifically, frequencies of 1.2 GHz, 5.2 GHz, and 10 GHz are chosen, corresponding to the 3rd, 13th, and 25th harmonics of the laser's repetition rate, respectively.

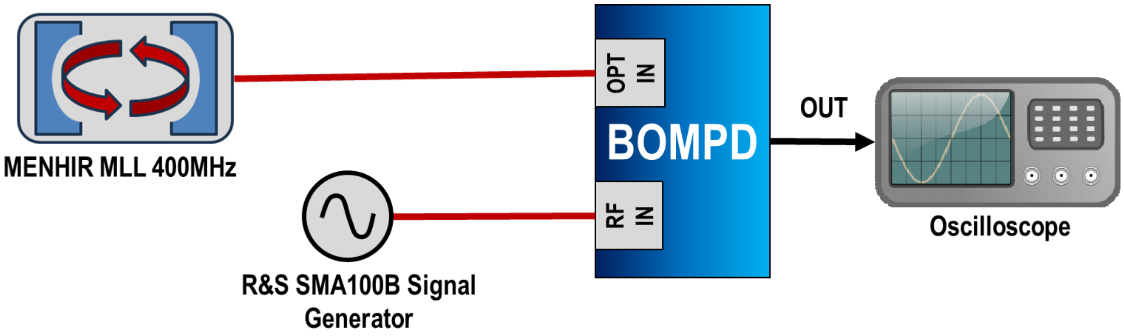

Figure 2-11. Timing sensitivity characterization for the BOMPD.

The timing sensitivity of the BOMPD is defined by the linear slope of its response voltage near the zero-crossing point, as a function of the relative delay between the two inputs [72]. Figure 2-12 illustrates the measured timing sensitivity of the BOMPD at various microwave frequencies, using a 4 MHz detector bandwidth. The results reveal a clear trend: timing sensitivity increases with higher microwave frequencies.

This increase can be attributed to the stronger electric fields associated with higher-frequency microwaves, which induce larger phase changes in the electro-optical modulator. Using these moderate input power levels, the BOMPD demonstrates exceptional timing sensitivities of 0.26 mV/fs, 1.54 mV/fs, and 2.42 mV/fs at frequencies of 1.2 GHz, 5.2 GHz, and 10 GHz, respectively.

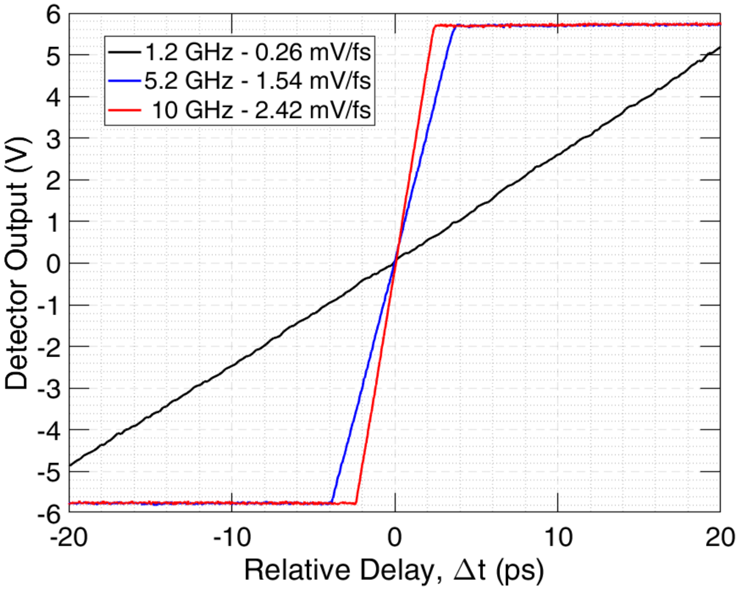

Figure 2-12. Measured BOMPD timing sensitivity at different microwave frequencies.
Black curve at 1.2 GHz, blue curve at 5.2 GHz and red curve at 10 GHz. The measurements are done at 1 MΩ termination.

2.2.3. Noise Floor Characterization

The noise floor of the BOMPD is defined as the detector's response in the absence of a microwave input, with the SGI properly balanced and the optical input present. Figure 2-13 shows the measured noise floor of the BOMPD, scaled at different microwave frequencies. Since the noise floor is measured with the microwave source turned off, all three measurements yield the same integrated voltage value of 0.38 mV RMS at 50Ω, integrated over a 1 Hz to 1 MHz bandwidth. The graph on the right in Figure 2-13 shows the corresponding jitter spectral densities, scaled according to the measured timing sensitivities. When these densities are integrated, as shown on the left, they provide the total noise floor values of the BOMPD over the same bandwidth. The resulting values are 2.92 fs RMS, 0.49 fs RMS, and 0.31 fs RMS at 1.2 GHz, 5.2 GHz, and 10 GHz, respectively.

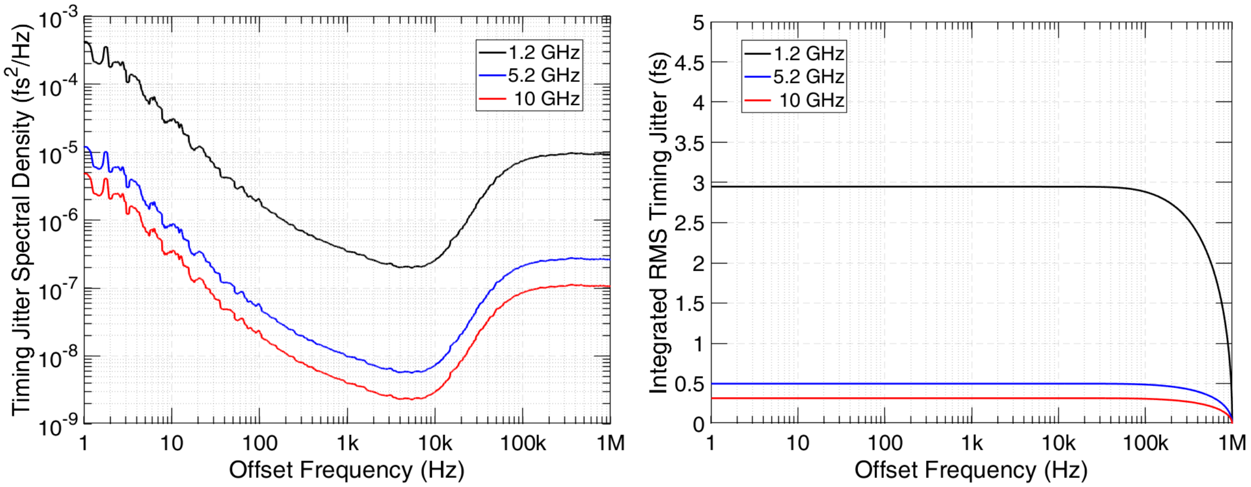

Figure 2-13. Measured BOMPD noise floor scaled at different microwave frequencies.

Black curve at 1.2 GHz, blue curve at 5.2 GHz and red curve at 10 GHz. Left: timing jitter spectral densities; and right: their integrated RMS timing jitter. The measurements are done at 50 Ω termination

2.2.4. Residual Timing Jitter Characterization

Once the timing error between the two input sources is measured, a feedback loop can be implemented on the frequency actuator of one source to synchronize it with the other. In this setup, an analog proportional-integral (PI) controller (LB1005) is employed at the output of the BOMPD. The controller's output is directed to the intracavity mirror actuator of the laser. To minimize timing jitter, the feedback parameters P and I are carefully optimized monitoring the output in a commercial phase noise analyzer (R&S® FSWP, see Appendix A.3).

Figure 2-14 shows the measured residual timing jitter between the optical and microwave signals. A locking bandwidth exceeding 70 kHz is achieved for all tested microwave frequencies, as indicated by the peaks of the three curves, due to the low noise floor provided by the BOMPD. At 5.2 GHz and 10 GHz, the locking bandwidth can be extended further, reaching approximately 100 kHz, because of the enhanced timing sensitivity at higher frequencies.

Below the locking bandwidth, the feedback loop effectively suppresses the timing jitter. However, above this bandwidth, the residual jitter represents the unsuppressed noise between the two sources. Notably, integrated residual timing jitter values as low as 5.94 fs RMS, 4.72 fs RMS, and 4.57 fs RMS are achieved at RF input frequencies of 1.2 GHz, 5.2 GHz, and 10 GHz, respectively.

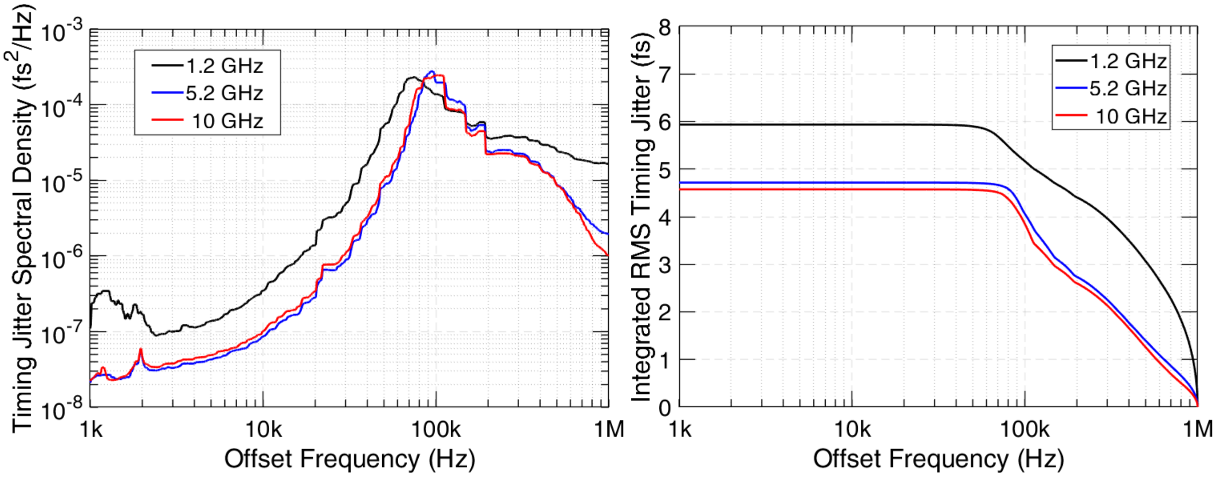

Figure 2-14. Measured residual timing jitter between the optical and RF signals at different frequencies.

Black curve at 1.2 GHz, blue curve at 5.2 GHz and red curve at 10 GHz. Left: timing jitter spectral densities; and right: their integrated RMS timing jitter. The measurements are done at 50 Ω termination.

3. MODE-LOCKED LASER CHARACTERIZATION AND MICROWAVE SYNTHESIS

This chapter addresses the characterization of timing jitter and phase noise in mode-locked lasers, which are utilized as optical sources for photonic microwave oscillators (PMOs). Various methods for such characterization are presented, along with their features and limitations. Subsequently, the process of synthesizing microwave signals from ultra-short optical pulses is described, beginning with the properties and characteristics of photodetectors and progressing to the identification of noise sources and strategies for mitigating them. These steps are critical for ensuring the accurate transfer of timing properties from the optical to the microwave domain.

3.1. TIMING JITTER CHARACTERIZATION OF MODE-LOCKED LASERS

As discussed in Section 1.3, mode-locked lasers are the optical sources selected for the photonic microwave oscillator setup in this project due to their unparalleled phase noise performance at higher offset frequencies. The timing information in mode-locked lasers is encoded in their highly precise repetition rates. However, random fluctuations in the temporal spacing between consecutive pulses, known as timing jitter, lead to variations in the repetition rate. A brief overview of the noise sources in mode-locked lasers and the coupling mechanisms leading to timing jitter and phase noise can be found in Appendix B.1.

Characterizing the timing jitter of the chosen mode-locked laser is essential for constructing a photonic microwave oscillator. Selecting a laser with the lowest possible noise ensures that the synthesized microwave signals inherit superior timing and phase noise properties from the optical source.

This section presents the methods employed for phase noise characterization of mode-locked lasers. Understanding these methods not only provides insights into the laser's phase noise but also underpins the design of the photonic microwave oscillator. Notably, one of these methods is integrated as a key component to stabilize and reduce the laser's noise.

3.1.1. Microwave Phase Detection upon Photodetection Method

This technique relies on microwave extraction through direct photodetection and is one of the simplest approaches for phase noise characterization. It uses a photodiode to generate electronic photocurrent pulses out of the optical pulse train coming from the laser, at the same repetition rate (a detailed explanation of the photodetection of ultrashort pulses is presented in Section 3.2). By filtering the fundamental frequency of the electronic photocurrent pulses, corresponding to the repetition rate of the laser, the phase noise can be directly measured using a signal source analyzer.

In this setup, the well-characterized local oscillator within the signal source analyzer is tuned to the carrier frequency, allowing the phase noise power spectral density of the laser under test to be measured. However, the method is constrained by the quality of the measurement equipment, particularly the photodetector and the local oscillator in the analyzer. Limitations in the internal circuitry and configuration of the signal source analyzer may also introduce measurement inaccuracies.

For the development of this work, the R&S® FSWP signal source analyzer was predominantly used. Details of its phase noise measurement capabilities are provided in Appendix A.3. Figure 3-1 illustrates the schematic of the measurement setup.

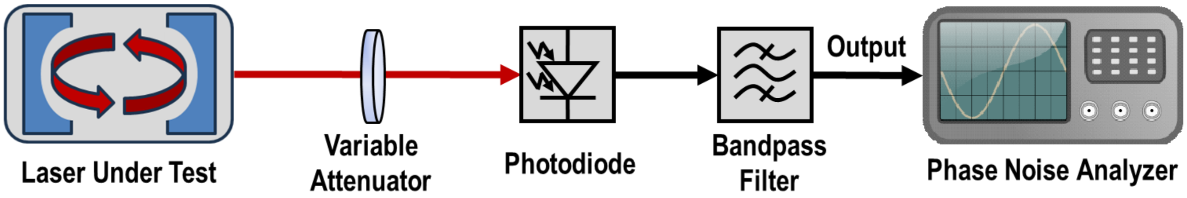

Figure 3-1. Schematic representation of direct phase noise measurement.

This type of measurement is commonly referred to as the Absolute Phase Noise of the RF signal under test, as it is measured relative to the calibrated local oscillator of the measurement device rather than a reference source within a synchronization scheme.

Several factors can negatively influence this type of measurement. Notably, the residual frequency modulation (FM) of the signal source analyzer's local oscillator can introduce additional phase noise into the measurement. This added noise can be either up-converted or down-converted by the mixers. Furthermore, the noise floor of the analyzer imposes a fundamental limitation. For instance, while the noise floor of the R&S®FSWP can be reduced from a few femtoseconds to tens of attoseconds, achieving such low values requires a higher number of correlations during the measurement process, which significantly increases the measurement duration. Figure 3-2 illustrates the achievable noise floor at various carrier frequencies for a single correlation using the FSWP [79].

From the perspective of photodetection, limitations are also introduced by the laser source itself. A high relative intensity noise (RIN) laser source can lead to excess AM-to-PM noise conversion in the photodetection [80], adversely affecting phase noise measurements. Additionally, shot noise at the photodetector can contribute to elevated noise floors, a topic that will be explored further in Section 3.2.

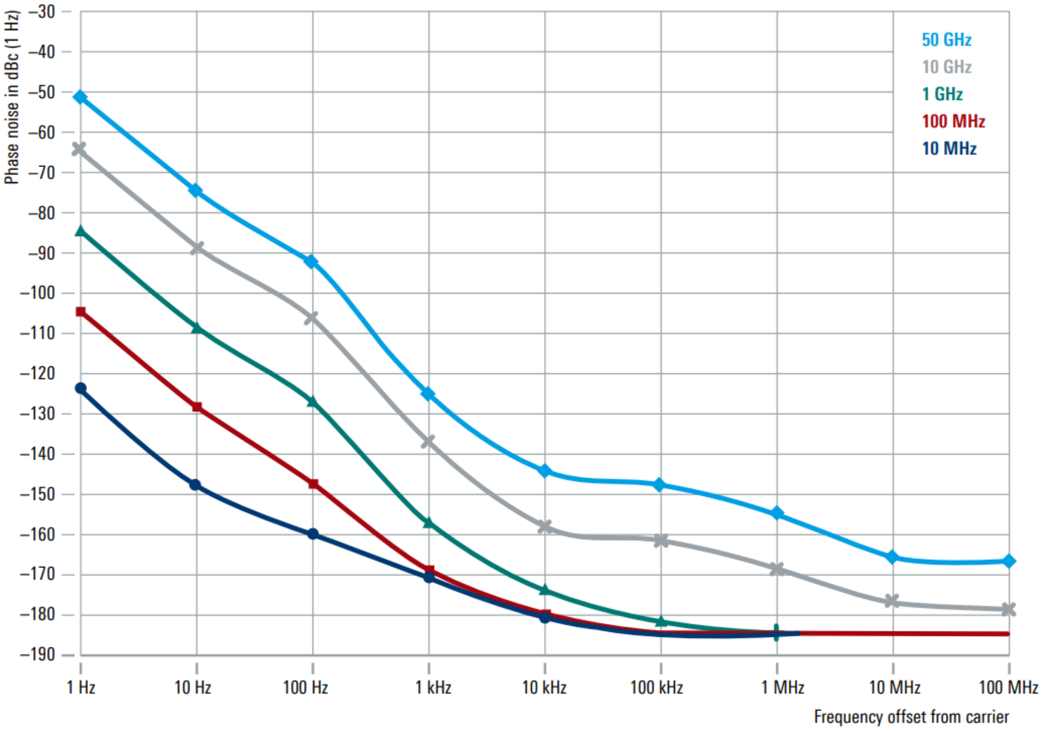

Figure 3-2. Noise floor for phase noise measurement using the R&S® FSWP Signal Source Analyzer at various carrier frequencies.

Taken from manufacturer specifications [80]

3.1.2. Optical Timing Detection Method

Another widely used method for optical phase noise characterization in mode-locked lasers involves balanced optical cross-correlators (BOCs) [63]. These devices are ideal for such measurements due to their attosecond-level timing resolution and inherent immunity to amplitude fluctuations, as discussed in Section 2.1.

The setup typically requires two identical optical sources. Figure 3.3 illustrates the experimental arrangement for timing jitter characterization of mode-locked lasers using BOC, as described in Section 2.1.2. This setup necessitates two mode-locked lasers operating in a master-slave configuration with synchronized repetition rates [81], [82].

The pulse trains from both lasers are fed into the optical inputs of the BOC. The BOC's output serves as an error signal in a PLL configuration, which includes a PI servo controller. This controller drives the piezoelectric transducer (PZT) of the slave laser, locking its repetition rate to that of the master laser. For this characterization method, a low locking bandwidth is preferred to capture a broader range of common noise between the two sources as will be shortly discussed.

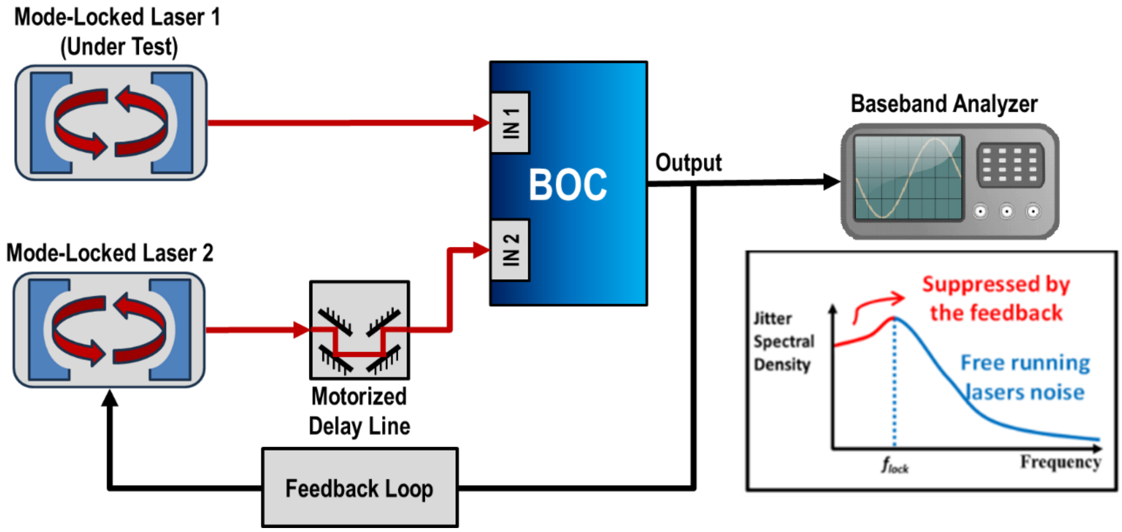

Figure 3-3. Experimental setup for phase noise measurement using a BOC as a timing detector with two synchronized mode-locked lasers.

The electronic power spectral density of the BOC output, measured while both lasers are locked, is analyzed using a baseband spectrum analyzer. This data is then converted into a timing jitter spectral density using the known timing sensitivity of the BOC.

With the lasers locked, their intrinsic timing jitter becomes observable at frequencies beyond the locking bandwidth. This jitter is used to characterize the free-running noise of the lasers, assuming that both lasers operate with a common phase noise. The measured value is divided in two to account for the contribution of each laser.

The effect of the BOC's locking bandwidth on the measured timing jitter is best analyzed using a feedback loop model, as shown in Figure 3-4 and described in [83].

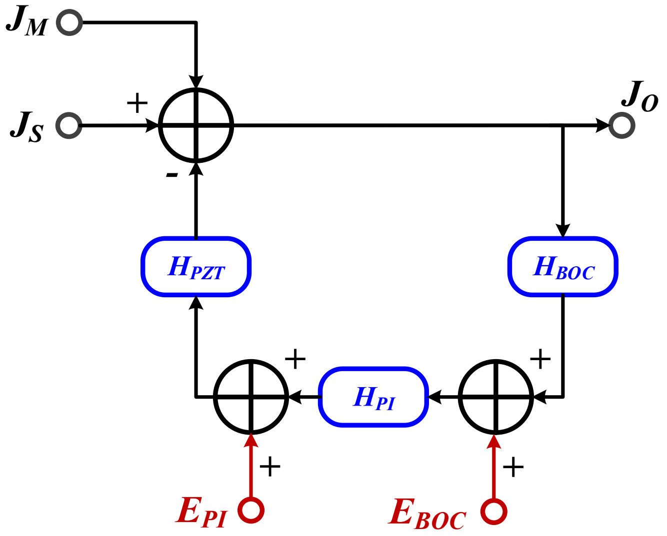

Figure 3-4. Feedback loop model for laser synchronization using a BOC as the error signal generator.

J_M and J_S: free-running jitter of the master and the slave laser; J_O: relative jitter between the two lasers at the BOC input; H_{BOC}, , H_{PI} and H_{PZT}: transfer functions of the BOC, PI controller and slave laser's PZT, respectively; $E_{BOC}$and E_{PI}: electronic noise of the BOC and the PI controller, respectively [64]

In this model, the timing jitter between the master and slave lasers is converted into a voltage signal by the BOC, following a transfer function H_{BOC}. This signal also includes electronic noise from the detector, denoted as E_{BOC}.

Following this model, timing jitter between the master and the slave laser is converted to a voltage signal by the BOC following a transfer function H_{BOC}, along with the electronic noise of detector noise E_{BOC}. This voltage signal is subsequently processed by the PI controller, which has its own transfer function H_{PI} in a negative feedback configuration. Finally, the output from the PI controller, combined with its electronic noise E_{PI}, is amplified and converted back into a time delay by the slave laser's PZT, represented by the transfer function H_{PZT}.

The resulting relative timing jitter between the two lasers at the BOC input can be expressed as:

$$J_O = J_M + J_S + [-(J_O H_{BOC} + E_{BOC})H_{PI} + E_{PI}]H_{PZT}$$

Equation 3-1

Here, J_M and J_S represent the free-running jitter of the master and slave lasers, respectively.

By defining the electronic noise jitter term J_N and the total transfer function H as follows:

$$J_N = -E_{BOC}H_{BOC} + E_{PI}H_{BOC}H_{PI} \quad H = H_{BOC}H_{PI}H_{PZT}$$

Equation 3-2

Equation 3-1 simplifies to:

$$J_O = \left(\frac{1}{1+H}\right)(J_M + J_S) + \left(\frac{H}{1+H}\right)J_N$$

Equation 3-3

Since J_M, $J_S$and J_N are uncorrelated noise sources, the mean values of their cross-products are zero. Consequently, the average timing jitter spectral density detected by the BOC is given by:

$$\bar{J_O} = \left|\frac{1}{1+H}\right|^2 (\overline{{J_M}^2} + \overline{{J_S}^2}) + \left|\frac{H}{1+H}\right| \overline{{J_N}^2}$$

Equation 3-4

From Equation 3-4, it is evident that three main contributions determine the output timing jitter measured by the BOC: the free-running timing jitter of the master laser, the free-running timing jitter of the slave laser, and the system's electronic noise.

Assuming the master and slave lasers are identical, the coefficients are defined $C_M = |1/(1+H)|^2$ and $C_N = |H/(1+H)|^2$. Substituting these into Equation 3-4, it is obtained:

$$J_O = 2C_M\overline{{J_M}^2} + C_N\overline{{J_N}^2}$$

Equation 3-5

If H≈0, implying C_M≈1 and C_N≈0, the measured timing jitter at the BOC output originates almost entirely from the master laser's timing jitter. This gives the upper limit for J_M as half of the measured timing jitter:

$$\overline{J_M}^2 \approx \frac{\overline{J_O}^2}{2} - \frac{1}{2}C_N\overline{J_N}^2 \leq \frac{1}{2}\overline{J_O}^2$$

Equation 3-6

To explore the effects of locking bandwidth on timing jitter measurement, the transfer functions in Figure 3-4 are defined as:

$$H_{BOC} = \frac{K_{BOC}}{s + 2\pi f_{BPD}} \quad H_{PI} = \frac{K_{PI}}{s + 2\pi f_{PI}} \quad H_{PZT} = \frac{K_{PZT}}{f_R s}$$

Equation 3-7

Defining the overall feedback loop gain as $K = K_{BOC} + K_{PI} + K_{PZT}$, as described in [66], the locking bandwidth can be expressed as [84]:

$$f_{locking} = \sqrt{\frac{K}{2}\left[K - 2f_{PI} + \sqrt{(K - 2f_{PI})^2 + 4f_{PI}^2}\right]}$$

Equation 3-8

This relationship shows that the locking bandwidth is directly proportional to the overall feedback loop gain and the corner frequency of the PI controller (f_{PI}). Using the laser characteristics detailed in Appendix B.2, the achievable locking bandwidth for this type of laser can be determined by tuning the PI parameters in the loop filter controller. Figure 3-5 illustrates the simulated locking bandwidth for this specific laser using different PI parameters.

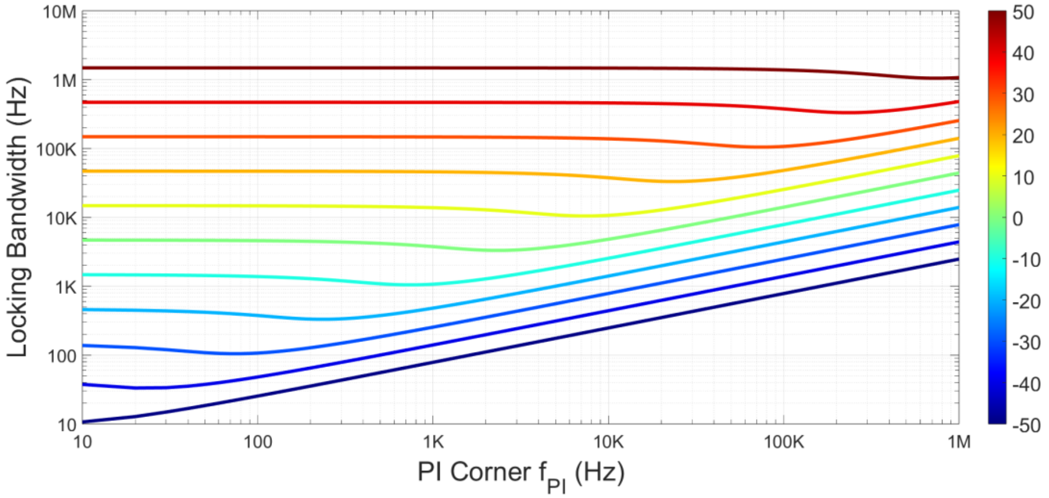

Figure 3-5. Locking bandwidth dependance on P gain and I frequency corner for the timing jitter characterization of two identical 1 GHz repetition rate mode-locked lasers.

BOC timing sensitivity fixed at 0.2 mV/fs and PZT gain at 146.7 Hz/V

Since the primary interest lies in measuring the intrinsic laser noise rather than the extent to which noise can be reduced within this scheme, it is preferable to select the lowest gain possible. This approach maximizes the dynamic range for timing jitter measurement. However, this process is non-trivial, as reducing the gain too much may compromise the locking state of the two lasers. A lower gain can lead to an unstable lock, adversely affecting the overall measurement accuracy.

In practice, this measurement was performed using the 1 GHz MENHIR lasers described in Appendix B.2, following the test procedure outlined in Figure 3-3. For this experiment, the frequency corner f_{PI} was set at 100 Hz, while the proportional gain of the controller varied from 50 dB down to -5 dB. The experimental results are shown in Figure 3-6.

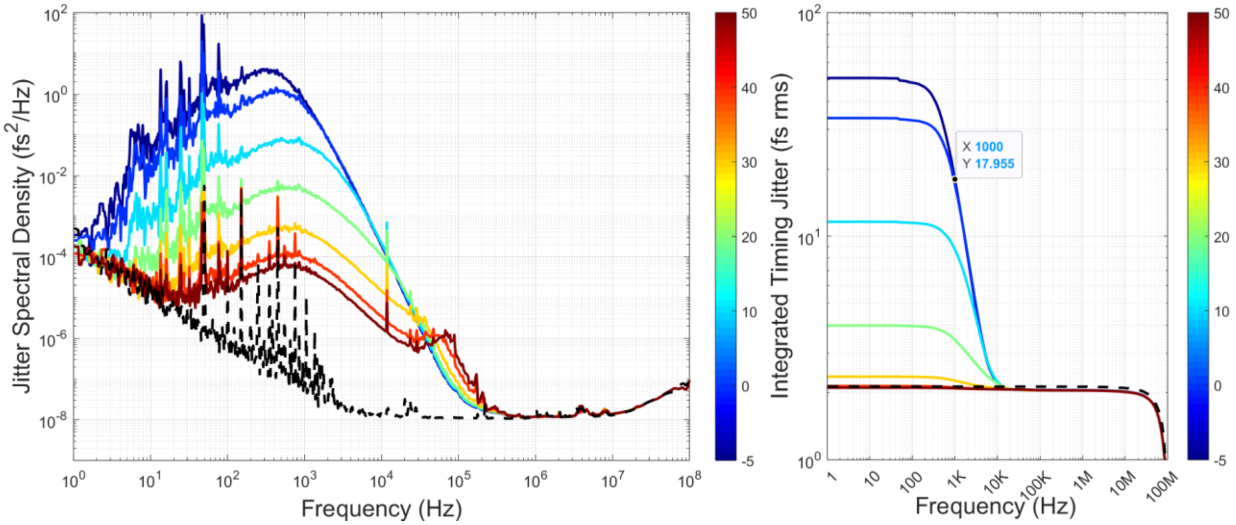

Figure 3-6. Measured jitter spectral density and integrated timing jitter for a 1 GHz mode-locked laser characterized using the optical timing detector method.

Measurement performed with BOC timing sensitivity at 0.2 mV/fs, optical power at the input of the BOC to be 5 mW from each laser and balanced photodetector bandwidth at 150 MHz

The results demonstrate that reducing the proportional gain of the controller provides greater access to the timing jitter of the laser under test. By decreasing the gain to -5 dB, a locking bandwidth around 1 kHz was achieved, as simulated in Figure 3-5. Although further reduction in gain could theoretically enable even lower locking bandwidths, this was not feasible in practice. Beyond this point, the PLL became too unstable, causing the locking between the two lasers to fail.

At the lowest gain, the integrated timing jitter from 100 MHz down to 1 kHz was measured at approximately 18 fs RMS, as shown in the right graph of Figure 3-6. However, the measurement process faced a limitation due to the bandwidth-to-gain relationship in the balanced photodetector used for the BOC. For broader noise characterization at 150 MHz, the photodetector operates with its highest bandwidth but also its lowest gain, which, in this scenario, was only 0.2 mV/fs. This limitation meant that for measurements above 1 MHz, the results were constrained by the noise floor of the BOC itself.

Even attempts to increase the BOC gain to reduce the noise floor did not improve the overall performance significantly. The minimum achievable feedback loop gain K remained constant, imposing a higher limit on the proportional gain. Consequently, the locking bandwidth for this specific laser was restricted to being around the 1 kHz range under the given conditions.

3.1.3. Optical Delay-Line Method

A third method for characterizing timing jitter is the optical delay-line method, which uses a time-delayed version of the optical pulse train under test rather than requiring two identical mode-locked lasers. Figure 3-7 illustrates the experimental setup for this timing jitter measurement scheme.

This method is inspired by delay-based techniques traditionally used in microwave characterization [85], and it has recently been adapted for optical applications [62], [86]. Unlike interferometric methods [87], this approach takes advantage of the high timing sensitivity provided by BOCs [88].

In this setup, the optical pulse train from the laser is split into two paths. One path passes through a delay line—implemented here using a fiber delay line—where the delay converts frequency fluctuations into phase fluctuations. The delay is sufficiently long to ensure that the two pulse trains become uncorrelated. Additionally, the signals in both paths are configured to be orthogonal to each other. These two pulse trains are then fed into the BOC, which acts as a phase detector.

When the laser pulses overlap with their delayed versions, the BOC generates a voltage spectral density proportional to the jitter spectral density.

The free-running jitter spectral density of the mode-locked laser, $S_{\Delta t}(f)$, can then be determined using the following relationship:

$$S_{\Delta t}(f) = \frac{S_{BOC}(f)}{2(1 - \cos(2\pi f \tau))}$$

Equation 3-9

Here, $S_{BOC}(f)$ represents the jitter spectral density measured by the BOC, and τ denotes the delay time given by the length of the fiber delay line [62], [63].

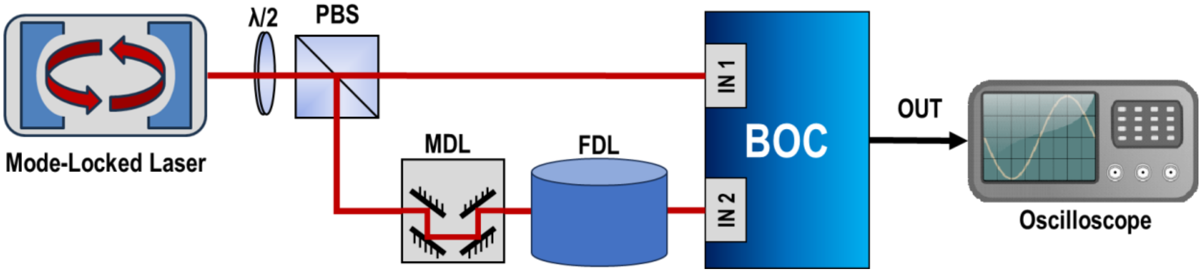

Figure 3-7. Timing jitter measurement setup using delay line phase noise method.

PBS: Polarization beam splitter, MDL: motorized delay line, FDL: Fiber delay line

3.1.4. Optical Timing Jitter Methods Compared

To better understand the performance of each method described in the previous sections, a measurement of timing jitter of the 1 GHz mode-locked laser detailed in Appendix 2.3 is performed. Figure 3-8 presents a comparison of the phase noise spectra of this laser at a 10 GHz equivalent carrier frequency, measured using the three methods.

- **Curve (i)** shows the absolute phase noise measured by the phase noise analyzer (R&S® FSWP). Notably, this curve reaches the analyzer's noise floor at approximately 50 kHz.
- **Curve (ii)** depicts the phase noise measurement using the timing-detector method. With a locking bandwidth of around 700 Hz, the method suppresses noise below this frequency, which does not reflect the laser's actual phase noise. Above the locking bandwidth, the measured phase noise aligns well with the result from the phase noise analyzer. Due to the lower noise floor of the BOC, the laser's noise is resolved even beyond 50 kHz, reaching -180 dBc/Hz at an offset frequency of approximately 900 kHz.

- **Curve (iii)** shows the results from the timing-delay method, which combines the advantages of the previous two methods. It resolves close-to-carrier phase noise with performance comparable to that of the phase noise analyzer while maintaining a low wide-band noise floor similar to the timing-detector method. The only drawback is the presence of "null points" at harmonics of 1/τ (e.g., ~90 kHz, due to the ~2250 m fiber length used for characterization), where noise detection sensitivity is reduced.

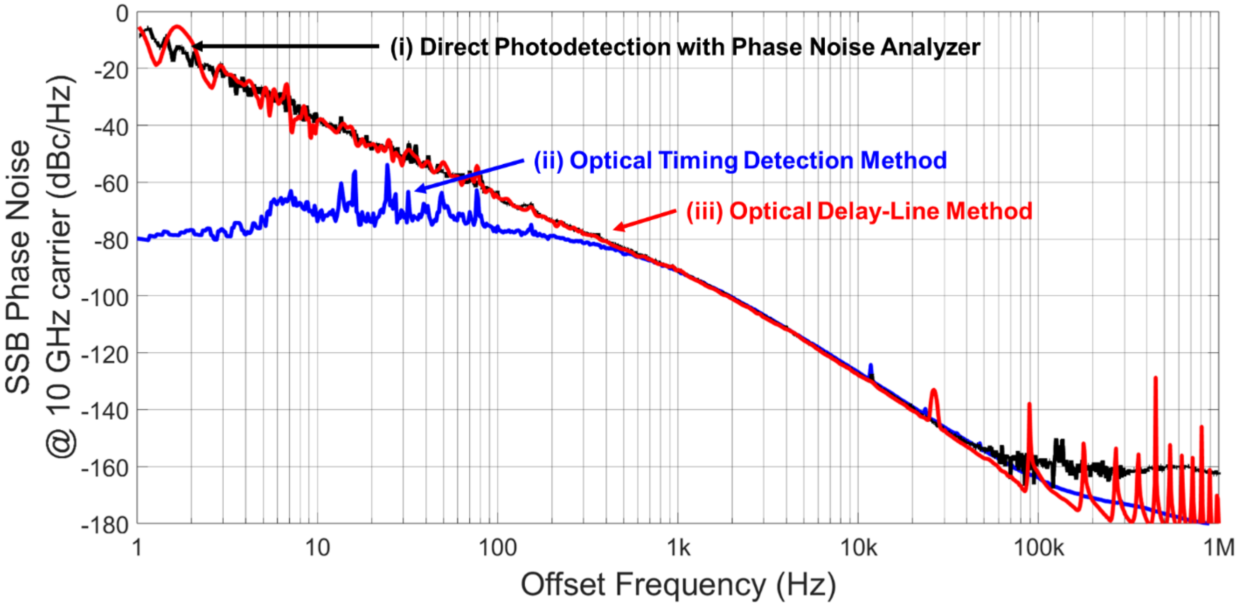

Figure 3-8. Measured phase noise spectra of a mode-locked laser at 10 GHz carrier using (i) a commercial phase noise analyzer, (ii) the timing-detector method and (iii) the timing-delay method.

A comparison of three methods to measure phase noise, namely the absolute phase noise analyzer, the timing-detector method, and the timing-delay method, shows their merits and limitations in assessing the timing jitter of a 1 GHz mode-locked laser.

The phase noise analyzer is a good reference, but it is limited by the noise floor above ~50 kHz. The timing-detector method overcomes this by offering lower noise floors than the phase noise analyzer and detects phase noise up to 900 kHz. However, it is limited by the locking bandwidth that suppresses the noise below ~700 Hz.

The timing-delay method combines the best features of the two preceding techniques, offering a performance close to that of the phase noise analyzer in terms of close-to-carrier noise and at the same time maintaining a low noise floor. A notable drawback is that null points at certain frequencies give rise to reduced sensitivity.

In summary, the timing detector and timing-delay techniques show much better performance than the phase noise analyzer, especially for higher frequencies and lower noise floors. The right choice of method depends on specific requirements of the phase noise measurement in terms of the frequency range and sensitivity needed.

3.2. MICROWAVE SYNTHESIS FROM MODE-LOCKED LASERS

Having established the timing jitter characterization of mode-locked lasers and their exceptional phase noise properties, this section explores the translation of these phase noise characteristics into the microwave domain. The ability to synthesize stable microwave signals from optical frequency combs is essential for applications requiring ultra-low phase noise and high frequency stability.

A comprehensive understanding of photodetection techniques for ultrashort optical pulses is crucial for this process. This section details the mechanism of photodetection, highlighting its fundamental limitations, sources of noise, and its role in the synthesis of high-purity microwave signals. By leveraging the optical frequency comb generated by mode-locked lasers, photodetection enables the transfer of optical frequency stability into the RF domain.

3.2.1. Photodiodes

Photodiodes are fundamental components for bridging the optical and the radiofrequency domains. These semiconductor devices, specifically p-n junctions, operate based on the theory of the photoelectric effect [89]. When photons are absorbed by the photodiode, their energy generates electron-hole pairs within the depletion region, resulting in a photocurrent proportional to the incident photon flux, as illustrated in Figure 3-9.

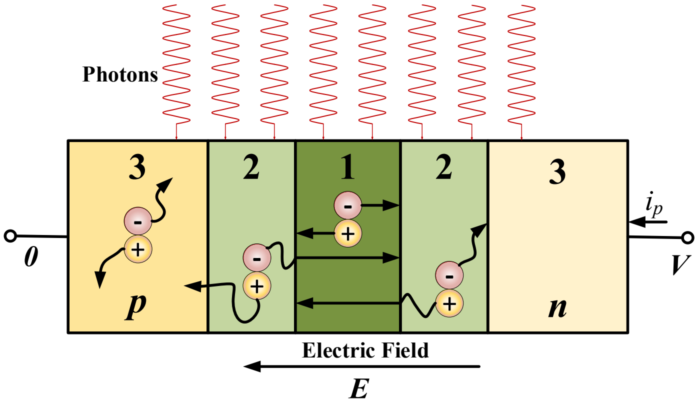

Figure 3-9. Photoelectric phenomena (photoeffect) in photodiodes. Modified from [89].

Figure 3-9 expands on the photoelectric phenomena, or photoeffect, within photodiodes, detailing various regions where photon absorption occurs. Region 1 signifies the depletion region, marked by a strong electric field that efficiently guides electron and holes toward their respective junctions, which significantly enhances the resultant photocurrent. In contrast, electron-hole pairs generated in region 3 contribute minimally to the photocurrent due to quick recombination in the absence of an electric field. Electron-hole pairs formed in region 2 exhibit random drift, partially contributing to the photocurrent.

For synthesizing ultrashort electronic pulses, photodiodes typically function in photoconductive mode. In this mode, a strong reverse bias voltage is applied to the photodiode, creating a photocurrent approximately linearly proportional to the incident photon flux.

In photoconductive mode, a reverse voltage is applied to the photodiode, typically chosen to be high enough to enhance the drift velocity of the charge carriers. This increase in drift velocity widens the depletion region, enlarging the light collection area and reducing the junction capacitance, which in turn improves the photodiode's response time. While the reverse voltage has minimal impact on the photocurrent, it does increase the dark current—the noise current generated in the absence of light. Higher reverse voltages can also lead to increased device heating, potentially causing timing drift and raising thermal noise. Figure 3-10 illustrates the photoconductive mode operation and the current voltage (I-V) characteristics of a photodiode with and without a load.

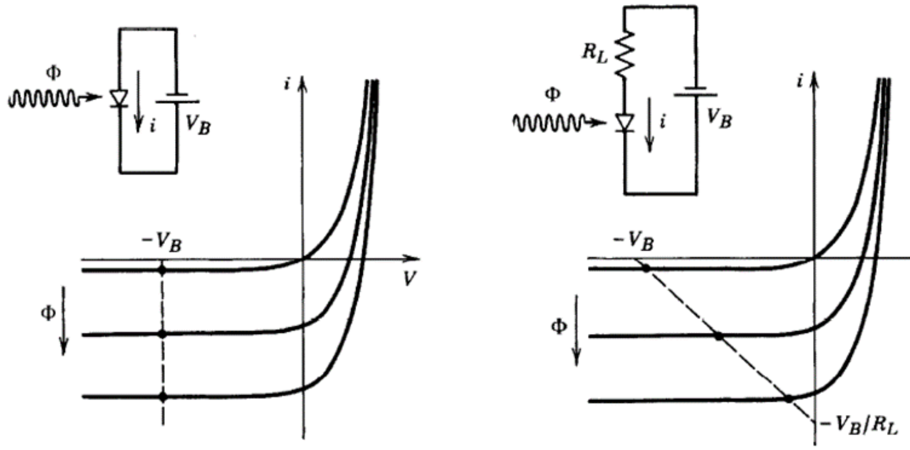

Figure 3-10. I-V characteristics of the photoconductive operation mode on photodiodes, without a load (left) and with a series load in the circuit (right)

v_B bias voltage, R_L: load resistor. Taken from [89].

Photodiodes must balance several requirements to effectively generate microwave signals with a substantial signal-to-noise ratio (SNR): high responsivity, high saturation power, high linearity, low intrinsic noise, and adequate electrical bandwidth. Key characteristics defining photodiodes for this application include:

- *Quantum Efficiency and Responsivity:* Quantum efficiency represents the probability that an absorbed photon generates an electron-hole pair in the depletion region, ranging from 0 to 1. This parameter is closely linked to responsivity, which relates the incident optical power to the resulting photocurrent. Equation 3-10 expresses the average photocurrent as a function of quantum efficiency, with responsivity defined as the ratio between the electron charge and the energy of the incident photon multiplied by the quantum efficiency.

$$i_p = \eta e \Phi = \frac{\eta e P_{opt}}{h\upsilon} = \Re P_{opt}$$

Equation 3-10

Responsivity can also be expressed in terms of the incident photon's wavelength:

$$\Re = \frac{\eta e}{h\upsilon} = \eta \frac{\lambda_o}{1.24} \quad [A/W]$$

Equation 3-11

- *Saturation*: The saturation characteristic of a photodiode indicates its capacity to handle elevated optical power levels without losing linearity in its response. Once optical input power exceeds a certain threshold, the photocurrent generated may no longer increase proportionally, leading to distortion and signal clipping. A high saturation power is essential to maintain signal integrity in applications involving varying light intensities and demanding high linearity.
- *Response Time:* This characteristic refers to the impulse response time of the photodiode, governed by the carrier transit time across the depletion layer as well as the RC response time determined by the device's resistance and capacitance. Factors such as diffusion processes can also impact response times. Modern fabrication techniques may mitigate these limitations, as discussed in Section 3.2.5.
- *Bandwidth:* In the frequency domain, bandwidth is reflective of the impulse response time. The influence of bandwidth on the photodetection of ultrashort pulses will be explored further in Section 3.2.2.

3.2.2. Photodetection of Ultrashort Optical Pulses

While the photoconductive operation mode of photodiodes, as previously described, effectively characterizes the device under continuous optical flux, it is vital to examine the photodiode's behavior when subjected to an optical pulse train, particularly the ultrashort pulses produced by mode-locked lasers. This section provides an analytical description of the photodetection process.

In this context, the optical pulse train is converted into a current-equivalent pulse train by the photodiode. Figure 3-11.a and Figure 3-11.b illustrate the perspective of these pulse trains from both optical and electrical viewpoints. Notably, the photodiode detects only the envelope of the optical pulse train rather than the optical carrier frequencies contained within it. Accordingly, the photodiode down-converts the optical pulse train into a baseband pulse train, preserving the frequency relationships associated with the laser's repetition rate and its harmonics.

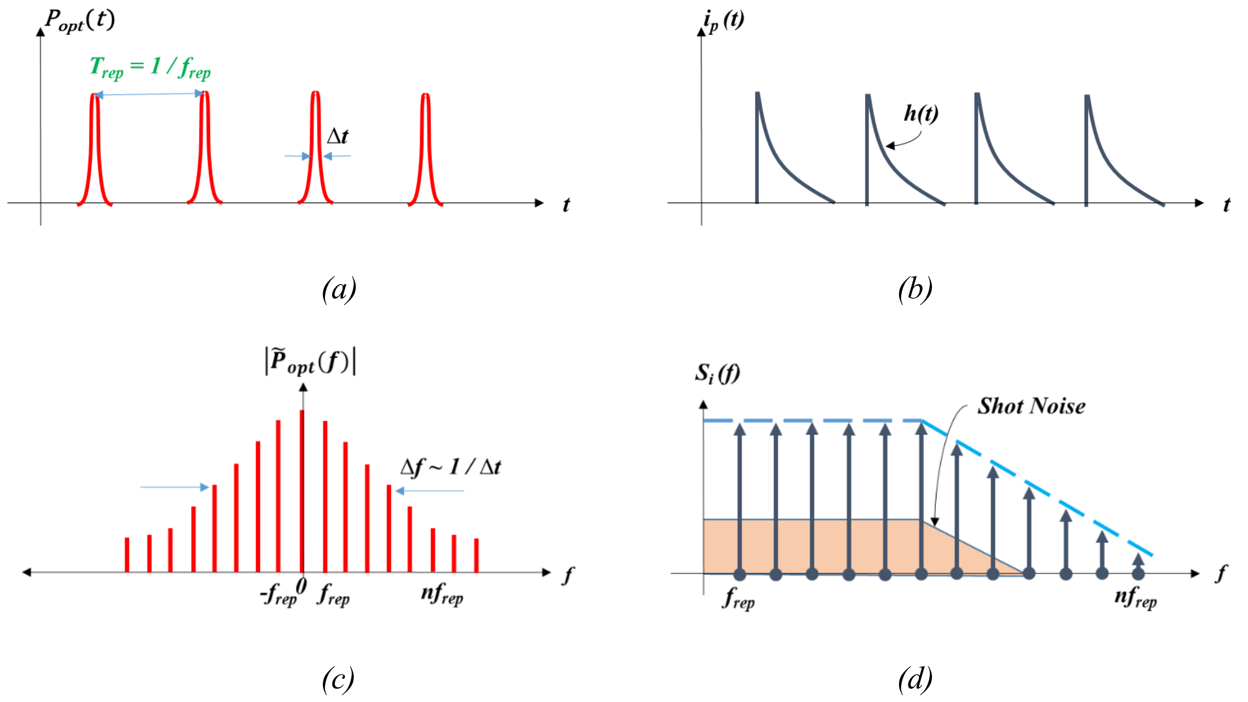

(a) (b) (c) (d)

Figure 3-11. Time and Frequency representation of optical and photodetected pulse trains.

(a) Optical pulse train intensity profile (b) Photocurrent pulse train, where h(t) is the impulse time response of the photodiode. (c) Spectrum of the optical intensity profile. (d) Power spectrum of the photocurrent. Modified from [90]

Figure 3-11.c and Figure 3-11.d present the frequency representations of the optical and electrical pulse trains, exhibiting an array of radiofrequency carriers at the repetition rate and its harmonics. It is crucial to acknowledge that the transformation from the optical pulse train to the photocurrent pulse train is constrained by the impulse response time of the photodiode, denoted as $h(t)$. The mathematical foundations of these phenomena, originally detailed in [89] and expanded upon in [90], [91], will be discussed further.

The photocurrent generated in the diode can be expressed as a summation of pulses, each pulse produced by a photon that has (or has not) generated a free carrier pair:

$$i_p(t) = \sum_k X_k h(t - k\Delta t)$$

Equation 3-12

Here, $i_p(t)$ represents the total photocurrent over time, and the summation includes contributions from the incident photon k. The term X_k is a random variable that indicates whether the absorbed photon generates a free carrier pair within the time interval Δt, taking a value of either 0 or 1.

The probability of successful photodetection within a time interval Δt is given by:

$$\wp = \frac{\eta}{hv} P_{opt}(t)\Delta t = \lambda(t)\Delta t$$

Equation 3-13

where $P_{opt}(t)$ is the optical power as a function of time, and $\lambda(t)$ is the photoelectron rate. For pulsed lasers, the optical power can be expressed in terms of the pulse profile function *f*(*t*), and is periodically separated by a period given by the inverse of the repetition rate:

$$P_{opt}(t) = P_o \sum_{n} f(t - nT_{rep})$$

Equation 3-14

Since the photocurrent depends on a random variable, it is treated as a stochastic process defined by its double-sided Power Spectral Density (PSD). Here $\mathcal{F}_T$ denotes the finite-time Fourier transform, and $\langle\cdot\rangle$ indicates the expected value.

$$S_{i_p}(f) = \lim_{T\to\infty} \frac{1}{T} \langle \left| \mathcal{F}_T\{i_p(t)\} \right|^2 \rangle \qquad [\mathrm{A}^2/\mathrm{Hz}]$$

Equation 3-15

To analyze this process, Equation 3-12 is substituted into Equation 3-15, calculating the cross-spectrum between f and f ':

$$S_{i_p}(f,f') = \lim_{T\to\infty} \frac{1}{T} \langle \mathcal{F}_T \left\{ \sum_{k} X_k h(t - k\Delta t) \right\} * \mathcal{F}_T^* \left\{ \sum_{l} X_l h(t - l\Delta t) \right\} \rangle$$

By defining $\mathcal{F}_T \equiv \int_{-T/2}^{T/2} h(t)\, e^{-i2\pi f t} \equiv H_T$ and rearranging the terms, it is obtained:

$$S_{i_p}(f,f') = \lim_{T\to\infty} \frac{1}{T} \langle \sum_{k} \sum_{l} X_k X_l \cdot H_T(f) H_T^*(f')\, e^{-i2\pi f k\Delta t} e^{i2\pi f' l\Delta t} \rangle$$

As $H_T(f)$ is the finite time Fourier and taking the duration of the pulse way shorter than T, then $H_T(f) = H(f)$:

$$S_{i_p}(f,f') = \lim_{T\to\infty}\frac{1}{T}H(f)H^*(f')\sum_k\sum_l\langle X_kX_l\rangle\cdot e^{-i2\pi fk\Delta t}e^{i2\pi f'l\Delta t}$$

Equation 3-16

The expectation value of the product of the random variables X_k and X_l is derived from Equation 3-13 yielding:

$$\langle X_kX_l\rangle = \begin{Bmatrix}\lambda(k\Delta t)\Delta t & k=l\\ \lambda(k\Delta t)\lambda(l\Delta t)\Delta t\Delta t & k\neq l\end{Bmatrix}$$

Equation 3-17

By substituting Equation 3-17 back into Equation 3-16:

$$S_{i_p}(f,f') = \lim_{T\to\infty}\frac{1}{T}H(f)H^*(f')\sum_k\lambda(k\Delta t)\Delta t\cdot e^{-i2\pi(f-f')k\Delta t}$$
$$+\sum_k\sum_{l\neq k}\lambda(k\Delta t)\lambda(l\Delta t)\Delta t\Delta t\cdot e^{-i2\pi fk\Delta t}e^{i2\pi f'l\Delta t}$$

Taking the limit as $\Delta t \to 0$

$$S_{i_p}(f,f') = H(f)H^*(f')\lim_{T\to\infty}\frac{1}{T}\sum_k\int_{-T/2}^{T/2}\lambda(\tau)\cdot e^{-i2\pi(f-f')\tau}\mathrm{d}\tau$$
$$+\iint_{-T/2}^{T/2}\lambda(\tau)\lambda(\tau')\cdot e^{-i2\pi f\tau}e^{i2\pi f'\tau'}d\tau d\tau'$$

$$S_{i_p}(f,f') = H(f)H^*(f')\lim_{T\to\infty}\frac{1}{T}[\Lambda_T(f-f') + \Lambda_T(f){\Lambda_T}^*(f')]$$

Equation 3-18

Finally, by setting *f = f'*, the double-sided PSD for the photocurrent is obtained:

$$S_{i_p}(f) = |H(f)|^2\lim_{T\to\infty}\frac{1}{T}[\Lambda_T(0) + |\Lambda_T(f)|^2] = |H(f)|^2\left[\lambda_{avg} + S_\lambda(f)\right]$$

Equation 3-19

Thus far, the defined spectral density of the photocurrent produced by the detection of ultrashort pulses in a photodiode is presented. Equation 3-19 shows that the double-sided PSD comprises two terms: the first, given by the average photoelectron rate (related to shot noise, further explained in the next section), and a second term $S_\lambda(f)$ represented as a series of discrete pulses at harmonics of the repetition rate.

As indicated in Equation 3-13, $S_\lambda(f)$ can be related to the power spectrum of the optical intensity profile:

$$S_\lambda(f) = \left(\frac{\eta}{h\nu}\right)^2 S_P(f)$$

Equation 3-20

Where $S_P(f)$ is defined as:

$$S_P(f) = \lim_{T\to\infty} \frac{1}{T} \langle \left| \mathcal{F}_T\{P_{opt}(t)\} \right|^2 \rangle$$

Equation 3-21

It is important to clarify that $S_P(f)$ represents the PSD for the optical intensity profile of the pulse train and does not represent the PSD of the optical electric field. Consequently, all harmonics of the repetition rate are depicted as a baseband double-sided version of the optical electric field spectrum as shown in Figure 3-11.c.

3.2.3. Noise Sources during Photodetection

During photodetection, various noise sources significantly influence the performance and reliability of the detected signals. A comprehensive understanding of these noise sources is crucial for optimizing photodiode operation and enhancing overall signal integrity. This section highlights several key types of noise encountered in optical sources and during the photodetection process.

Figure 3-12 illustrates the different types of noise sources affecting the signal during photodetection. To begin with, the input optical flux is subject to inherent noise due to the discrete and random nature of photon arrival at any given time *T*. This phenomenon is commonly referred to as *quantum* or *photon noise*, which typically follows a Poisson probability distribution, particularly when the light source is a laser [89].

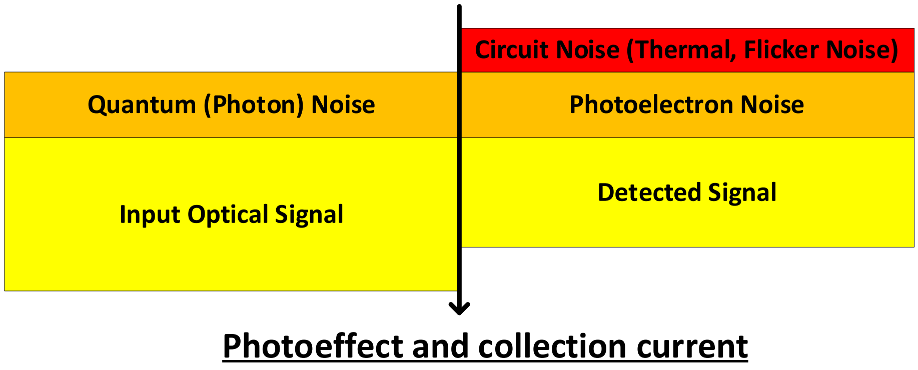

Figure 3-12. Noise sources during photodetection. Adapted from [89].

Once the photoeffect occurs, *photoelectron noise* contributes to the detected signal, particularly in non-ideal receivers where the quantum efficiency is less than 1. This noise source arises from the uncertainty of whether an absorbed photon effectively generates a free carrier pair. Collectively, these two noise phenomena constitute what is generally termed *shot noise*, also referred to as photocurrent noise, as it directly influences the photocurrent generated by the photodiode [90], [91].

Referring to Equation 3-19, which describes the spectrum of the photodetected electrical pulse train, the first term represents shot noise, directly proportional to the average photoelectron rate. From this, a representation of the single-sided power spectrum of shot noise is derived at a narrow bandwidth Δf around the center frequency f:

$$P_{shot}(f) = 2|H_n(f)|^2 q I_{avg} R \Delta f \qquad [\mathrm{W}]$$

Equation 3-22

In this equation, I_{avg} represents the average photocurrent (which is related with the photocurrent rate when comparing Eq. 3-10 and Eq. 3-13), q is the electron charge, $H_n(f)$ is the normalized version of the photodiodes transfer function, so that: $H(f) = qH_n(f)$ and R is the termination load on which the power is measured.

The frequency representation of shot noise in relation to the spectrum of the photocurrent pulses in the photodetected signal is depicted in Figure 3-11.d. This figure illustrates how shot noise scales according to the photodiode's transfer function while maintaining a relatively flat response across all frequencies.

From Equation 3-22 it is evident that shot noise becomes dominant when the optical power incident on the photodiode is sufficiently high. This occurs because shot noise power scales proportionally with the photocurrent. Consequently, shot noise may overshadow electronic noise sources (such as thermal noise and flicker noise, as will be discussed further).

In addition to shot noise, *flicker noise*—also known as 1/f noise—plays a significant role in photodetection systems, particularly at lower frequencies. Flicker noise originates from various mechanisms within the photodiode and related electronic components, including traps in the semiconductor material that can introduce fluctuations in current [92], [93]. The manifestation of flicker noise is predominantly observed in systems operating at low frequencies, often below a few kilohertz.

Flicker noise leads to an excess noise in the frequency representation of the photocurrent, impacting the signal quality and reliability. Unlike shot noise, which increases with photocurrent, flicker noise is more constant and varies inversely with frequency. This characteristic makes flicker noise particularly consequential in applications requiring long measurement periods or where signal stability is desired.

The expression for the spectral density of flicker noise can be represented as:

$$S_{flicker} = \frac{K}{f} \qquad [\mathrm{A}^2/\mathrm{Hz}]$$

Equation 3-23

where K is a constant that depends on the specific photodetector configuration and material properties. The presence of flicker noise in photodetection may necessitate special attention during system design, especially when optimizing for low-frequency operation.

Thermal noise, also referred to as Johnson-Nyquist noise, arises from the random motion of charge carriers within the photodiode and associated resistive elements at non-zero temperatures. This noise is inherent in all resistive electrical components and can be described by its power spectral density, which is proportional to the temperature (in Kelvin) and the resistance R:

$$S_{thermal}(f) = \frac{4k_BT}{R} \qquad [\mathrm{A}^2/\mathrm{Hz}]$$

Equation 3-24

where k_B is the Boltzmann constant. Thermal noise becomes significant at higher temperatures and, unlike shot noise, does not depend on the incident optical power or the photocurrent.

In the context of photodetection, thermal noise can severely impact the signal-to-noise ratio (SNR), especially when measuring weak optical signals. It is particularly prevalent in high-speed applications where the bandwidth is extended, as the thermal noise power integrates over a broader frequency range.

In general, both flicker noise and thermal noise are of crucial concern in photodetection from ultra-short pulses from mode-locked lasers concerning microwave synthesis. Flicker noise will present itself predominant at frequencies close to carrier during the noise spectrum. Meanwhile, thermal noise can degrade the SNR, especially in high-speed applications where the bandwidth is expanded to capture the ultrashort pulse profiles effectively. Given the sensitivity of microwave synthesis to these noise sources, effective noise management strategies such as optimizing the photodiode operating conditions, employing low-noise amplification techniques, and maintaining thermal stabilization of the detection system are essential [34]. Figure 3-13 depicts the contributions of the noise sources during photodetection into the phase noise of a microwave signal synthesized from an optical pulse train from a mode-locked laser.

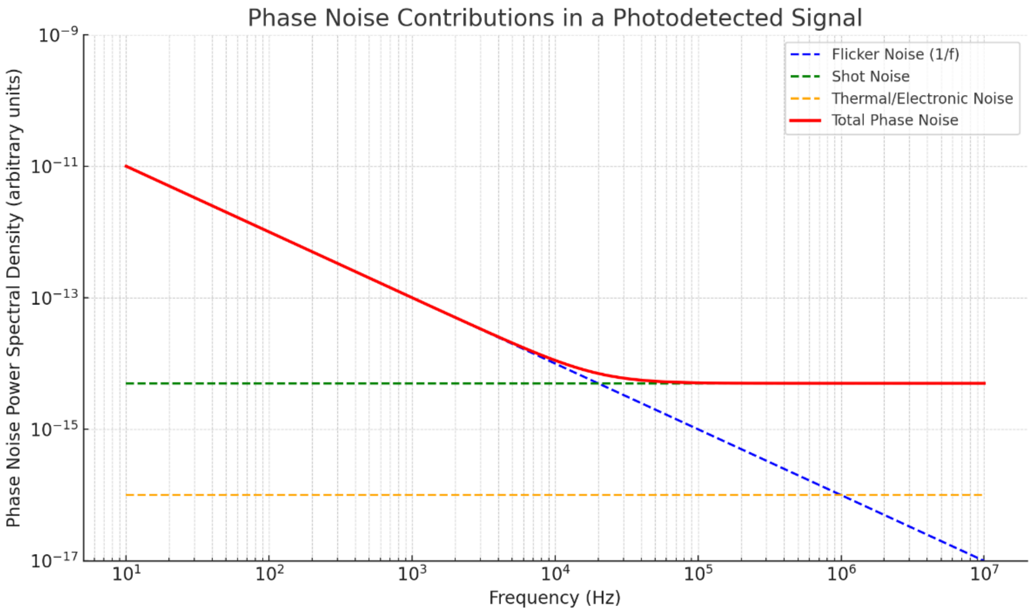

Figure 3-13. Phase noise contributions from different noise sources on a single frequency from a photodetected signal.

3.2.4. AM-PM Conversion

In addition to the aforementioned noise sources and the inherent timing characteristics of noise in photodetection, another phenomenon to consider is amplitude modulation to phase noise modulation, or AM to PM conversion for short. This refers to the phenomenon where amplitude modulation of the incoming optical pulse signal (related to the relative intensity noise of the laser) results in excess phase modulation noise of the photocurrent signal of similar amplitude.

This phenomenon arises due to nonlinearities in the photodiode, circuit parasitics, and thermal effects, and has significant implications for the performance of systems that generate microwave or RF signals from optical sources, particularly mode-locked lasers [94]. The nonlinear response of photodiodes, temperature-dependent variations, and impedance mismatch are the main contributors to this effect [95]. These factors distort the optical-to-electrical conversion process, introducing unwanted phase noise and reducing the stability of the generated signal.

In mode-locked laser systems, ultrashort optical pulses with high peak power drive larger values of AM-to-PM conversion, since it is directly dependent on the input power. This becomes more apparent when the photodiode is operating near saturation or outside its linear range. This conversion adds phase noise to the electrical signal, degrading spectral purity and creating spurious sidebands that degrade signal quality. The amount of AM-to-PM conversion depends on factors such as optical power, modulation frequency, pulse repetition rate, and the type of photodiode used. For example, high linearity photodiodes such as MUTC devices typically exhibit reduced AM-to-PM effects compared to standard PIN photodiodes [96], which will be further discussed.

As shown in [75], photodiodes (even devices with the same construction and characteristics) describe a unique AM-PM conversion characteristic (or coefficient). This is another major limitation of direct photodetection for systems where sub-femtosecond precision of the generated microwave is required, since a fixed value for the AM-PM contribution of the photodiode cannot be well established without prior characterization, which can be a tedious task.

Careful system design is essential to mitigate the AM-to-PM conversion. Strategies include using highly linear photodiodes, ensuring that the photodiode operates within its linear range, stabilizing the temperature of the photodetector, and designing impedance-matched, low-noise circuits. In addition, preconditioning optical pulses to minimize distortion and peak power helps limit nonlinear effects during photodetection [97], [98]. By addressing these factors, AM-to-PM conversion can be minimized, resulting in improved signal fidelity and lower phase noise in systems that rely on photodetected optical pulses.

3.2.5. Photodiode Types

Photodiodes used for detecting ultrashort optical pulses and converting them into microwave signals must balance key performance metrics, including high responsivity, saturation power, linearity, and wide bandwidth. Various photodiode architectures have been developed to optimize these characteristics, with the most widely used types being PIN, dual-depletion region (DDR), uni-traveling carrier (UTC), and modified UTC (MUTC) photodiodes [88], [98-100]. Additionally, waveguide-integrated designs based on these configurations further enhance performance [102].

Among these, PIN, DDR, and MUTC photodiodes have demonstrated the lowest noise and highest stability in optically generated microwave signals, making them the focus of this discussion. Their performance is primarily governed by carrier transit time and the RC time constant (given by the resistance and capacitance across the circuit), which depend on the depletion region’s thickness and device capacitance. Optimizing photodiode design involves increasing the depletion region for better light absorption while reducing capacitance to minimize RC limitations. Figure 3-14 illustrates the energy band diagrams and structural characteristics of these photodiodes.

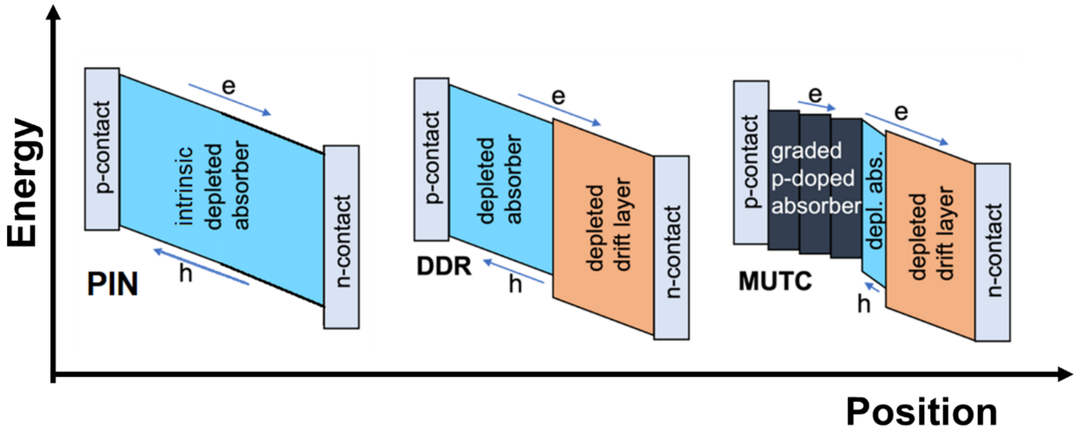

Figure 3-14. Band diagrams of PIN, DDR and MUTC photodiodes.

Modified from [34], [89].

3.2.5.1. PIN Photodiode Structure

The PIN photodiode features p-doped and n-doped semiconductor layers separated by an intrinsic (undoped) layer, which serves as the depletion region where most photoelectric conversion occurs. The intrinsic layer supports an extended electric field, effectively widening the depletion region. A wider depletion region increases the area available for light absorption and reduces junction capacitance, thereby lowering the RC time constant and enhancing the bandwidth. However, increasing the depletion width also lengthens the transit time of carriers, which may limit the bandwidth if not carefully managed. By minimizing the ratio of carrier diffusion to drift lengths, a larger portion of the photocurrent is transported via the faster drift process, improving the photodiode's response.

3.2.5.2. Dual-Depletion Region (DDR) Photodiodes

The DDR photodiode is an extension of the PIN design, incorporating both absorbing and non-absorbing depletion layers. Upon optical illumination, photogenerated electrons and holes in the absorbing layer are swept toward the p-doped and n-doped regions under the influence of an applied bias voltage. Positioning the absorber layer near the p-contact ensures that the slower holes only traverse the absorber, while the faster electrons transit through both the absorbing and non-absorbing drift layers. This design balances the transit times of electrons and holes. The device's capacitance, which can be modeled as a parallel-plate capacitor, is reduced by the addition of the non-absorbing drift layer without compromising transit-time-limited bandwidth. Consequently, DDR photodiodes achieve higher bandwidth and narrower impulse responses. Furthermore, the inclusion of the drift layer increases the saturation power, as it allows for larger device diameters without significantly increasing capacitance [99].

3.2.5.3. Modified Uni-Traveling Carrier (MUTC) Photodiodes

MUTC photodiodes further refine the dual-layer concept by incorporating a p-doped, undepleted absorbing layer. This design minimizes the contribution of hole transport, leaving the faster, high-mobility electron transport as the dominant mechanism for the photodetector's response. To address saturation effects, MUTC photodiodes utilize a multilayer structure to carefully shape the internal electric field. The tailored electric field assists in carrier transport, mitigating space-charge effects and allowing the device to maintain high bandwidth even under high photocurrent conditions. This design not only enhances bandwidth but also ensures reliable operation at higher optical power levels [103].

3.2.6. Photodiodes under Test

The performance of PIN and MUTC photodiodes in detecting ultrashort optical pulses and converting them into microwave signals was evaluated for their suitability in the microwave synthesis process for the PMO setup. Two experiments were conducted to compare the RF power response of the EOT 3500-F (PIN) and FP1015a (MUTC) photodiodes under different operating conditions.

The tests involved using optical pulse trains from a MENHIR-1550 mode-locked laser and provided insights into the linearity, saturation behavior, and harmonic generation characteristics of the two photodiode types. These evaluations help determine the optimal photodetector choice for achieving high-power handling in photonic microwave oscillator applications.

3.2.6.1. Fundamental and Harmonic RF Response at 1 GHz

The first experiment investigated the single harmonic RF response of both photodiodes when illuminated by a MENHIR-1550 laser operating at a 1 GHz repetition rate. The optical power varied from -6 dBm to 14 dBm for the MUTC photodiode and from -3 dBm to 12 dBm for the PIN photodiode. Two key metrics were measured: the RF power at the fundamental harmonic (1 GHz) and the RF power at the 10th harmonic (10 GHz).

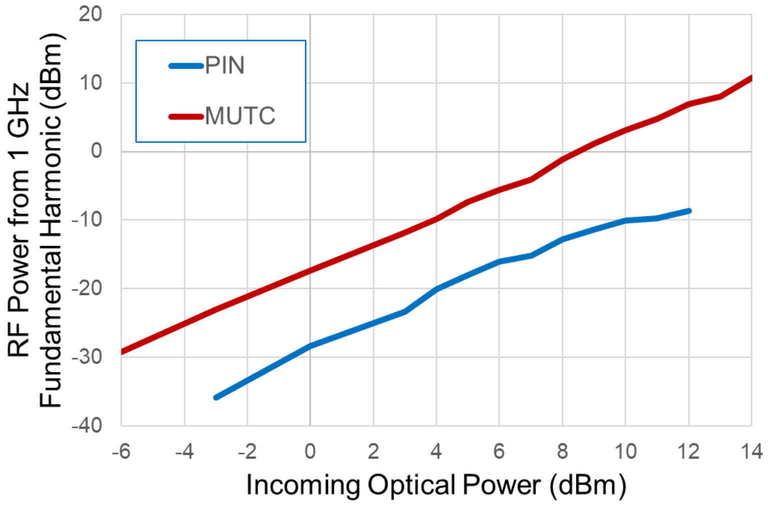

Figure 3-15. Photocurrent RF power for the fundamental harmonic frequency at 1 GHz vs. incoming average optical power for PIN and MUTC photodiodes.

Figure 3-15 shows the results for the RF power measurement of the fundamental harmonic contained in the photocurrent pulse at 1 GHz. Here, both photodiodes showed an increase in RF power proportional to the optical power, as expected. However, the MUTC photodiode consistently delivered higher output power, maintaining a minimum 10 dB advantage over the PIN photodiode across the entire power range. This highlights the superior responsivity and efficiency of the MUTC design for converting optical signals to RF power at the fundamental frequency.

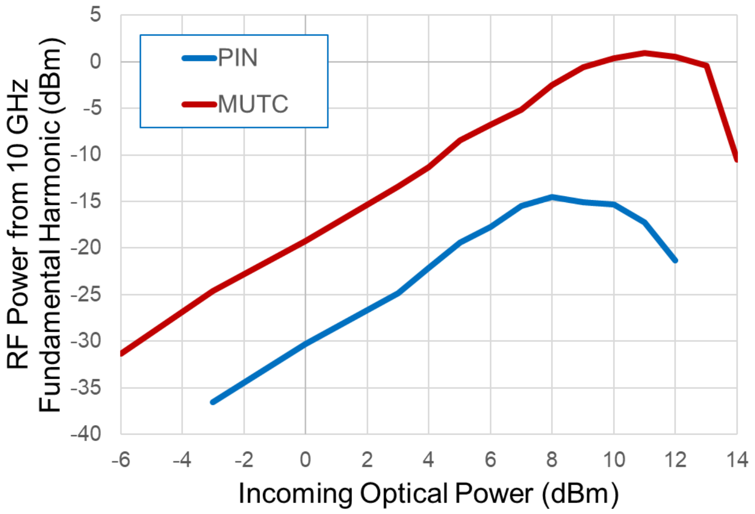

Figure 3-16. Photocurrent RF power for the 10th harmonic frequency at 10 GHz vs. incoming average optical power for PIN and MUTC photodiodes.

Figure 3-16 shows the results for the RF power measurement of the 10th harmonic at 10 GHz. Here, both photodiodes initially exhibited proportional scaling of RF power with incoming optical power. However, saturation effects began to emerge at higher optical powers. The PIN photodiode experienced saturation at around 8 dBm optical power, after which its RF power output decreased sharply. In contrast, the MUTC photodiode maintained its linearity up to approximately 12 dBm before saturation effects became evident. Even in the saturation regime, the MUTC outperformed the PIN photodiode in RF power output, demonstrating its superior saturation power and ability to sustain high-frequency performance.

In summary, the MUTC photodiode showed clear advantages over the PIN photodiode in terms of RF power at their outputs, saturation resilience, and bandwidth, making it better suited for high-power, high-frequency microwave generation applications.

3.2.6.2. Frequency Response of the MUTC Photodiode at Different Repetition Rates

A second experiment was carried out, focusing exclusively on the MUTC photodiode, examining its frequency response when illuminated by the MENHIR-1550 laser at two different repetition rates: 400 MHz and 1 GHz. The optical power varied from –6 dBm to 15 dBm in 3 dB increments, and the RF power of individual harmonics was measured across the optical spectrum. It is interesting to observe how the RF power of the harmonics scales quadratically to the optical input power, evidenced in the lower harmonics which increase by 6dB for each 3dB increase in optical power.

Figure 3-17 shows the case for the 400 MHz repetition rate mode-locked laser. Here, the electronic power spectrum was measured up to 15 GHz. It details each harmonic RF power as single points, which are joined to display the frequency response of the photodiode.

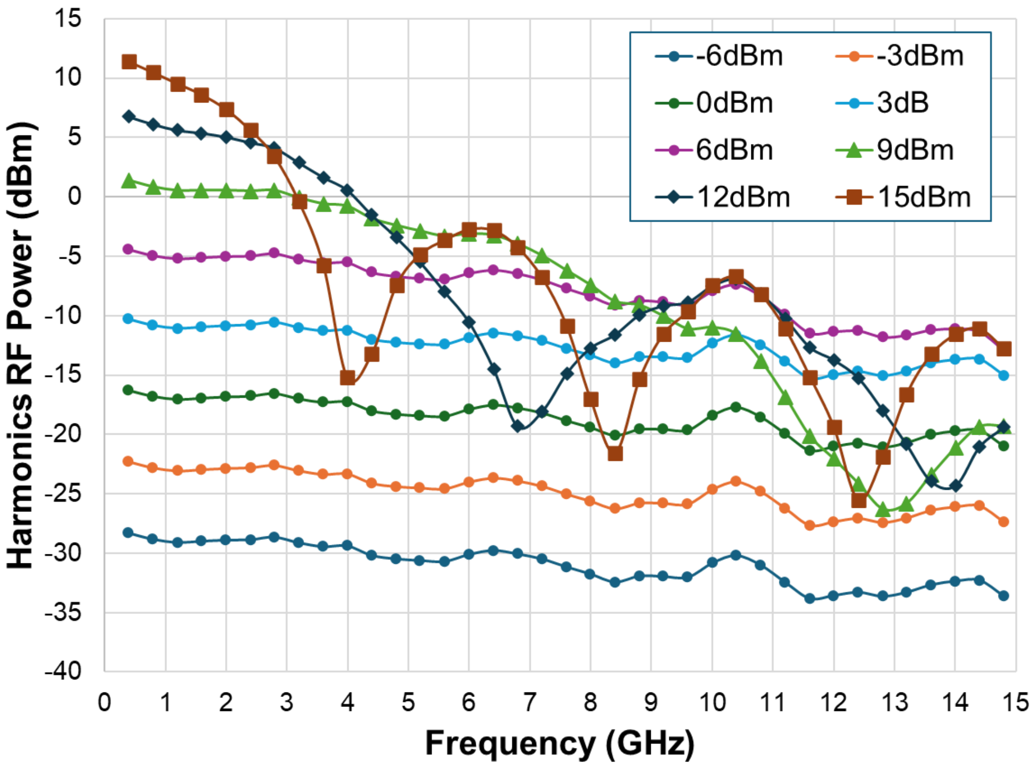

Figure 3-17. Optical spectrum of photocurrent pulse for the MUTC photodiode illuminated by a 400 MHz repetition rate mode/locked laser.

It is clear how each harmonic scaled proportionally with increasing optical power at lower levels. However, non-linearities became apparent starting from 6 dBm optical power, particularly at higher harmonics. These non-linearities are attributed to saturation effects and space-charge dynamics within the photodiode.

In contrast, Figure 3-18 illustrates this case at a 1 GHz repetition rate. Here, the photodiode displayed a more linear response, with non-linearities emerging only at higher optical powers (around 12 dBm). The higher repetition rate reduced the time between successive optical pulses, distributing the optical energy more evenly and reducing saturation effects. As a result, the MUTC photodiode maintained a more stable and linear frequency response over a broader range of optical powers.

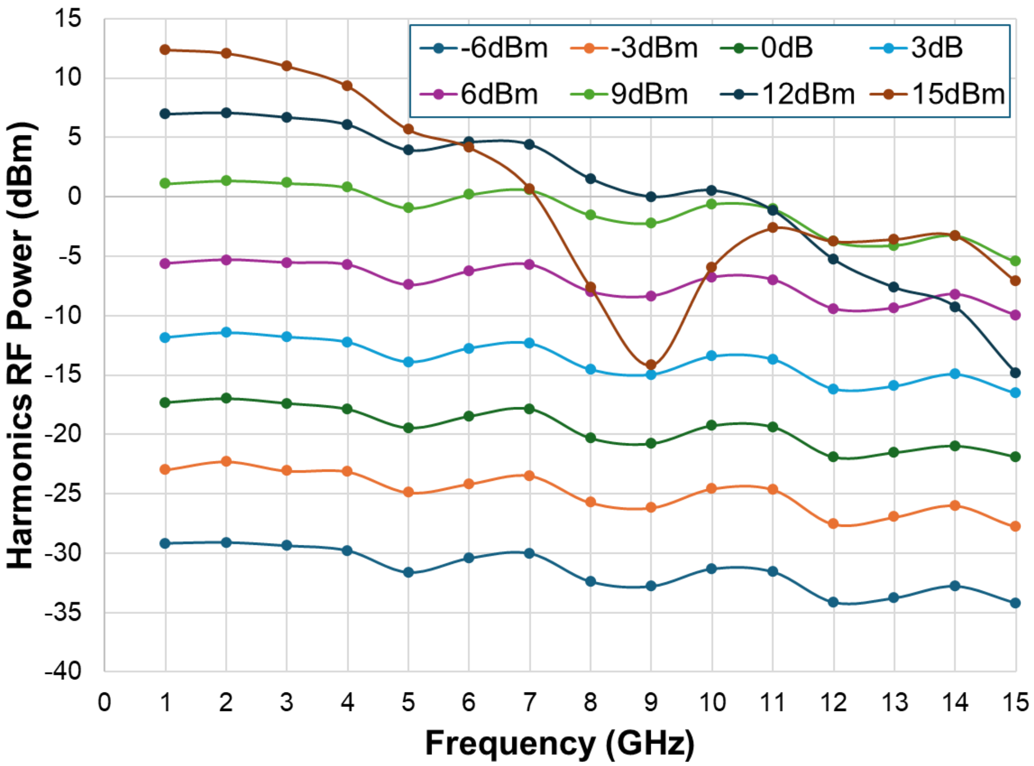

Figure 3-18. Optical spectrum of photocurrent pulse for the MUTC photodiode illuminated with a 1 GHz repetition rate mode/locked laser.

The results also demonstrated that the closer a harmonic is to the fundamental frequency, the more linear the response remains as optical power increases. This behavior underscores the benefit of high repetition rate lasers for generating high-frequency microwaves at higher RF power levels, as they mitigate non-linear effects and improve photodiode performance in high-power regimes. Additionally, interleaving techniques can be employed as a complementary solution to further enhance high-frequency microwave generation [104], [105]. By interleaving multiple synchronized optical pulse trains, the effective repetition rate can be increased, thereby reducing the energy per pulse and spreading the optical power more evenly across the frequency spectrum. This reduces the likelihood of non-linear effects, such as saturation and space-charge buildup, and enhances the overall linearity and efficiency of the photodiode at higher harmonic frequencies.

These characterization experiments emphasize the superior performance of MUTC photodiodes over PIN photodiodes for high-speed photodetection and microwave generation. The MUTC photodiode not only provided higher RF output power at both fundamental and harmonic frequencies but also exhibited greater resilience to saturation, maintaining linearity over a wider range of optical powers.

Additionally, increasing the repetition rate of the optical pulse train proved advantageous for generating high-frequency microwaves. At higher repetition rates, the MUTC photodiode demonstrated improved linearity and reduced non-linear effects, particularly for harmonics closer to the fundamental frequency. These findings highlight the MUTC photodiode’s suitability for its use in the microwave synthesis at a photonic microwave oscillator setup.

4. PHOTONICALLY REFERENCED EXTREMELY STABLE OSCILLATOR (PRESTO)

As discussed across this dissertation, mode-locked lasers have become fundamental tools for ultra-low phase noise microwave generation, surpassing traditional electronic oscillators in timing precision and frequency stability. However, despite their remarkable performance, these lasers are still subject to repetition rate fluctuations due to intrinsic noise mechanisms, which can degrade the stability of the generated microwave signals (See Appendix B.1 for insight). To fully harness the potential of mode-locked lasers for microwave synthesis, effective stabilization techniques are required to mitigate these fluctuations and ensure that the microwave signal inherits the exceptional phase noise and timing stability from the optical source.

Several stabilization strategies have been explored in the literature, as detailed in Section 1.3, including locking mode-locked lasers to ultra-stable optical references such as high-finesse optical cavities, atomic clocks, or stabilized CW lasers [39], [40], [106]. While highly effective, these methods often involve complex, costly, and bulky setups, limiting their practicality for compact and scalable implementations. An alternative approach focuses on self-referencing stabilization, where the laser is locked to an internal optical reference, such as a fiber delay-line, providing a streamlined and cost-efficient means of achieving enhanced stability [107], [108].

This chapter presents the design and implementation of the Photonically Referenced Extremely Stable Oscillator (PRESTO), a novel photonic microwave oscillator architecture that leverages self-referencing stabilization to achieve outstanding phase noise performance. The discussion begins with a theoretical framework that outlines the stabilization process, feedback loop dynamics, and noise reduction mechanisms employed in PRESTO. A computational model is then introduced to simulate system performance and validate the stabilization concept.

Following the theoretical and simulation studies, the chapter provides a detailed description of the experimental setup, emphasizing the key optical and microwave components, their roles, and the overall system configuration. The performance of PRESTO is evaluated through in-loop timing jitter measurements and microwave phase noise characterization, offering a comprehensive analysis of its stability under different operating conditions.

4.1. PRESTO: CONCEPT AND DESIGN

The fundamental configuration of PRESTO is illustrated in Figure 4-1, with the primary objective of stabilizing the repetition rate of a mode-locked laser by employing a fiber delay-line as a key reference. The stabilized optical source is then used to generate a highly stable microwave signal, ensuring that the frequency stability in the optical domain is transferred to the microwave domain [109].

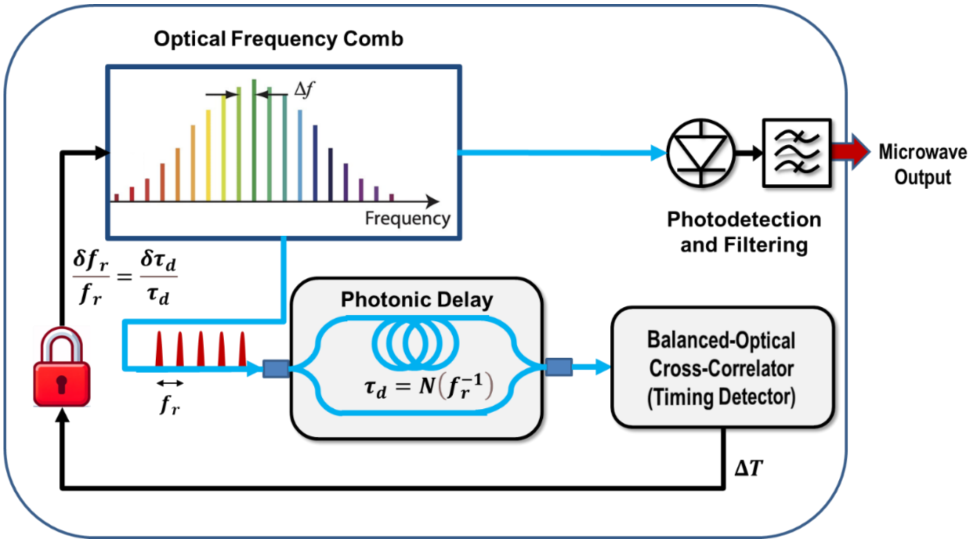

Figure 4-1: General configuration for the Photonically Referenced Extremely Stable Oscillator (PRESTO).

In this system, the fiber delay-line serves as a passive optical reference, where the optical pulse train circulates, with the introduced delay corresponding to the number of pulses accommodated based on the laser's repetition rate. This delay acts as an energy storage element, reinforcing the coherence and stability of the pulse train.

The stabilization process involves comparing the timing difference between the directly emitted pulse train from the laser and the pulse train delayed through the fiber delay-line. This comparison is performed using a BOC, which measures the relative timing difference and generates an error signal that reflects the deviation. The resulting error signal is processed in a PLL control system that actively regulates the laser's repetition rate, effectively suppressing unwanted timing fluctuations.

By locking the mode-locked laser's repetition rate to the fractional stability of the fiber delay-line, PRESTO achieves an enhanced level of frequency stability, which is then directly translated into the synthesized microwave signal.

4.1.1. Feedback Loop Model

In order to comprehend the fundamental dynamics of timing jitter and phase noise in this oscillator, we describe the timing jitter dynamics of the mode-locked laser by means of a simple diffusion equation, which is driven by the fundamental spontaneous emission noise of the amplifier, as described in [110].

$$\frac{d}{dt}\Delta T = S_T(t)$$

Equation 4-1

where $S_T(t)$ is the spontaneous emission noise characterized as white noise with a certain power spectral density D_T

$$\langle S_T(t)S_T(t')\rangle = D_T\,\delta(t-t') \text{ with } D_T = \frac{\pi^2\tau^2}{3}\frac{P_n}{W_0} \text{ and } P_n = \Theta\frac{2g_s}{T_R}\hbar\omega_0\,,$$

Equation 4-2

Here, P_n is the spontaneous emission noise power of the optical amplifier, W_0 the intracavity pulse energy, Θ the excess noise factor of the optical amplifier, $2g_s$ the round-trip power gain of the laser cavity, T_R the cavity round-trip time and $\hbar\omega_0$ the photon energy at the center wavelength of the gain medium. The time or center position of the pulse, ΔT, undergoes a random walk driven by white noise, that is integrated over time by the laser cavity from round-trip to round-trip. This is described by the flow diagram depicting the free-running mode-locked laser with noise shown in Figure 4-2.

For the rest of the analysis, the intrinsic timing jitter spectrum of the laser is defined as:

$$J_I^2 = \Delta\hat{T} = \frac{D_T}{\omega^2} \qquad [\ \mathrm{fs}^2/\mathrm{Hz}]$$

Equation 4-3

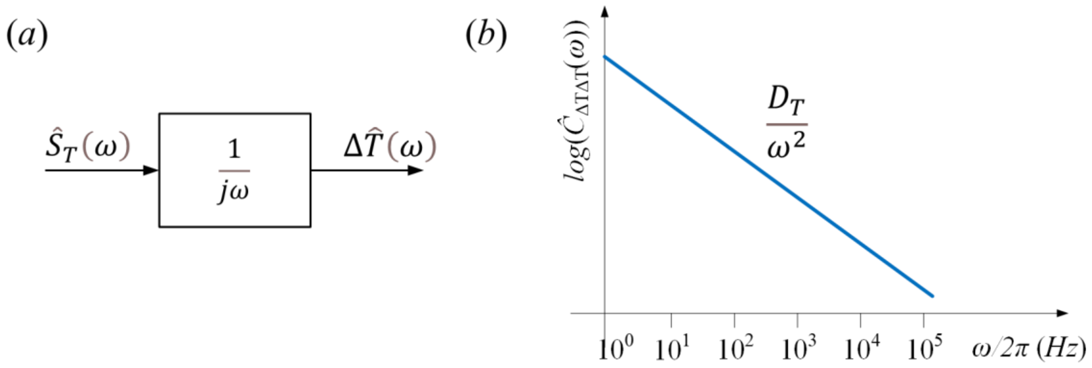

Figure 4-2. Integration of spontaneous emission noise over each round-trip in a mode-locked laser.
(a) Free running laser depiction; (b) Corresponding correlation spectrum of timing fluctuations

Parting for the intrinsic integrated timing jitter of the laser, a feedback loop analysis is performed to study the different dynamics affecting the PRESTO setup. Here, we study our delay-based feedback loop using a model similar to that in [83] (see Figure 4-3).

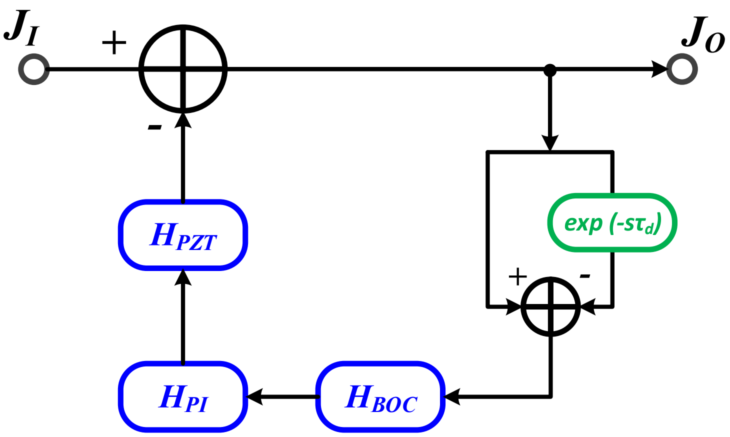

Figure 4-3. Feedback loop model for PRESTO.
J_I: intrinsic laser jitter, J_O: Jitter when feedback loop is active; H_{BOC}, H_{PI}, H_{PZT}, transfer functions of the BOC, PI controller and laser's PZT, respectively.

The intrinsic timing jitter of the laser, J_I, is split into two paths: one undergoes a long fiber delay, τ_d, while the other is much shorter (i.e., << τ_d). The timing jitter between these two paths is measured by a BOC and transformed into a voltage signal through the BOC transfer function, $\boldsymbol{H}_{BOC}$. This voltage signal is then fed into a PI controller, $\boldsymbol{H}_{PI}$, configured in a negative feedback loop. The output from the PI controller is amplified and converted into a round-trip cavity delay by the PZT, $\boldsymbol{H}_{PZT}$, which reduces the laser's timing jitter by making precise mechanical adjustments to the cavity. According to this model, the relationship between the inherent laser jitter, J_I, and the laser output jitter when feedback is active, J_O, is expressed as:

$$\boldsymbol{J}_O = \left[\frac{1}{1 + \boldsymbol{H}_{BOC}\boldsymbol{H}_{PI}\boldsymbol{H}_{PZT}(1 - e^{-s\tau_d})}\right]\boldsymbol{J}_I$$

Equation 4-4

The transfer functions of the feedback elements are:

$$\boldsymbol{H}_{BOC} = \frac{K_{BOC}}{s + 2\pi f_{BPD}} \quad \boldsymbol{H}_{PI} = \frac{K_{PI}}{s + 2\pi f_{PI}} \qquad \boldsymbol{H}_{PZT} = \frac{K_{PZT}}{f_R s}\left(\frac{2\pi f_{res}}{s^2 + \xi s + (2\pi f_{res})^2}\right)$$

Equation 4-5

Here, $s = j\omega$ is the complex frequency. K_{BOC} determines the timing sensitivity of the BOC, whereas f_{BPD} represents the bandwidth of the balanced photodetector that constitutes part of the BOC. Additionally, K_{PI} and f_{PI} represent, respectively, the proportional gain and integral corner frequency of the PI controller. Moreover, K_{PZT} represents the piezo electrical sensitivity, whereby the electrical signal from the driver is transduced into a change of length in the cavity, which in turn results in a change in f_R, representing the repetition rate of the laser. In consequence, $\boldsymbol{H}_{PZT}$ describes the transfer function for the cumulative effect of the PZT and the cavity indicating that the delay generated by the PZT is integrated by the cavity. The term on the left for $\boldsymbol{H}_{PZT}$ represents the effect of the resonance frequency of the piezoelectric actuator, which can also represent a significant limitation, as will be discussed subsequently.

Then, the average jitter spectral density at the laser output can be expressed as:

$$\overline{\boldsymbol{J}_O^2} = |\boldsymbol{H}_\tau|^2\, \overline{\boldsymbol{J}_I^2}$$

Equation 4-6

Here the term $\boldsymbol{H_\tau}$ expresses the transfer coefficient, defined as:

$$|\boldsymbol{H_\tau}|^2 = \left[\frac{1}{1 + \boldsymbol{H}_{BOC}\boldsymbol{H}_{PI}\boldsymbol{H}_{PZT}(1 - e^{-s\tau_d})}\right]^2$$

Equation 4-7

In the frequency range where $\tau_d \ll 1$ and $|\boldsymbol{H}_{BOC}\boldsymbol{H}_{PI}\boldsymbol{H}_{PZT}(1 - e^{-s\tau_d})| \gg 1$; and by reducing the transfer functions for each component into a fully proportional system without any zeros and poles, this transfer function can be simplified to:

$$|\boldsymbol{H_\tau}|^2 = \left[\frac{1}{K_{BOC}K_{PI}K_{PZT}\tau_d}\right]^2$$

Equation 4-8

This simplification assumes that the system can be approximated by a proportional gain, effectively neglecting the higher-order dynamics introduced by zeros and poles in the individual transfer functions.

The resulting timing jitter of the oscillator coming from this approximation makes it behave as a new free-running oscillator with a new rescaled driving power spectral density equal to:

$$\overline{\boldsymbol{J_O^2}} = \left[\frac{1}{K_{BOC}K_{PI}K_{PZT}\tau_d}\right]^2 \overline{\boldsymbol{J_I^2}}$$

Equation 4-9

Intuitively, one can see that a higher reduction in timing jitter can be achieved by increasing the delay in the fiber delay-line, which corresponds to increasing the fiber length. Additionally, having a higher sensitivity in the BOC and greater available gain from the control system in the feedback loop will further enhance jitter reduction.

This scenario represents the ideal case. In practice, the output of the BOC will have a noise floor, and the delay line will experience length fluctuations, $\Delta\widehat{\tau_d}$, due to various factors, including thermorefractive noise, creating refractive index fluctuations in the delay-line caused by thermal and mechanical variations, alongside acoustic effects picked up by the fiber-delay line. Figure 4-4 shows how this noise of the fiber delay-line is propagated and imprinted into the timing jitter of the mode-locked laser.

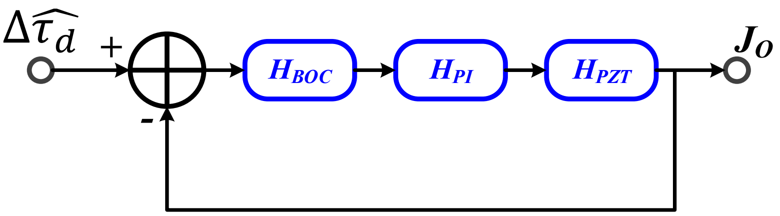

Figure 4-4. Timing noise written into the timing jitter of the mode-locked laser.

This delay line timing noise is written via the feedback loop into the timing of the laser according to the noise transfer function:

$$\widehat{\boldsymbol{H}}_{\tau_d} = \frac{K_{BOC}K_{PI}K_{PZT}}{1 - K_{BOC}K_{PI}K_{PZT}}$$

Equation 4-10

The timing jitter of the delay line should be much lower than the timing jitter of the free running laser so that the condition $|K_{BOC}K_{PI}K_{PZT}| \gg 1$ holds, resulting in a timing jitter transfer to the laser from that of the fiber delay-line. The stability of the fiber-delay line will be discussed in the next section.

Once the mode-locked laser is locked to the fiber-delay line and follows its timing jitter, the microwave signals synthesized from the laser, as described in Section 3.2.2, will also follow the timing jitter fluctuations and drift. The corresponding fluctuation spectra for the microwave signals will scale as:

$$S_{\mu}(\omega) = S_{opt}(\omega)\left(\frac{\omega_{\mu}}{\omega_{opt}}\right)^2$$

Equation 4-11

Here, $S_{\mu}(\omega)$ is the power spectral density of the timing jitter in the synthesized microwave signals, $S_{opt}(\omega)$ is the power spectral density of the timing jitter in the optical domain, ω_{μ} is the frequency of the microwave signal, and ω_{opt} is the repetition rate of the optical pulse train. This relationship indicates that the timing jitter characteristics of the microwave signals will be influenced by those of the mode-locked laser, scaled by the ratio of the microwave frequency to the optical repetition rate squared.

4.1.1.1. Noise suppression analysis

Having established a feedback model for the noise reduction achievable with PRESTO, a computer simulation based on Equation 4-7 is performed, to determine the effects of the feedback loop gain on the achievable noise reduction. For this simulation, $\boldsymbol{H_{BOC}}$ is chosen to be fully proportional, effectively omitting the effects of the balanced photodetector's bandwidth, since the bandwidth of the photodetector is much broader than the locking bandwidth of the system. This simplification allows us to focus on the primary effects of the feedback loop gain without additional complexities.

Table 4-1 lists the parameters used for this analysis, including the fiber delay length, PI controller settings, and PZT characteristics.

Table 4-1. PRESTO feedback loop model parameters for loop gain effects.

Parameter	Symbol	Value	Units
BOC Timing Sensitivity	K_{BOC}	$2\cdot10^{12}$ $(2\cdot10^{10})$	V/s
Laser's Repetition Rate	f_R	1.0	GHz
PI Proportional Gain	K_{PI}	*Varies*	dB
PI Corner Frequency	f_{PI}	30	kHz
PZT Voltage Response	K_{PZT}	146.7	Hz/V
PZT Resonance Frequency	f_{res}	40	kHz
PZT Damping Parameter	ξ	$1\cdot10^{3}$	-
Fiber Delay Length	$L_{\tau d}$	2.084	km

By systematically varying the feedback loop gain, it is possible to observe the resulting noise reduction that is expected from the PRESTO system in an ideal scenario. Figure 4-5.a illustrates the outcomes of this simulation, following the parameters outlined in Table 4-1. It is evident that as gain increases, the expected noise reduction also increases. Furthermore, the available locking bandwidth of the overall system is extended, resulting in noise reductions of up to tens of kilohertz.

However, a negative peak appears around the resonance frequency of the piezoelectric transducer (40 kHz), which scales with increasing gain. In practice, this resonance frequency imposes a fundamental limitation of PRESTO, as it represents a 180° phase shift, creating a peak resonance in the phase noise spectrum. This resonance increases the overall timing jitter from this corner frequency onward with increasing gain. Therefore, careful selection of the overall gain of the system is necessary to avoid high peak resonances and spurious components in the phase noise spectrum.

Additionally, upon removing the resonance response of the piezoelectric element from $\boldsymbol{H}_{PZT}$ in Equation 4-5, we obtain the transfer function response observed in Figure 4-5.b. This provides insight into the further limitations if a broader band actuator were used in place of the piezoelectric actuator in the laser's cavity. In this scenario, phase shifts start appearing around the resonance frequency of the fiber-delay line itself, approximately 97.98 kHz, and its corresponding harmonics. If there were no further constraints from the actuator, the fiber delay line's inherent resonance would become the next limitation. This will be discussed in more detail in the next section.

A third comparison was conducted with the same parameters as the previous one but with reduced timing sensitivity from the BOC, approximately two orders of magnitude smaller, which corresponds to the sensitivity available in the bulk version of the BOC. Figure 4-5.c shows this case, where the achievable noise reduction is significantly lower compared to the waveguide BOC. Furthermore, the achievable locking bandwidth is constrained, beginning at a few hundred hertz and reaching tens of kilohertz due to the imposed gain limit. This limitation may prove detrimental, as it could be dominated by the electronic noise of the overall feedback loop electronics.

These simulations provide valuable insights into the behavior of the PRESTO system under different operating conditions, highlighting the critical factors that influence noise reduction performance. Understanding these dynamics enables the fine-tuning of the system for maximum achievable stability and precision, particularly for further microwave synthesis.

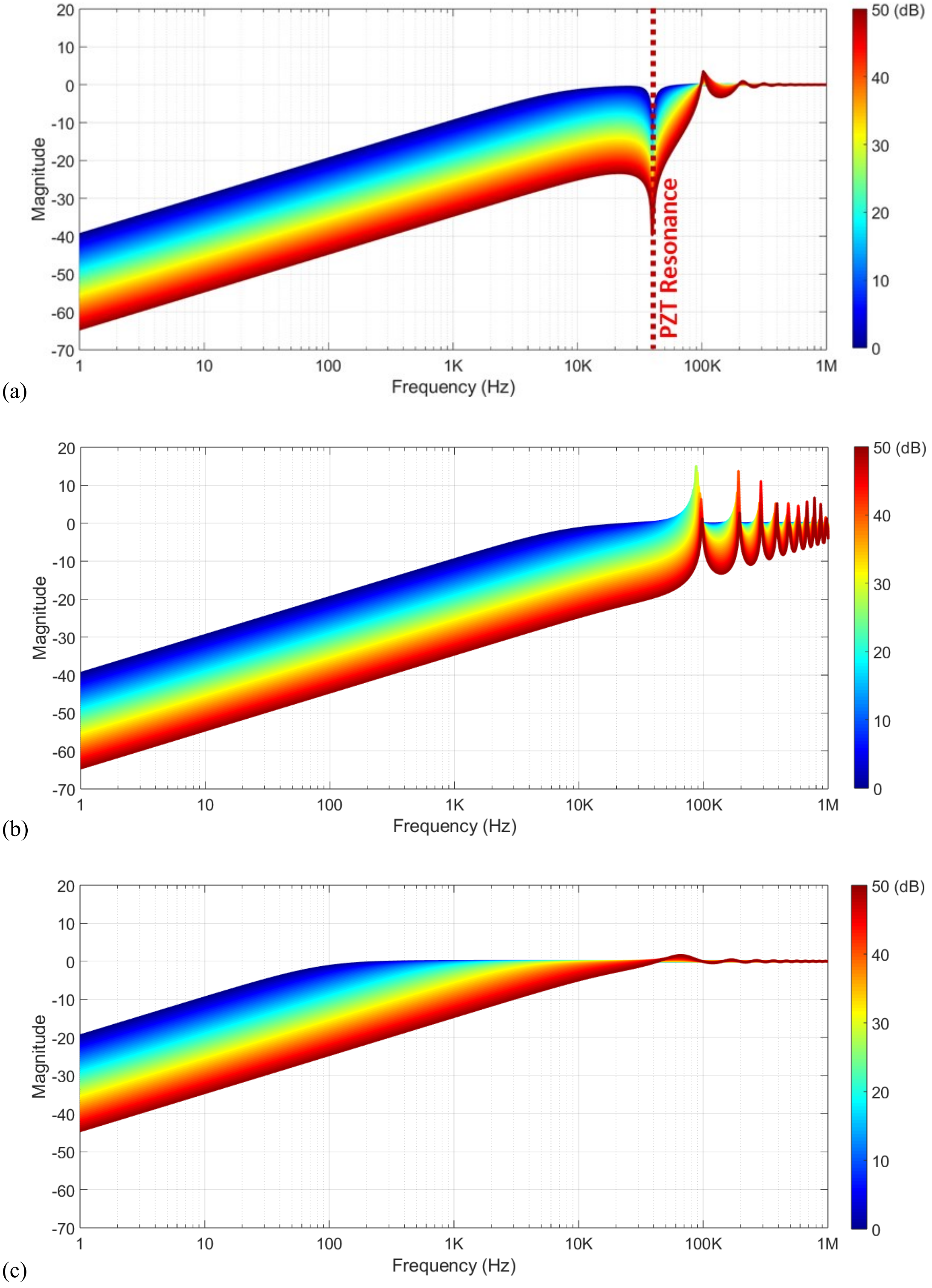

Figure 4-5. Feedback loop model from PRESTO with increasing proportional gain of the PI loop controller.

(a) Including the effects of the main resonance frequency of the PZT actuator in the laser, (b) Omitting the PZT effect to observe the following resonance of the cavity, (c) Omitting the PZT effect and reducing the timing sensitivity of the BOC to that of a bulk BOC.

4.1.2. Fiber Delay-Line Reference

As discussed in the previous section; to enhance the timing stability of the repetition rate of the mode-locked laser, the fiber-delay line must exhibit superior overall timing stability. This stability is crucial because it directly influences the stability of the laser cavity. The timing stability of the delay line is determined by the stability of its length, which in turn dictates the stability of the time delay introduced by this cavity. In essence, the more stable the length of the fiber-delay line, the more effectively this stability can be transferred to the mode-locked laser, thereby improving the precision of its repetition rate:

$$\frac{\delta L_c}{L_c} = \frac{\delta \tau_d}{\tau_d} \rightarrow \frac{\delta f_R}{f_R}$$

Equation 4-12

Where L_c represents the length of the fiber delay-line and τ_d and f_R represents the introduced time delay and repetition rate of the laser, respectively.

This imposes stringent requirements on the resilience of the fiber delay-line, particularly in resisting temperature and mechanical fluctuations, making it challenging to select an appropriate delay line component. To meet these demands in the implementation of PRESTO, the chosen photonic delay line consists of a long optical fiber wound into a fiber optic gyroscope (FOG) coil element [111]. These FOG coils are specifically designed to be insensitive to mechanical noise, temperature variations, acoustic disturbances, and airflow. A detailed study of their resilience against such fluctuations is available in [112], [113], [114]. Additionally, these coils are compact, with diameters of just a few centimeters, making them ideal for applications where space constraints are a concern.

To mitigate the effects of temperature fluctuations on fiber length, the fiber is wound in a quadrupole pattern, which compensates for thermal expansion and strain, as well as the resulting index changes caused by temperature variations [115]. Figure 4-6.a illustrates this quadrupole winding pattern. The selected fiber element is a glass coil, and the fiber used is single mode, wound with UV resin. Figure 4-6.b shows the actual element used in this work.

This careful design and choice of materials ensure that the fiber-delay line can maintain the required stability, making it a critical component in achieving the high timing stability necessary for PRESTO's operation.

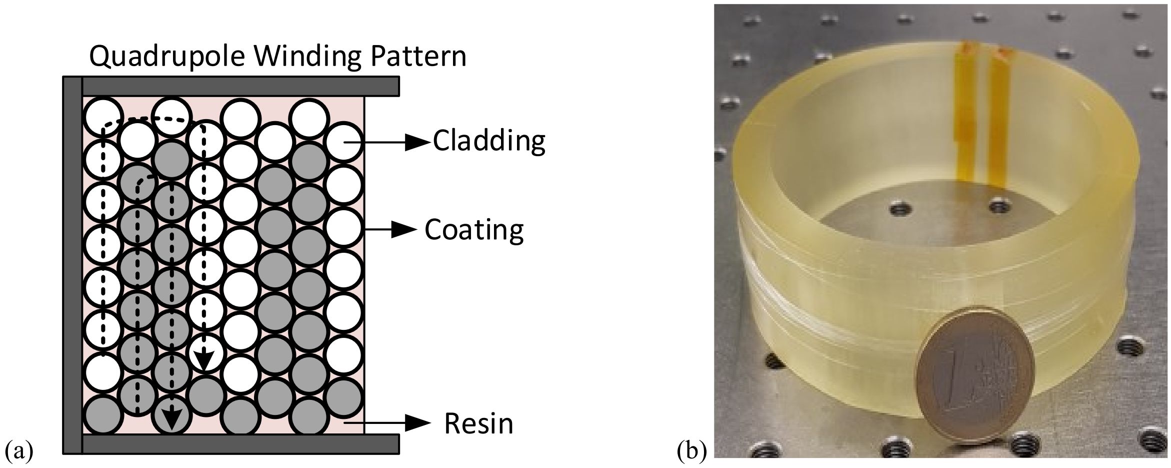

Figure 4-6. Fiber optic gyroscope coil element used as fiber-delay line for PRESTO.

(a) Quadrupole winding pattern, adapted from [116], (b) FOG coil used in the experimental setup.

4.1.2.1. Fiber Delay Length Effects on Noise Reduction

Building on the feedback model from Section 4.1.1, it was essential to evaluate the impact of the fiber-delay line length on the overall noise reduction achievable with the PRESTO setup. To do this, an additional simulation is conducted for the transfer function for noise reduction described in Equation 4-7, and using the same parameters listed in Table 4-1. PRESTO feedback loop model parameters for loop gain effects. However, this time, the gain of the PI controller is fixed at 10 dB, and the varying parameter is the fiber-delay line's length, from 0 to 4 km. This approach allows us to observe how changes in fiber length influence noise reduction.

Initially, a simulation is performed that disregards the resonance effects of the piezoelectric element within the laser's cavity. The results, shown in Figure 4-7.a, indicate that even a minimal fiber delay-line length can effectively reduce low-frequency noise components in the laser cavity. As the fiber length increases, the noise reduction improves and the bandwidth over which noise reduction is achieved also broadens. However, beyond a certain fiber length, the benefits of increased length converge, since the resonance frequency dictated by the fiber delay-line becomes narrower. This results in sharper resonance peaks at lower offset frequencies, which can cancel some of the noise reduction benefits. Therefore, an optimal fiber length must be carefully chosen to balance effective noise reduction with a broader spectral range, ensuring that the fiber delay-line's resonance does not become problematic.

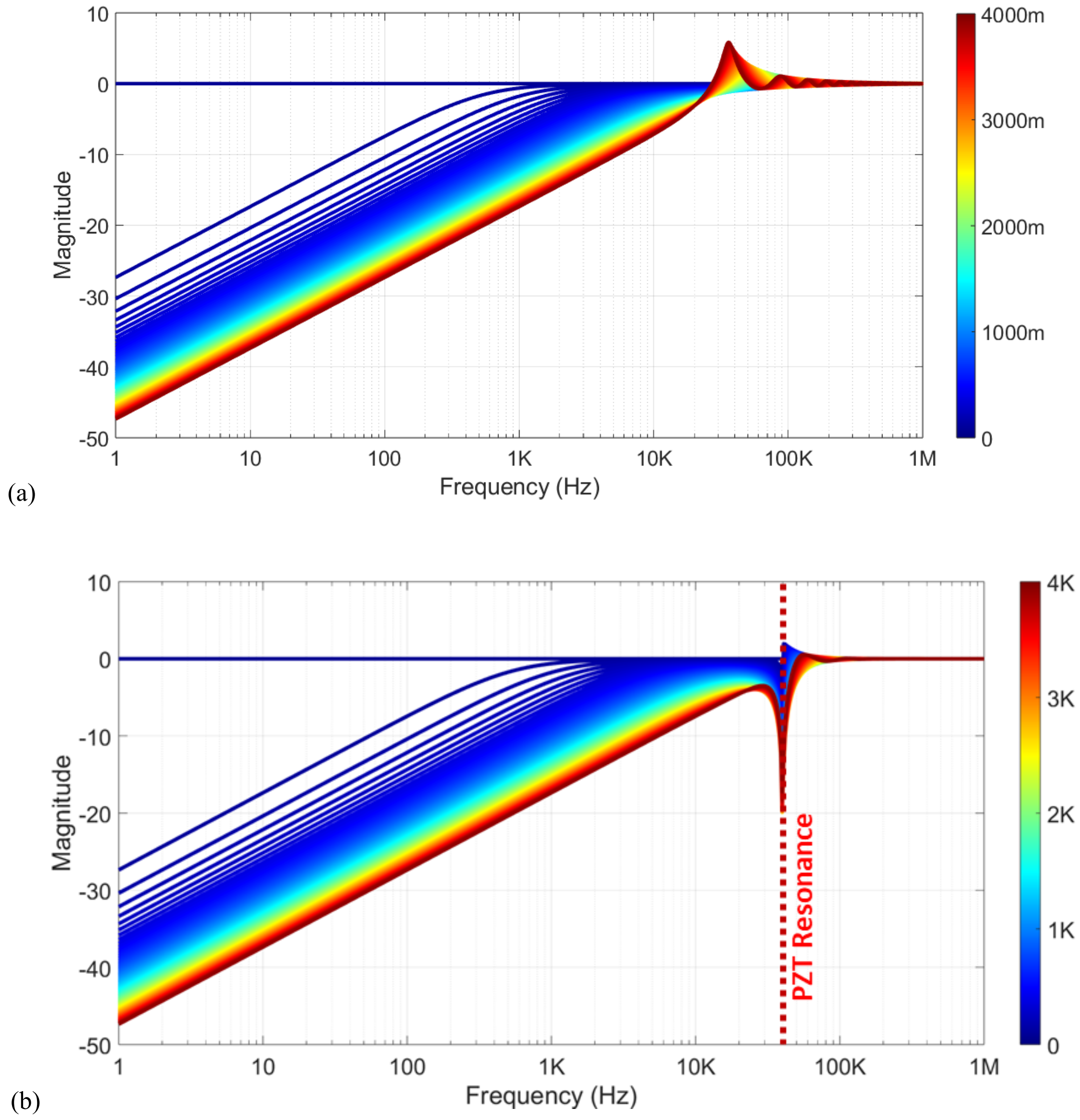

Figure 4-7. Feedback model simulation for PRESTO for increasing fiber-delay length.

(a) Ignoring the effects of the PZT resonance, (b) Including the PZT resonance into the model.

When considering the resonance effects of the piezoelectric element in the feedback loop, as shown in Figure 4-7.b, it becomes evident that, with increasing fiber length, the resonances of the piezoelectric element dominate over those of the fiber delay-line. This dominance limits the bandwidth within which noise reduction can be effectively implemented. To address this limitation, additional control strategies or the use of broader bandwidth actuators may be necessary to circumvent the constraints imposed by the piezoelectric element's resonances.

4.1.2.2. Fiber Dispersion Effects on Timing Sensitivity

When short pulses of light propagate through an optical fiber link, they are susceptible to various linear and non-linear effects. A linear effect called chromatic dispersion becomes particularly significant for this application. Chromatic dispersion arises due to the wavelength dependence of the group's velocity, leading to temporal broadening of the pulses. As a result, the stored pulse train traversing the fiber-delay line can experience pulse broadening, which not only increases their pulse duration but also diminishes the overall pulse energy [117].

This phenomenon poses a challenge for the BOC, which relies on sum-frequency generation—a non-linear process—for precise timing detection. The efficiency of this process is highly contingent on the temporal overlap and energy similarity between the stored optical pulse train and the original pulse train emitted by the laser. Any significant discrepancy in pulse duration or energy can lead to imprecise timing detection and reduced non-linear interaction efficiency.

To address this issue, careful dispersion management is required. This is achieved by introducing dispersion-compensating fiber (DCF) into the system. DCF introduces chromatic dispersion with an opposite sign to that of the primary fiber link, effectively counteracting the dispersion effects experienced during pulse propagation. By meticulously selecting the appropriate length and type of DCF, the system can restore the pulse duration and energy of the stored pulses to levels comparable with the original pulse train. This compensation ensures optimal temporal overlap and enhances the efficiency of the sum-frequency generation process within the BOC, leading to an increasing and more precise timing detection and overall system performance.

With a fixed length of the optical fiber link and a known dispersion sign and value for both the fiber link and the dispersion-compensating fiber (DCF), one can calculate the exact amount of DCF required to achieve net-zero dispersion along the entire optical path. Figure 4-8 illustrates the impact of even slight discrepancies in the length of the single-mode fiber relative to the DCF. Such discrepancies can significantly affect the S-curve response of the BOC, which is critical for maintaining the system's timing sensitivity.

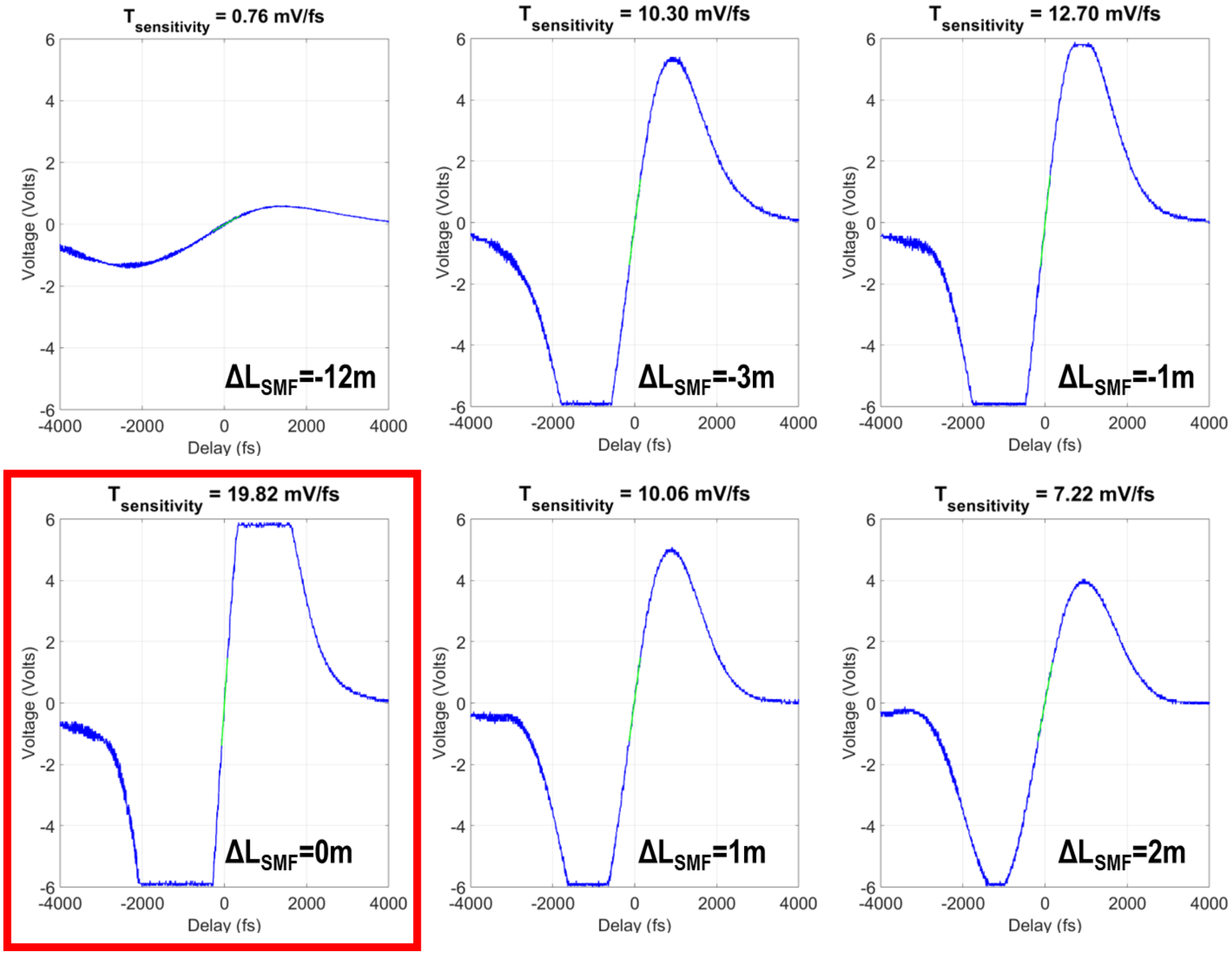

Figure 4-8: Single mode fiber length mismatch effects on the timing sensitivity due to dispersion compensation within the fiber delay line.

As discussed in the previous section, the timing sensitivity of the BOC is crucial for the overall performance of the PRESTO system. A reduced timing sensitivity, which can result from improper dispersion compensation, directly impacts the system's ability to reduce noise and limits the effective bandwidth over which this noise reduction can be achieved. Therefore, precise calculation and careful implementation of the DCF are essential to maintain the timing sensitivity and ensure that the system operates at its optimal performance, achieving the desired level of noise reduction and bandwidth.

4.1.2.3. Fiber Delay Limitations: Thermal Noise Effects

In the PRESTO setup, the optical fiber delay line serves as the critical reference for stabilizing the optical source, making it essential to understand its fundamental limitations and phase noise contributions.

Although the FOG coil provides robust resilience against temperature fluctuations, strain, and vibrational effects, a deeper examination of the fiber's thermodynamic properties reveals where the fundamental limitations lie within the fiber-delay line. Despite meticulous environmental control through the design of the FOG coil, additional thermodynamic effects can lead to continuous changes in the optical path length (which affects the phase accumulated by the propagating laser field) and the stability of the propagation time (related to the group index) [118], [119]. This fundamental thermal noise, caused by apparent local temperature fluctuations in the fiber, depends on the thermal properties of the fiber material sampled by the optical mode and shows a variance or power that scales with the square of the fiber's temperature and inversely with the mode volume [120].

This effect is particularly pronounced in standard single-mode fiber (SMF), used as the fiber optic reference in the PRESTO setup, due to its high thermo-optical coefficient (TOC) [121]. The TOC of silica at 1550 nm is approximately $10 \cdot 10^{-6}$/K, which often necessitates sub-mK temperature stabilization to mitigate its effects [122].

Various theoretical models describe thermal phase noise in optical fibers, typically as a combination of two phenomena. Equation 4-13, based on [123], outlines the phase noise resulting from the interaction of the optical mode with the fiber and the contributions of these two thermal noise terms:

$$S_{\varphi}(\omega) = \frac{4\pi^2}{\lambda^2}\left[\left(\frac{dn}{dT} + n\alpha_L\right)^2 L_c^2 S_{\delta T}(\omega) + n^2 S_l(\omega)\right]$$

Equation 4-13

Here, λ represents the mode field's wavelength, dn/dt the TOC, n the refractive index of the fiber, α_L the thermal expansion coefficient and L_c the length of the fiber delay-line

The first thermal noise term $S_{\delta T}(\omega)$ is called *thermoconductive noise* defined by Foster [124] and it is qualitatively similar to the noise previously described by Wanser as thermorefractive noise [121]. This is produced by localized spontaneous thermal fluctuations producing thermal expansion and refractive index fluctuations along the fiber due to a form of energy dissipation, which then interacts with the mode propagating through the optical fiber. Equation 4-14 describes the thermoconductive noise contribution:

$$S_{\delta T}(\omega) = \frac{k_B T^2}{4\pi^2 L_c \kappa} Re\left[exp\left(\frac{i\omega r_0^2}{2D}\right) E_1\left(\frac{i\omega r_0^2}{2D}\right)\right]$$

Equation 4-14

Where k_B is the Boltzmann constant, D, refers to the thermal diffusivity, r_0^2 is the effective radius of the Gaussian power profile, and $E_1(x)$ is the special function of the exponential integral.

From this equation, one might infer that longer optical fiber, with their larger mode field volume, would exhibit less thermoconductive noise. However, the thermoconductive noise contribution to the overall thermal phase noise in Equation 4-13 is scaled by the square of the fiber length, making it proportionally dependent on this factor. Therefore, increasing fiber length to enhance PRESTO's noise reduction, as described in the feedback model in the previous section, would, in fact, raise the thermal phase noise limit.

The second thermal noise term in Equation 4-13, *thermomechanical noise*, $S_l(\omega)$, is induced by spontaneous length fluctuations in the fiber due to internal friction and was extensively studied by Duan in [123] and experimentally demonstrated in [125], [126]. This noise term becomes more prominent at infrasonic frequencies:

$$S_l(\omega) = \frac{2k_B T L_c \phi_0}{\pi^3 A_c E_0 \omega} \sum_N \frac{1}{N^2[(1-\omega^2/\omega_N^2)^2 + \phi_0^2]}$$

Equation 4-15

Where ϕ_0 is the loss angle of the fundamental mode, A_c is the cross-sectional area of the fiber, E_0 is the Young's modulus without loss and ω_N is the angular frequency of the N^th^ mode of the fiber. This term and its harmonics dominate the noise at resonance frequencies created by the fiber modes and particularly at infrasonic frequencies where $\omega \ll \omega_N$. In this regime, $S_l(\omega)$ simplifies to:

$$S_l(\omega) = \frac{2k_B T L_c \phi_0}{3\pi A_c E_0 \omega}$$

Equation 4-16

Equation 4-13 is then used to estimate the thermal phase noise limit expected from PRESTO at a specific fiber length. For the model simulation, the parameters in Table 4-2 are utilized, using the specifications from [127]:

Table 4-2. SMF parameters used in thermal phase noise model.

Parameter	Symbol	Value	Units
Boltzmann constant	k_B	$1.3869 \cdot 10^{-23}$	J / K
Central Wavelength	λ	1556	nm
Effective refractive index	n	1.468	-
Thermal conductivity	κ	1.37	$W \cdot m^{-1} \cdot K^{-1}$
Thermal diffusivity	D	$8.2 \cdot 10^{-7}$	m^2 / s
Thermal expansion coefficient	α_L	$1.05 \cdot 10^{-6}$	K^{-1}
Mode-field radius	a_m	$5.25 \cdot 10^{-6}$	m
Fiber diameter	d_f	$125 \cdot 10^{-6}$	m
Cross-sectional Area	A_c	$\pi d_f^2/4$	m^2
Effective radio, Gaussian field	r_o	$\sqrt{a_m^2/2}$	m
Fiber length	L_c	2 x 1042	m
Mode loss angle	ϕ_0	0.1	-
Young's Modulus	E_0	$68 \cdot 10^9$	Pa

Figure 4-9.a displays the thermal noise simulation results for a nearly 2 km fiber link, similar to that used in PRESTO. It can be observed that for frequencies below 1 kHz, thermomechanical

noise dominates, while above 1 kHz, thermoconductive noise is the primary factor. This thermal noise behavior could define the ultimate limit on the achievable noise reduction by PRESTO. Figure 4-9.b shows the 10 GHz scaled version of the phase noise, representing the ideal phase noise limit of a 10 GHz microwave signal synthesized by a comb line in PRESTO. However, as seen in the experimental results in the following section, this ideal phase noise lies below the current measured phase noise for the synthesized 10 GHz signal.

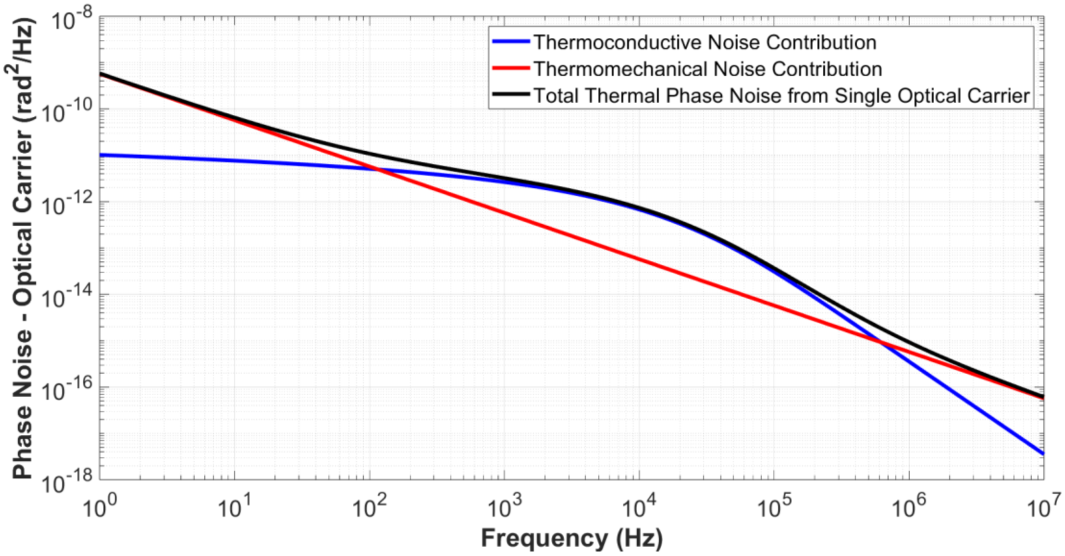

(a)

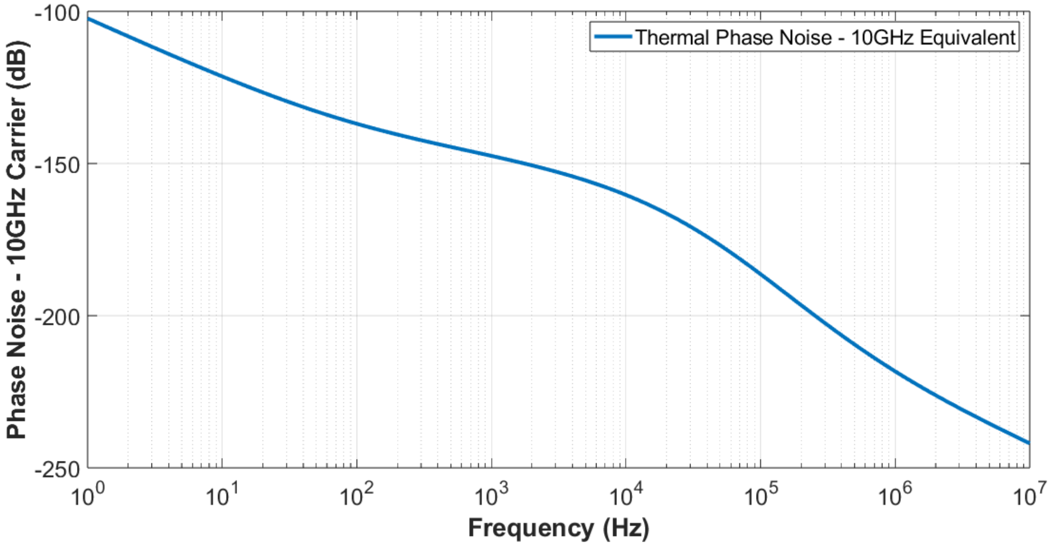

(b)

Figure 4-9. Expected Thermal Phase Noise from Fiber Delay Line of 2 km length in PRESTO.

(a) Phase Noise of the optical carrier at 1556 nm, (b) Scaled Phase Noise in for a 10 GHz carrier frequency

4.2. PRESTO: IMPLEMENTATION AND EXPERIMENTAL RESULTS

With the core concept of PRESTO established, along with its noise reduction dynamics and potential limitations, the next step is to detail its experimental implementation and performance evaluation.

4.2.1. Experimental Setup

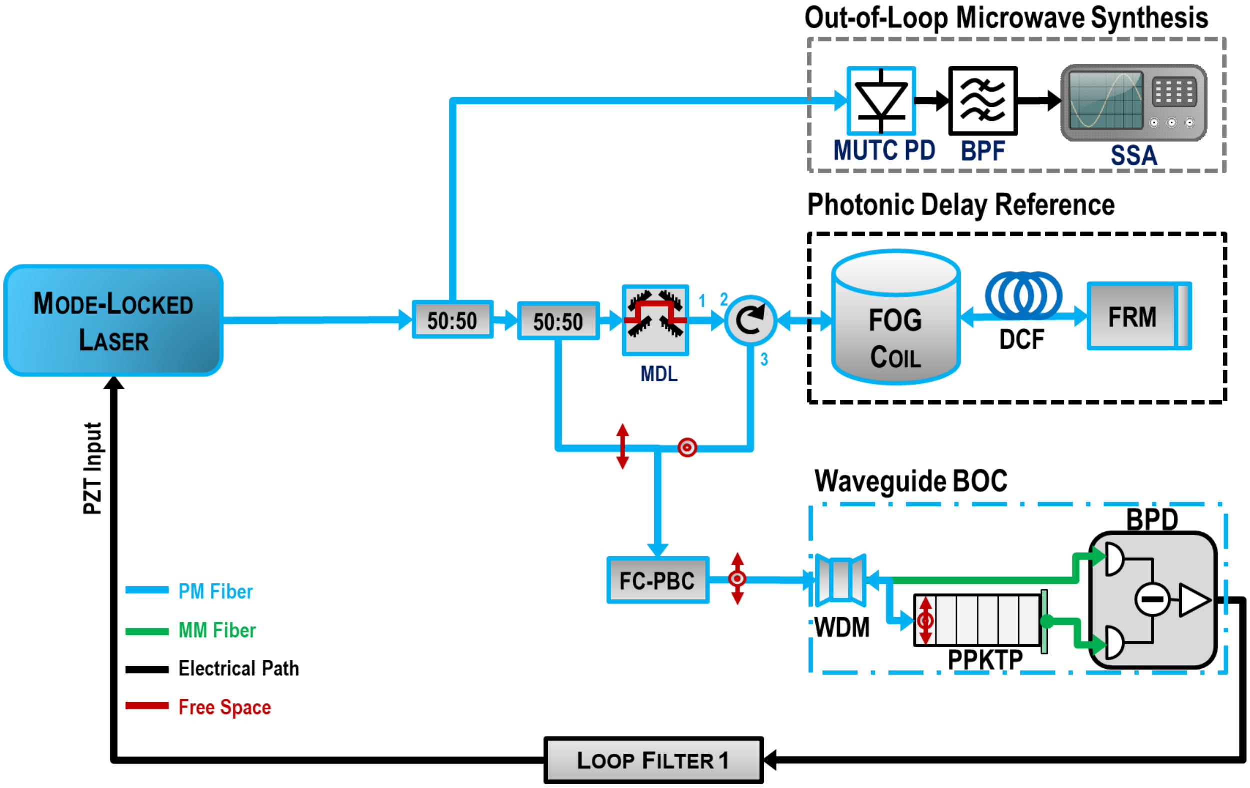

Figure 4-10. Schematic of the experimental implementation for PRESTO.

MUTC: Modified Uni-Traveling-Carrier Photodetector, BPF: Electrical Band Pass Filter, SSA: Signal Source Analyzer, MDL: Motorized Delay Line, DCF: Dispersion Compensating Fiber, FRM: Faraday Rotating Mirror, Fc-PBC: Fiber-Coupled Polarization Beam Combiner, WDM: Wavelength Division Multiplexer, PPKTP: Periodically Poled Potassium Titanyl Waveguide, DC: Dichroic Coating, BPD: Balanced Photodetector, PM: Polarization Maintaining Fiber, MM: Multimode Fiber

Figure 4-10 depicts the experimental setup for the photonic microwave oscillator, PRESTO, which is based on a fiber optic delay reference and a pulse timing detector. The core of the oscillator is a commercially available mode-locked laser (MENHIR-1550) that operates at a 1 GHz repetition rate with a center wavelength of 1564 nm. The specific parameters of this laser are detailed in Table 4-3, and additional features and characterization are found in Appendix B.2.

The fiber optic delay reference is composed of approximately 1000 meters of standard single-mode fiber, which is coiled into a fiber gyroscope configuration. This is followed by around 140 meters of DCF and terminated with a Faraday rotating mirror, making the total fiber length approximately 1140 meters. The role of the DCF is crucial for counteracting the chromatic dispersion introduced by the single-mode fiber, ensuring that the pulses maintain their duration and energy as they traverse the delay line.

The optical pulse timing detector utilized in this setup is the waveguide-based balanced optical cross-correlator (WBOC), previously discussed in Section 2.1.2. In the experiment, the laser pulses traverse the delay reference twice, and then return in an orthogonal polarization, thanks to the faraday rotating mirror at one end of the fiber delay-line. Afterwards, the delayed pulse train recombines with the fresh pulse train using a fiber-coupled polarization beam combiner (FC-PBC). To ensure that the counterpropagating pulse trains arrive at the WBOC at nearly identical times—allowing the WBOC to operate in its most sensitive region—a motorized delay line (MDL) is inserted into the setup for fine adjustments.

The WBOC then produces a baseband signal that is proportional to the timing difference between the original pulse train and its delayed counterpart. This signal is used as the input to a primary feedback loop, which is connected to the mode-locked laser. The feedback loop adjusts the intracavity piezoelectric element, effectively locking the laser's repetition rate to the fiber delay reference.

Table 4-3. Mode-locked laser specifications for PRESTO.

Parameter	**Value**	**Units**
Repetition Rate	999.988	MHz
Center Wavelength	1564	Nm
Power at Output	45	mW
Optical Bandwidth	13	Nm
Pulse Width	200	fs
Output Pulse Width	500	fs
Integrated Timing Jitter (up to 1 kHz)	7.8	fs

A fraction of the laser's output is diverted from the loop for integration into the microwave synthesis framework. This setup employs a Freedom Photonics photodetector (FP1015a), with an MUTC structure as discussed in Section 3.2.6, with a 22 GHz bandwidth and designed to handle optical power up to 100 mW and generate substantial RF power. At the end of the photodetector, a 10 GHz bandpass filter with a 100 MHz bandwidth is used to extract the 10th harmonic from the 1 GHz optical pulse train produced by the mode-locked laser. This synthesized 10 GHz signal represents the primary output of the photonic microwave oscillator, and its performance characterization will be the benchmark for evaluating the success of this work.

4.2.1.1. In-Loop Timing Jitter Insights

To gain insight into the noise reduction dynamics of the PRESTO system, the output of the WBOC was monitored, using the signal source analyzer (SSA) R&S®FSWP as a baseband analyzer to assess the in-loop timing jitter, by converting the baseband noise into jitter spectral density while using the detector's timing sensitivity.

Given the high sensitivity at which the WBOC operates, even a unit gain in the feedback loop is sufficient to drive the system to the resonance point of the piezoelectric element within the laser, as shown in Figure 4-11.

Starting with a lower gain, it is observed that the locking bandwidth of PRESTO expands in conjunction with the degree of noise reduction achieved in the laser's operation. As the feedback loop gain increases from -5 dB to 0 dB, the system's locking bandwidth progressively approaches the resonance frequency of the PZT. At this point, any further attempt to increase the feedback loop gain—aimed at enhancing noise reduction—becomes counterproductive. The system enters a regime where the feedback loop is dominated by a pronounced noise peak at the PZT's resonance frequency. This peak effectively limits the ability of the feedback loop to further reduce noise, marking a critical threshold in the system's performance.

This phenomenon represents a significant limitation of the current experimental setup. The resonance-induced noise peak not only constrains the achievable noise reduction but also restricts the effective bandwidth over which the system can operate. To address this challenge and enhance the system's performance, additional strategies must be implemented.

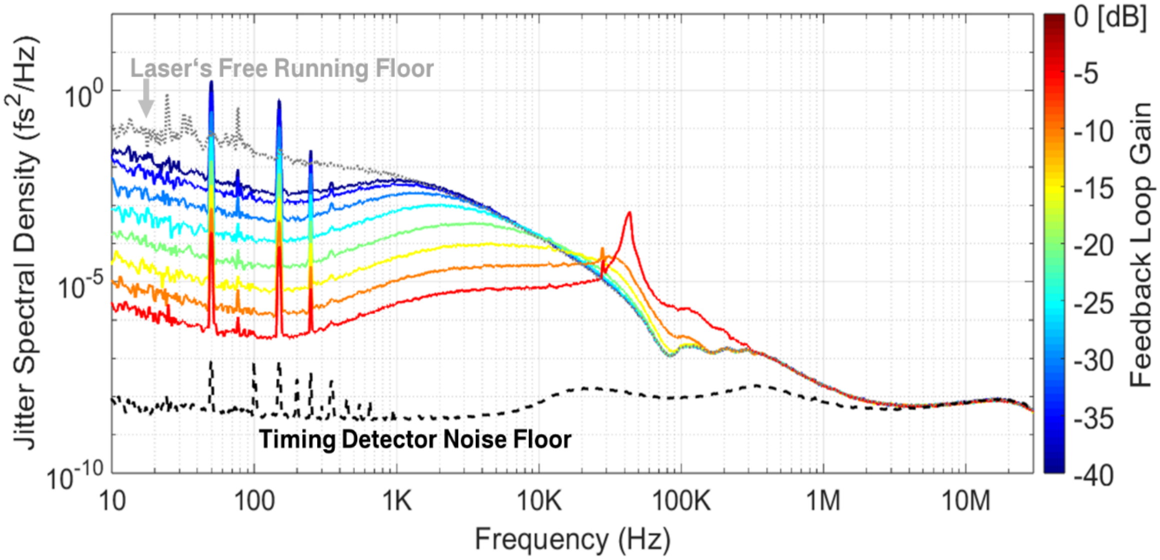

Figure 4-11. In-loop timing jitter of the PRESTO setup as a function of increasing feedback loop gain.

4.2.1.2. Microwave Characterization

The microwave characterization of PRESTO's output was performed using the R&S$^{®}$FSWP signal source analyzer (details on its phase noise characteristics and measurement procedures can be found in Appendix A.3). To achieve optimal RF signal conversion, the photodetector was illuminated with approximately 5 mW of optical power, producing a 10 GHz microwave signal with an RF power level of -7 dBm. Figure 4-12.a presents the phase noise spectrum of this generated signal, compared to that of the free-running laser. All measurements were conducted with a -5 dB feedback loop gain.

In the phase noise spectrum, a resonance peak emerges around 50 kHz, which corresponds to the resonance frequency of the PZT within the laser cavity. This resonance imposes a significant limitation on the extent of noise reduction achievable through the feedback loop. The presence of this peak is particularly discouraging because, ideally, increasing the locking bandwidth could further reduce the overall noise, especially within the 10 kHz region of the phase noise spectrum, where noise reduction would be most beneficial.

However, despite these limitations, Figure 4-12.b demonstrates a significant improvement in integrated timing jitter up to 1 Hz, with a reduction of nearly two orders of magnitude, achieving sub-100 fs levels. This improvement is most pronounced at lower offset frequencies, underscoring the effectiveness of the PRESTO setup in reducing noise and enhancing the stability of the microwave signal. While the resonance-induced limitations are a challenge, the system still achieves substantial noise reduction, particularly in the critical low-frequency range, which is essential for high-precision applications.

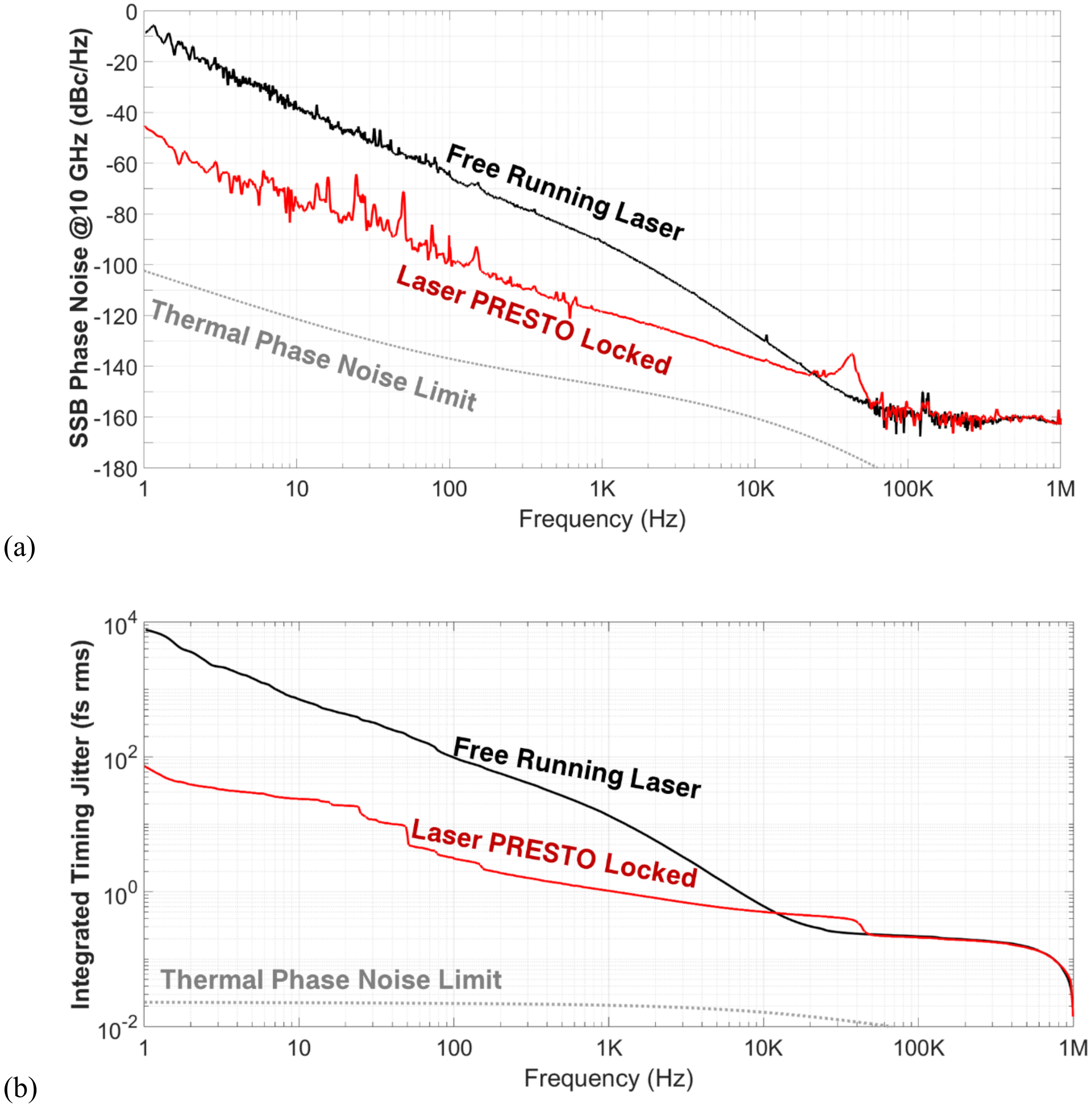

Figure 4-12. Characterization of 10 GHz microwave output from PRESTO.

(a) Single side band phase noise: comparison between free-running laser and laser locked to fiber delay reference, (b) integrated timing jitter up to 1 Hz

4.2.2. Experimental Setup 2.0

After validating the PRESTO concept with the initial experimental setup and identifying technical constraints—particularly the resonance frequency limitation of the PZT—an improved approach was developed: integrating a secondary feedback loop with a broader bandwidth. This additional loop utilizes an electro-optical phase modulator (EOM-PM) with a 100 MHz bandwidth, enabling finer phase correction once the primary feedback loop is engaged.

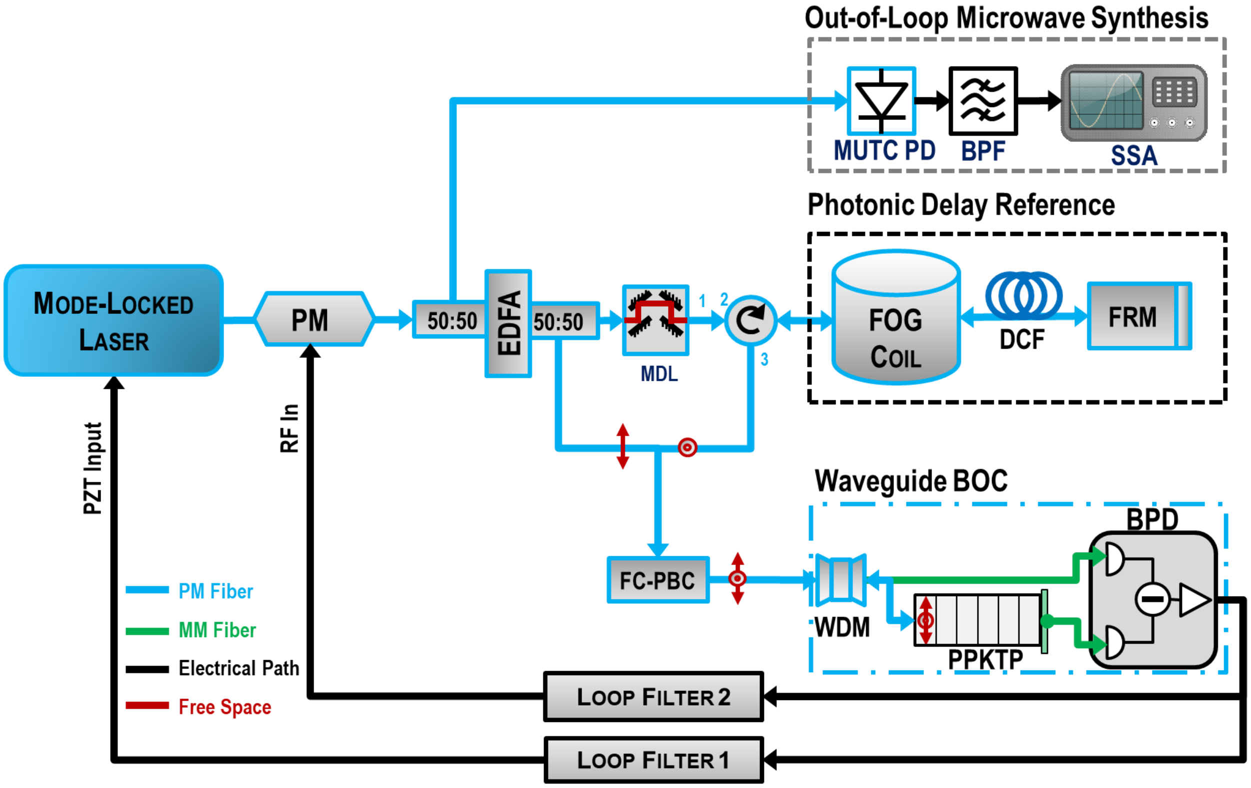

Figure 4-13. Schematic of the experimental implementation for PRESTO with a double feedback scheme.

MUTC: Modified Uni-Traveling-Carrier Photodetector, BPF: Electrical Band Pass Filter, SSA: Signal Source Analyzer, MDL: Motorized Delay Line, DCF: Dispersion Compensating Fiber, FRM: Faraday Rotating Mirror, Fc-PBC: Fiber-Coupled Polarization Beam Combiner, WDM: Wavelength Division Multiplexer, PPKTP: Periodically Poled Potassium Titanyl Waveguide, DC: Dichroic Coating, BPD: Balanced Photodetector, PM: Polarization Maintaining Fiber, MM: Multimode Fiber, EDFA: Erbium-doped fiber amplifier, PM: Phase modulator

To compensate for the additional losses introduced by the EOM-PM, a custom-built Erbium-Doped Fiber Amplifier (EDFA) is integrated into the system. This EDFA, incorporating 1.5 meters of gain fiber, boosts the available optical power, thereby enhancing the timing sensitivity of the

WBOC. The updated system schematic, illustrated in Figure 4-13, depicts the incorporation of this secondary feedback loop into the existing setup

The stabilization process begins by locking the primary feedback loop at a lower gain, establishing a stable lock to the reference fiber-delay line. Once the first loop is locked, the secondary feedback loop, which controls the fast EOM-PM at the femtosecond laser's output, is activated. This secondary loop is essential for high-frequency noise suppression, mitigating the resonance limitations of the PZT. However, to maintain system stability, the secondary loop can only be engaged once the primary loop has successfully locked the laser to the reference fiber delay-line. This ensures that optical phase or delay adjustments remain within the dynamic range of the phase modulator, which is approximately one optical cycle at 1564 nm (~5 fs).

4.2.2.1. In-Loop Timing Jitter Characteristics

As in the previous setup, the first step in this analysis involves examining the output of the WBOC, which provides the error signal used for stabilization. This is achieved using the R&S®FSWP in baseband mode, where the baseband noise spectrum is converted into jitter spectral density. This conversion relies on the timing sensitivity of the detector, ensuring accurate characterization of the system's performance at this stage of the experiment.

Once the initial analysis is complete, the feedback loop controlling the laser's PZT actuator is engaged. The loop gain is progressively increased, pushing the locking bandwidth as close as possible to the resonance frequency of the PZT element. At this critical point, the secondary feedback loop is activated, which significantly expands the locking bandwidth and suppresses the resonance peak associated with the PZT.

A key observation is that activating the second loop allows for an additional 10 dB increase in loop gain, exceeding the stability limits of the single-loop configuration. This enhancement facilitates greater noise suppression, particularly at lower frequencies, without being restricted by resonance peaks typically observed in the kilohertz region.

Figure 4-14 presents a comparison between the maximum noise reduction achieved using a single-loop setup and the further reduction enabled by the dual-loop configuration. This comparison underscores the effectiveness of the dual-loop system in mitigating PZT resonance limitations, leading to a more stable and precise locking mechanism and enhanced phase noise suppression.

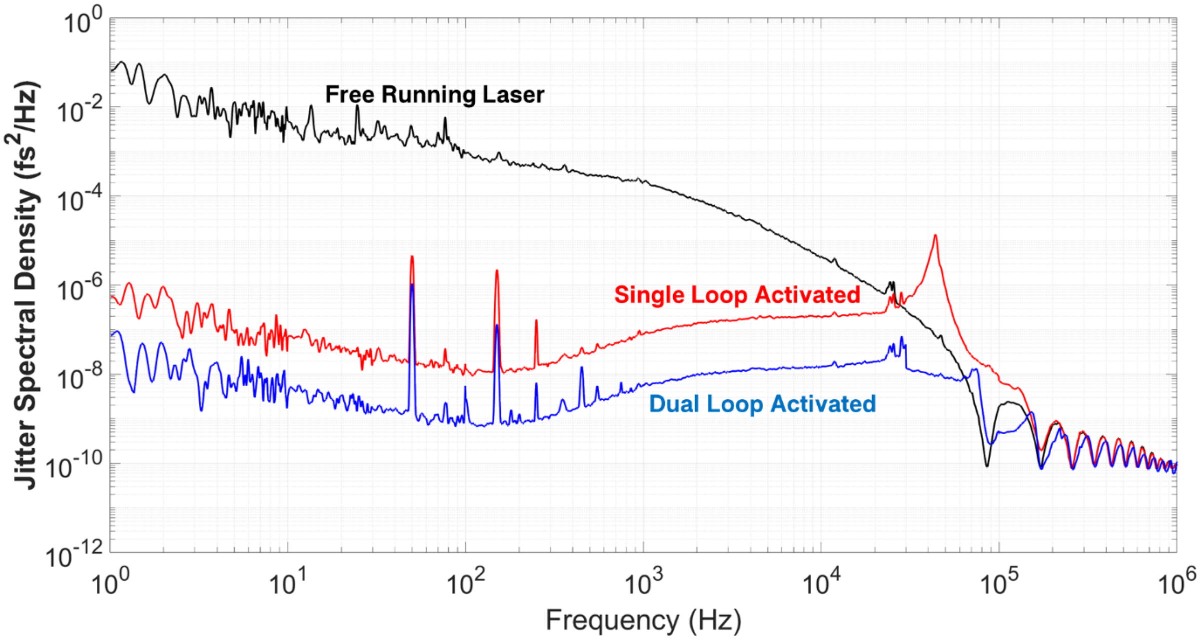

Figure 4-14. In-loop timing jitter of the PRESTO setup for single and dual feedback loop.

4.2.2.2. Microwave Characterization of the Dual-Loop PRESTO

To further evaluate the impact of the dual-loop stabilization, a microwave characterization of the out-of-loop synthesized signal was performed. Figure 4-15.a presents a detailed comparison of the microwave output phase noise for three configurations: free-running mode-locked laser, single-loop locked PRESTO, and dual-loop locked PRESTO. The results confirm that the projected in-loop noise reduction of approximately 15 dB is directly reflected in the microwave domain. This improvement extends across the spectrum, effectively suppressing phase noise down to 50 kHz offset and eliminating the resonance peak at this frequency.

Additionally, Figure 4-15.b illustrates the impact of the dual-loop stabilization on the integrated timing jitter. The results demonstrate a significant improvement, with total timing jitter decreasing from ~100 fs in the single-loop configuration to just ~30 fs when the dual-loop locking mechanism is engaged (integrated down to 1 Hz). This substantial reduction underscores the effectiveness of the dual-loop system in improving phase noise performance and overall stability of the PRESTO microwave output, making it a highly promising approach for ultra-stable photonic microwave generation.

(a)

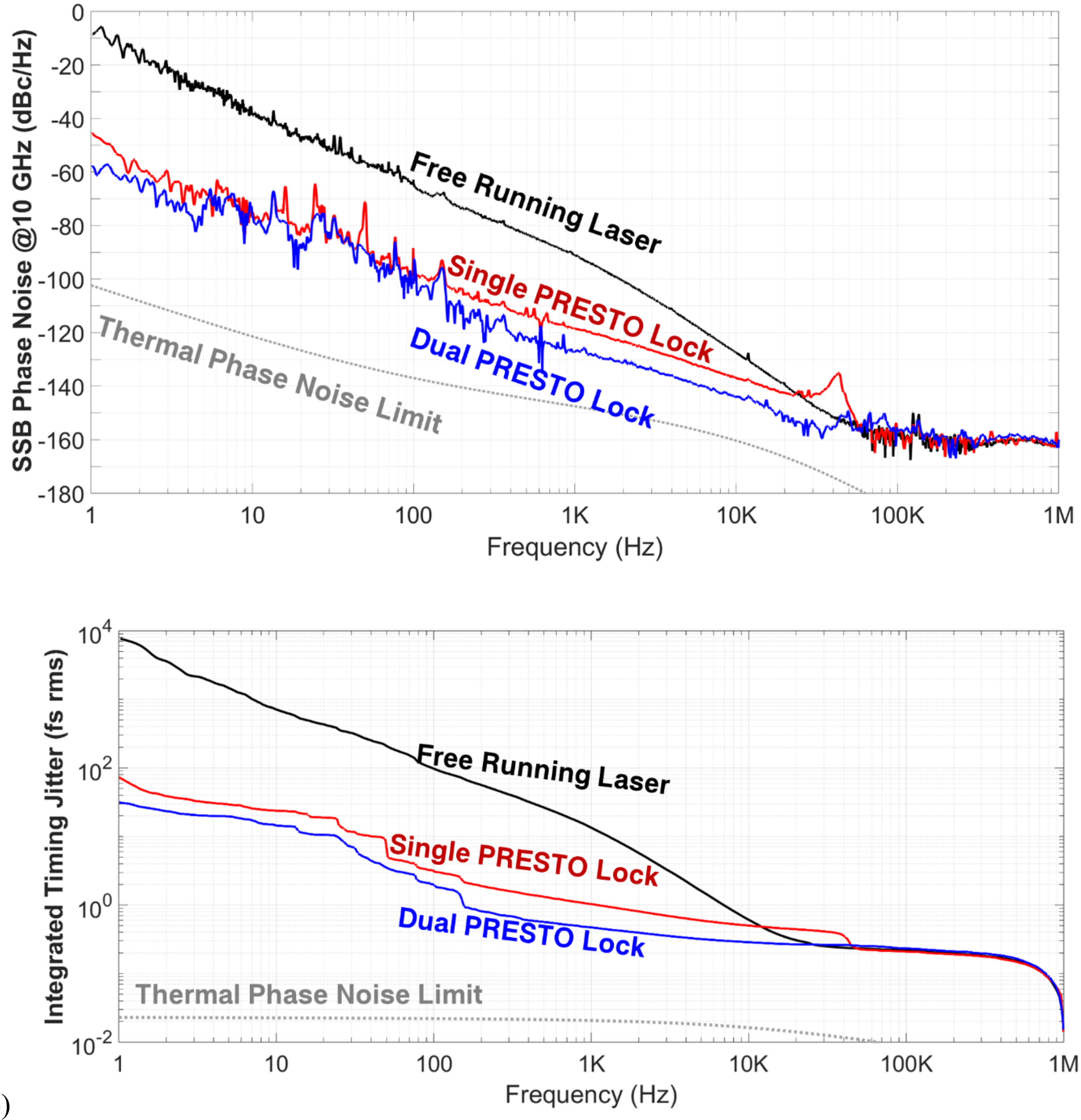

(b)

Figure 4-15. Characterization of 10 GHz microwave output from PRESTO for Single and Dual Feedback Loop. (a) Single side band phase noise: comparison between free-running laser and laser locked to fiber delay reference for single loop with PZT and double loop with EOM-PM, (b) integrated timing jitter up to 1 Hz

4.2.3. Microwave Relative Timing Jitter to the Laser Source

An additional characterization was conducted to evaluate the relative timing jitter between the RF signal generated by microwave synthesis at the PRESTO output and the optical pulse train from the stabilized mode-locked laser. This measurement was performed using the BOMPD, as described in Section 2.2. By directly comparing the microwave phase fluctuations to the stabilized optical pulse train, this analysis provides a precise assessment of how effectively PRESTO transfers the optical frequency stability into the RF domain.

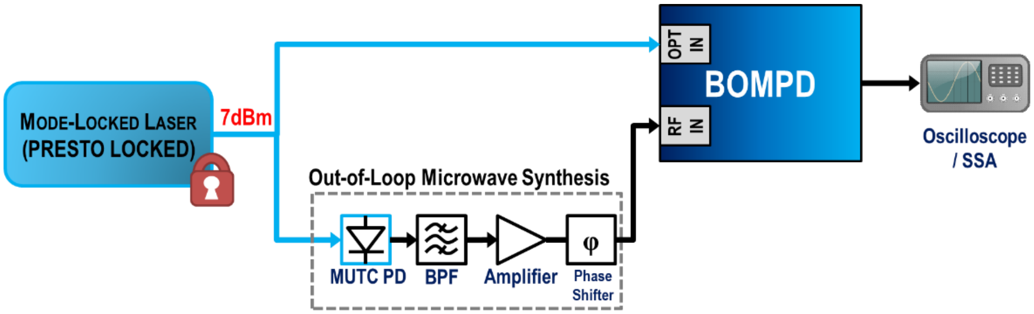

Figure 4-16. Out-of-loop optical to microwave timing jitter characterization setup.

To begin, the timing sensitivity of the BOMPD for this specific setup must be determined. This is achieved by connecting a frequency synthesizer—with a power level similar to that of the microwave synthesis signal—to the RF input of the BOMPD, replacing the microwave synthesis source in Figure 4-16. A slight frequency shift is introduced in the RF synthesizer (in the order of a few hundred hertz), causing the BOMPD output voltage to generate a beat note frequency (f_{beat}) corresponding to this frequency shift.

The real-time response of the BOMPD is then determined using the following relation: $\tau_{\mathrm{BOMPD}} = \tau_{\mathrm{OSC}} f_{beat} / f_{\mathrm{RF}}$, where τ_{OSC} is the time recorded on the oscilloscope. Figure 4-17 presents the measured sensitivity at the zero-crossing for a beat note of 100 Hz, yielding approximately 0.13 mV/fs.

This relatively low sensitivity is primarily attributed to the limited optical power available from the mode-locked laser, which is divided between the microwave synthesis and characterization processes. As a result, the power available at both the optical and RF inputs of the BOMPD is reduced. Nevertheless, as will be demonstrated in the following analysis, the relative timing jitter is not constrained by the BOMPD's noise floor, even at this reduced sensitivity.

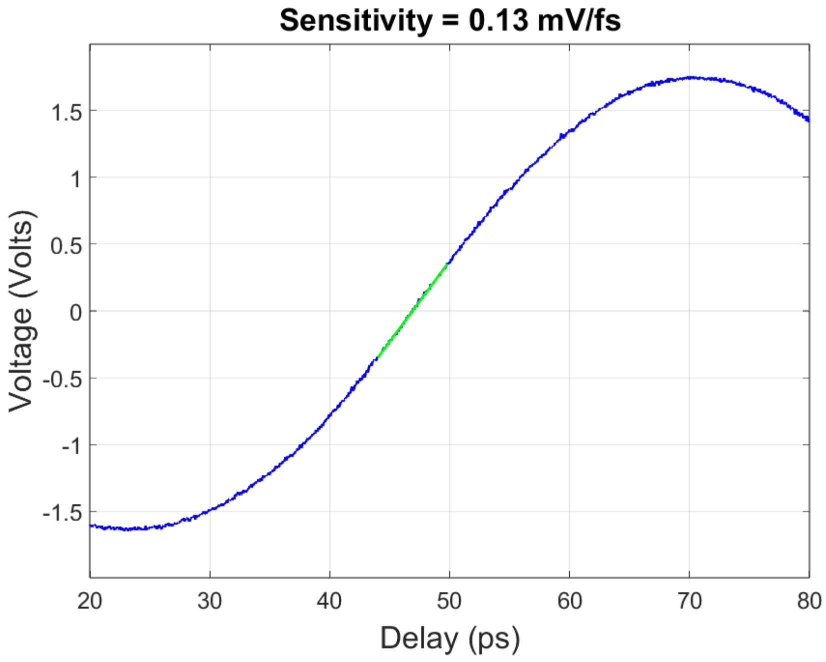

Figure 4-17. BOMPD Sensitivity Measurement at the Zero-Crossing from a 100 Hz Beat Note Signal.

To measure the relative jitter, the amplified 10 GHz signal generated by the microwave synthesis is connected to the RF input of the BOMPD, as depicted in Figure 4-16. A phase shifter is employed to ensure that the detector operates precisely at the zero-crossing of the microwave signal. The noise floor of the BOMPD is also characterized as described in Section 2.2.3.

Figure 4-18.a presents the baseband measurement results, transformed into the jitter spectral density of the microwave signal relative to the optical pulse train. Here, it is confirmed that the measurement is not constrained by the detector's noise floor.

Figure 4-18.b illustrates the integrated timing jitter from 1 Hz to 20 MHz, showing a value of approximately 11 fs RMS for the microwave signal relative to the mode-locked laser. This demonstrates how the stability of the laser is effectively transferred to the microwave signal synthesized from the pulse train. Furthermore, it highlights that any improvements to the laser's noise performance will directly enhance the photonic microwave oscillator scheme presented in this study.

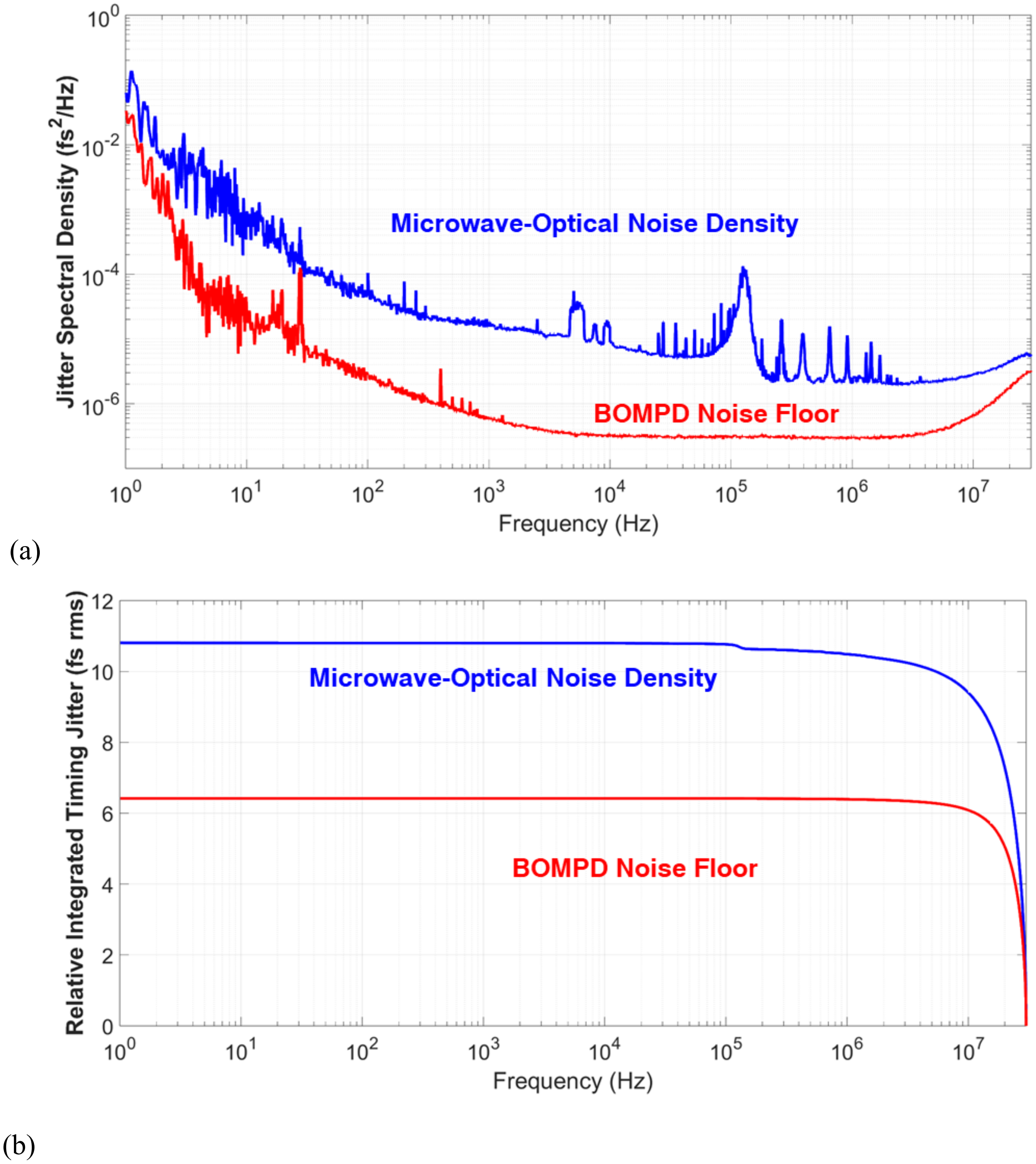

Figure 4-18.Relative Timing Jitter Measurements from the Photonic Microwave Oscillator in Comparison with the Stabilized Optical Source.

(a) Jitter Spectral Density and Noise Floor of the BOMPD, (b) Integrated Timing Jitter from 1 Hz to 30 MHz bandwidth

5. CONCLUSIONS AND OUTLOOK

5.1 SUMMARY OF RESEARCH AND KEY FINDINGS

This work has investigated different types of photonic based microwave oscillators and studied their scope and advantages; in addition, this work has introduced the Photonically Referenced Extremely Stable Oscillator (PRESTO), a simple yet effective approach to ultra-low phase noise microwave generation. The research tackled fundamental challenges in photonic microwave synthesis, particularly in timing jitter reduction through frequency stabilization of mode-locked lasers.

One of the fundamental features of this work was the development of timing characterization tools, where the Balanced Optical Cross-Correlator (BOC) took center stage for both optical source characterization and for stabilizing the optical fiber reference in PRESTO. The work on an integrated waveguide BOC contributed to the main achievement of this work by achieving higher timing sensitivities at lower pulse energies coming from GHz repetition rate mode-locked lasers, while at the same time opening for further potential integrations, particularly where size is a constraint. This advancement introduces the means to fully integrated photonic microwave oscillators, which may utilize chip-scale optical frequency combs and on-chip photodiodes.

Implementation of the Balanced Optical Microwave Phase Detector (BOMPD) was also critical in this study, offering precise characterization of synthesized microwave signals thanks to its timing sensitivity at the femtosecond level, enabling relative timing jitter precision in optical-to-microwave phase detection.

The overall design of PRESTO, employing a fiber delay-line and a feedback loop stabilization system based on BOC timing detection, demonstrated significant suppression of intrinsic timing noise. Experimental validation confirmed a phase noise reduction of up to 30 dB in near-to-carrier offset frequencies. The introduction of a secondary feedback loop in PRESTO further enhanced high-offset frequency suppression, improving phase noise performance by approximately 10 dB. Compared to the free-running laser, phase noise suppression exceeded 40 dB at offset frequencies below 1 kHz. At higher offset frequencies, the phase noise floor of -165 dBc/Hz beyond 100 kHz is currently limited by the phase modulator and the available photocurrent at the 10 GHz harmonic. The integrated timing jitter, improved from ~10 ps RMS in the free-running laser, was reduced to an impressive 30 fs RMS over a bandwidth of 1 Hz – 1 MHz.

5.2 COMPARATIVE ANALYSIS AND IMPACT OF PRESTO

Figure 5-1 compares PRESTO's absolute phase noise with state-of-the-art photonic microwave oscillators. Optical frequency division (OFD) remains the benchmark for ultra-low phase noise, with OFD1 representing the record performance reported in [39], while OFD2 denotes a relatively compact, transportable version [41]. Another promising approach is electro-optical frequency division (eOFD), which utilizes an electro-optic comb. While eOFD exhibits slightly higher phase noise than OFD, it still outperforms other PMOs [30]. A photonic chip-based version of eOFD has also been demonstrated, positioning it as a direct competitor to PRESTO, though it still faces technical challenges [28].

Despite the exceptional phase noise performance of optical frequency division techniques, their bulkiness, complexity, and high cost pose significant drawbacks. PRESTO offers a compelling alternative, as it provides a simpler implementation. Instead of relying on large optical cavities or ultra-stable CW laser references, PRESTO is based on a fiber-optic delay line, reducing system complexity while maintaining high performance.

Other photonic microwave oscillator implementations, such as mode-locked lasers stabilized by fiber delay lines (MLL DL) [128] and microcombs stabilized using fiber delay lines (μC DL) [108], are also compared. While promising, these techniques do not consistently outperform PRESTO in the critical 1 kHz – 100 kHz offset frequency range. They rely on interference between only two optical frequencies extracted from a broader optical spectrum containing thousands of frequencies. This narrow filtering process significantly reduces the optical signal power available for phase noise detection. Additionally, these interferometric techniques require broad optical bandwidths for high noise sensitivity, as well as complex electronics incorporating external acousto-optic or electro-optic modulators to isolate and retrieve the phase noise of the pulse repetition rate. Moreover, they are more susceptible to increased noise floors due to optical backscattering in fiber and laser source relative intensity noise.

The best-performing optoelectronic oscillator (OEO) [24], also shown in Figure 5.1, remains competitive. However, PRESTO exhibits comparable to better performance in crucial offset frequency regions.

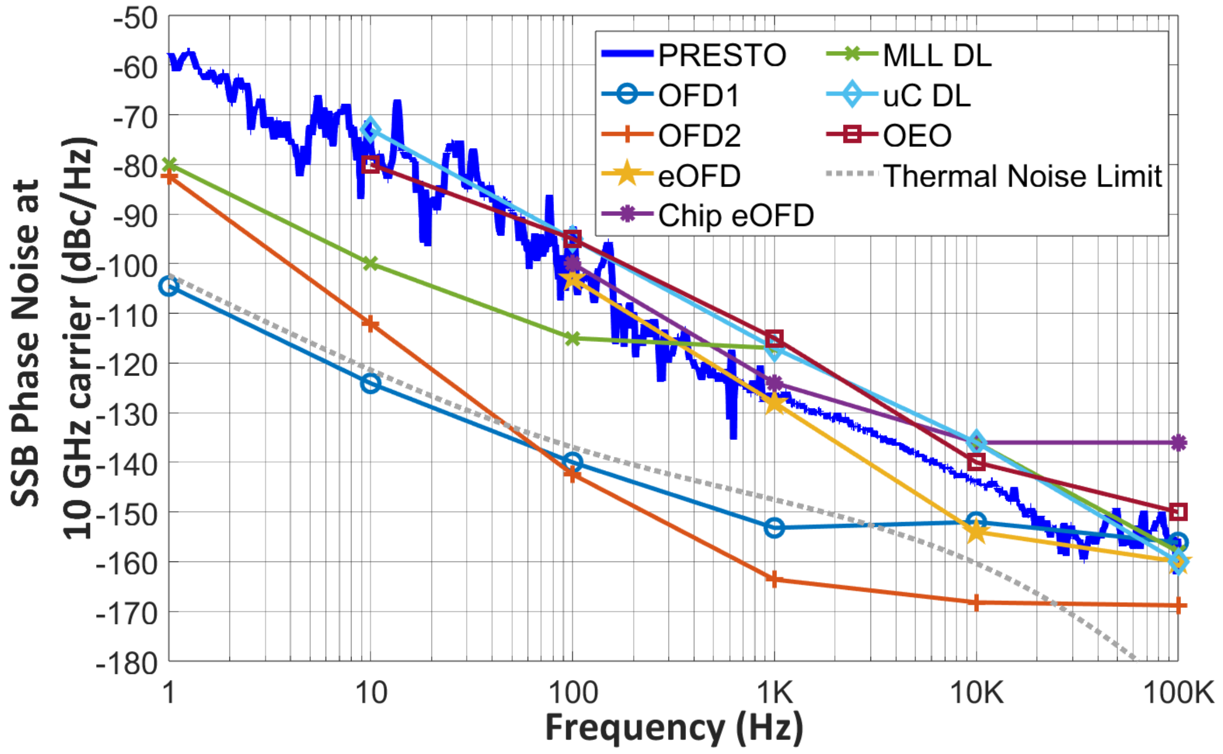

Figure 5-1. Comparison of PRESTO's phase noise performance with other photonic microwave oscillators.

OFD1: optical frequency division in [39], OFD2: compact and transportable OFD shown in [41], eOFD: electro-optical frequency division in [30], Chip eOFD: photonic chip eOFD setup results in [28], MLL DL: mode-locked laser stabilization by single optical frequencies using fiber delay lines shown in [128], uC DL: Microcomb stabilized by fiber delay line shown in [108], OEO: best results from optoelectronic oscillators shown in [24]

5.3 OUTLOOK

Despite the significant advancements demonstrated in this work, further research is required to optimize the performance of PRESTO and expand its applicability. The fiber delay-line remains a crucial component in the system, and exploring its length variations and their effects on phase noise reduction could lead to further improvements. Enhancing thermal and mechanical isolation techniques may help mitigate environmental fluctuations, while addressing nonlinear effects and dispersion compensation could improve long-term stability.

The actuation mechanism also presents an area for innovation. Replacing the PZT-based stabilization system with broadband actuators, such as microelectromechanical systems (MEMS) or optical phase modulators with a larger dynamic range, could enhance performance. Implementing adaptive feedback control algorithms would further optimize the system response by dynamically adjusting loop gain and minimizing spurious resonance effects.

Another critical step in PRESTO’s evolution is its integration with Photonic Integrated Circuits (PICs). A chip-scale implementation would significantly reduce size, cost, and power consumption, making PRESTO more viable for widespread applications. Integrating mode-locked lasers, photodiodes, and timing detectors into a single monolithic photonic circuit would greatly improve system robustness. Exploring hybrid integration strategies with silicon photonics would provide additional avenues for manufacturability and long-term reliability.

Currently, the PRESTO setup is being engineered into a 6” height units rack-mountable housing, constrained primarily by the size of the mode-locked laser. However, the PRESTO concept is compatible with various fiber and chip-scale mode-locked lasers, which can further increase its potential for miniaturization. Some system components, such as the delay reference and timing detector, are already compact and can be integrated into much smaller volumes. With continued advancements, PRESTO has the potential to redefine photonic oscillators by simplifying their structure, reducing size, and lowering costs, making them more accessible for emerging applications in metrology, aerospace, and quantum technologies.

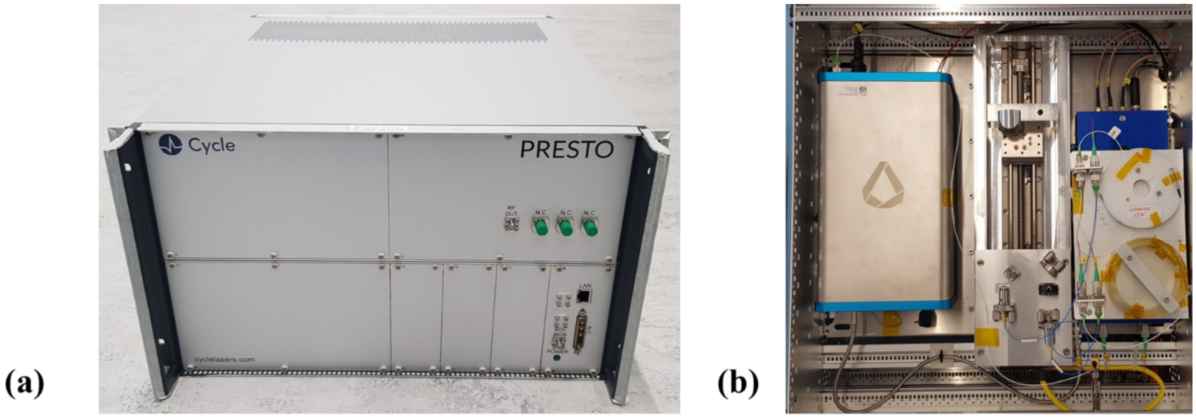

Figure 5-2. Further implementation of PRESTO in a 6U rack unit

(a) 6U Rack unit outside view, (b) top view from exhibiting the mode-locked laser, motorized delay line and optical fiber timing components.

5.4 CONCLUDING REMARKS

This dissertation provides a significant contribution to the milestones in photonic microwave generation. PRESTO is a promising alternative to ultra-stable microwave synthesis. With its foundation in mode-locked laser stability and fiber-based referencing, this type of photonic microwave oscillator provides outstanding frequency stability and phase noise performance, making it a desirable solution for precision timing, communications, and scientific instrumentation.

Future work includes increased miniaturization, system integration, and broader frequency coverage. Improving fiber stabilization techniques, refining actuator technology, and incorporating photonic technology integration will be crucial to advancing photonic microwave oscillators. As the demand for ultra-stable microwave sources continues to grow, PRESTO sets a solid foundation for next-generation timing and frequency standards, bridging the gap between laboratory research and real-world applications.

APPENDIX:

PHASE NOISE AND STABILITY IN OSCILLATORS

This section introduces the basic concept of oscillator stability, central to this thesis, and defines the main metrics and instruments used for its characterization.

Stability in oscillators means the ability of oscillators to resist frequency deviations due to internal and external factors. This includes everything from short-term fluctuations to long-term trends driven by factors such as temperature, aging, and other environmental changes.

Phase noise and jitter metrics quantify short-term stability, showing fluctuations over periods from millisecond to second scales. Long-term stability is given by parameters such as frequency drift and Allan deviation, which get modified over periods of minutes to days. These metrics provide a comprehensive understanding of oscillator performance under dynamic conditions. This Appendix will be primarily focused on the characterization of short-term stability in oscillators.

A.1. PHASE NOISE AND TIMING JITTER

The most important metric characterizing the short-term stability of an oscillator is its phase noise. This is given by the random fluctuations in the phase of the oscillator signal.

To understand the effect of noise on an oscillator, consider a theoretical pure sinusoidal signal, as shown in Figure 0-1.a. There, the amplitude and phase of this signal do not change with time. Realistic oscillators subjected to noise behave much more like the superimposed signal shown in Figure 0-1.b. Here, the amplitude A_o is modulated by a random signal $A_n(t)$, which accounts for amplitude fluctuations over time. $\varphi_n(t)$ determines the phase noise and is related to the frequency stability of the signal. The power spectrum of these two signals, shown in Figure 0-1..c and Figure 0-1..d, illustrates how noise affects the ideal oscillator, causing the power spectrum of a single frequency to broaden. This results in modulation of the carrier by random fluctuations in amplitude and phase (noise components), as shown by the sidebands.

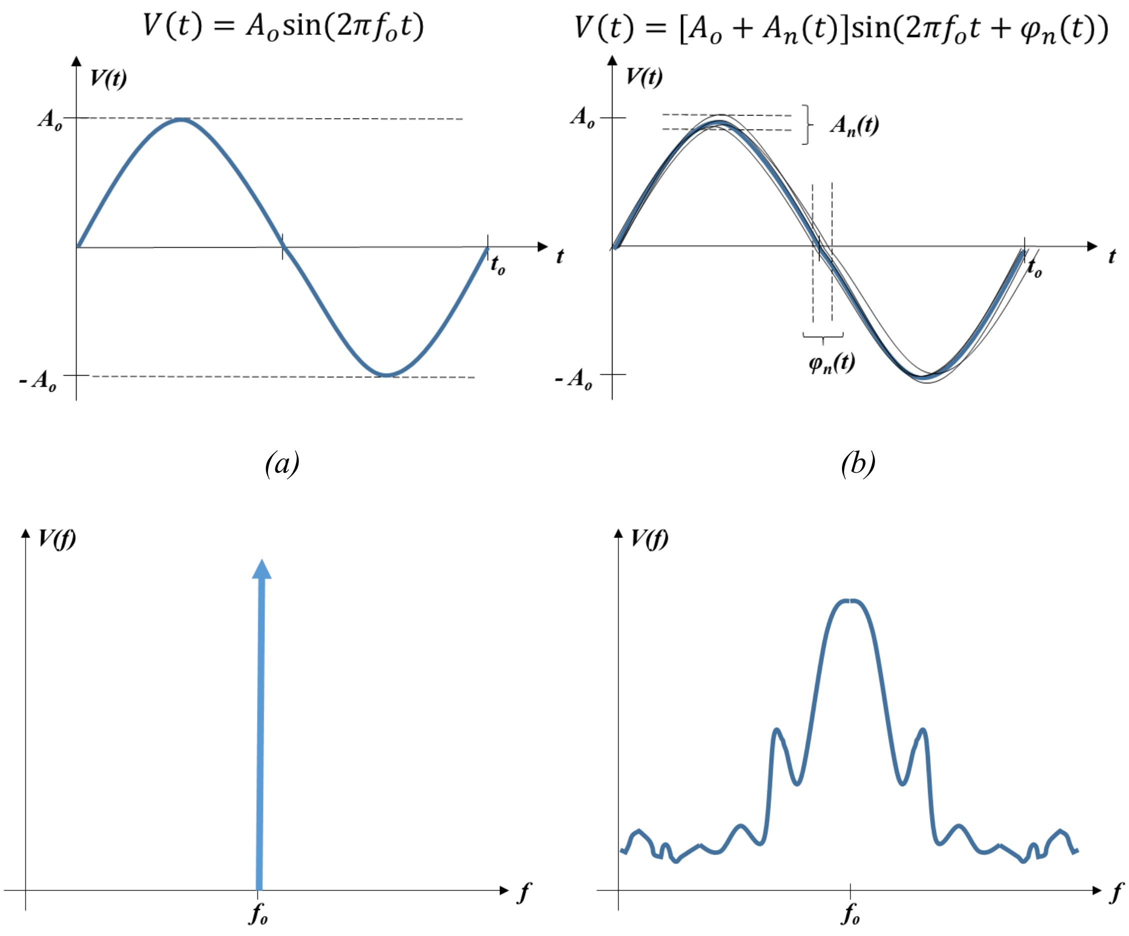

(a) (b)

(c) (d)

Figure 0-1. Ideal and real representation of a sinusoidal continuous signal in time and frequency

Ideal sinusoidal signal (a) in the time domain and (c) in the frequency domain. (b) Real sinusoidal signal affected by noise in the time domain and (d) its frequency representation.

The broadening of the power spectrum of the signal includes contributions from both sources of noise. This fact necessitates the development of specific measurement mechanisms to effectively differentiate between the influences of amplitude noise and phase noise in the signal under test.

A common method employed in metrology for determining these magnitudes is described. For this purpose, the noisy signal depicted in Figure 0-1.b is used in a mixer setup with a reference signal at oscillating at the same frequency, but exhibiting a relative lower noise and a known fixed phase offset component ($\Phi_r(t)$). In this configuration, $A_n(t)$ and $\varphi_n(t)$ denote the zero-mean amplitude and phase noise components of the oscillator signal, respectively.

$$V_{DUT}(t) \times V_{ref}(t) = [A_o + A_n(t)]\cos\left(2\pi f_o t + [\theta(t) + \varphi_n(t)]\right) \times \cos\left(2\pi f_o t + \Phi_r(t)\right)$$

Equation 0-1

If the two signals are in phase ($\Phi_r(t) - \varphi_n(t) = 0$), this leads to:

$$V_{DUT}(t) \times V_{ref}(t) = \frac{[A_o + A_n(t)]}{2}\left[\cos(0) + \cos\left(4\pi f_o t + \Phi_r(t) + \varphi_n(t)\right)\right]$$

Equation 0-2

Leaving the higher frequency out, the DC signal is used as the source for amplitude noise measurements of the device under test.

Conversely, if the two signals are in quadrature ($\Phi_r(t) - \varphi_n(t) = \pi/2$), this results in:

$$V_{DUT}(t) \times V_{ref}(t) = \frac{[A_o + A_n(t)]}{2}\left[\sin(0) + \sin\left(4\pi f_o t + \Phi_r(t) + \varphi_n(t)\right)\right]$$

Equation 0-3

Leaving a DC signal which is close to zero, meaning that any contribution from the phase noise $\varphi_n(t)$ will be highly sensitive in the quadrature configuration, making this a way to measure phase noise. Nevertheless, as it is explored throughout this dissertation, there exist many other ways to measure phase noise.

Once the phase—and therefore the phase noise—of a signal is measured, a power spectral density (PSD) of the random phase fluctuations can be calculated, denoted by $S_\varphi(f)$. This power spectral density is often defined as a single-side band (SSB) PSD and has physical dimensions of rad^2/Hz [17].

Phase noise is defined by most manufacturers of instrumentation as $\mathcal{L}(f) = S_\varphi(f)/2$, usually given in the logarithmic scale. This provides a more technical definition of phase noise as "dB below the carrier in a 1 Hz bandwidth" [17].

$$\mathcal{L}(f) = 10\log\frac{1}{2}S_\varphi(f) \quad \left[\frac{dBc}{Hz}\right]$$

Equation 0-4

In other words, phase noise shows the representation of the quadrature noise power density relative to the carrier power at a given offset frequency defined by 1 Hz bandwidth. Figure 0-2 depicts this concept.

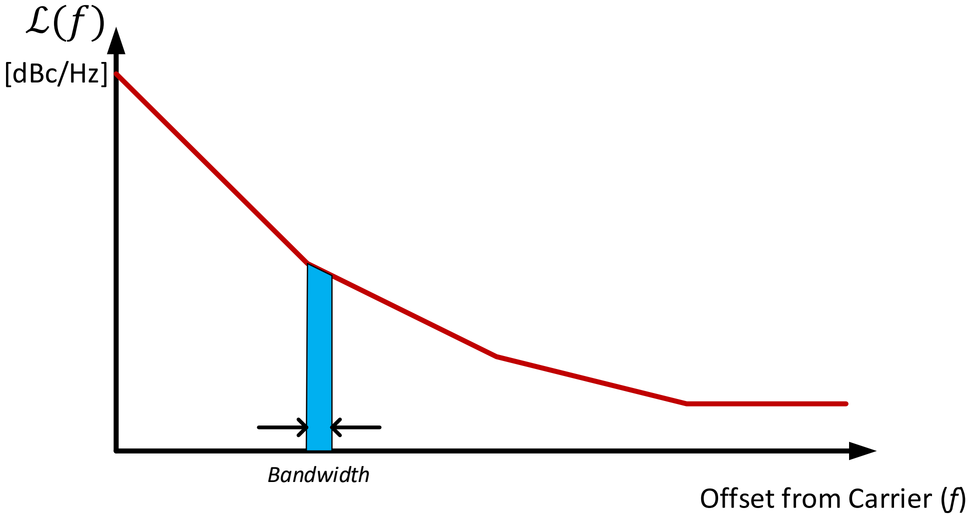

Figure 0-2. Phase noise spectrum as function of the offset frequency.

Key attributes of the phase noise spectrum are the close-in phase noise, which impacts signal purity in the vicinity of the carrier frequency and, therefore, affects both modulation accuracy and spectral integrity, and the far-out phase noise, which is found at some distance from the carrier and impacts applications such as adjacent channel interference and system sensitivity.

Moreover, timing jitter is introduced as a second figure of merit for stability characterization in a specified frequency range. While phase noise is primarily related to short-term stability, significant phase noise close to the carrier can slowly deteriorate long-term stability. In that case, timing jitter becomes relevant since it defines the expected time fluctuation at a given frequency offset, which can lead to frequency deviations in the oscillator.

Timing jitter is obtained by integrating the phase noise spectrum over a defined frequency interval. The timing jitter of an oscillator can be computed from Equation 0-5, by finding the root-mean-square value of the phase noise spectrum for the central frequency f_o at a certain measurement bandwidth $f_2 - f_1$:

$$\Delta t_{\mathrm{rms}} = \frac{1}{2\pi n f_o} \sqrt{\int_{f_1}^{f_2} \mathcal{L}(f)\,df} \qquad [\mathrm{s}]$$

Equation 0-5

A.2. PHASE NOISE INSTRUMENTATION FOR MICROWAVE OSCILLATORS

In microwave oscillators, the typical equipment used for measuring phase noise are spectrum analyzers and signal source analyzers. Although these instruments often appear similar and display results in comparable ways, there are key differences between them.

Spectrum analyzers are general-purpose instruments and have traditionally been used for phase noise measurements. The full spectrum measured by these devices is usually automated for phase noise measurement and often does not discriminate amplitude from phase noise.

On the other hand, signal source analyzers (SSA) are specialized instruments designed specifically for phase noise measurements. These analyzers typically offer higher speed and greater sensitivity compared to traditional spectrum analyzers and often come with a low-noise reference source that helps characterize most microwave signals. SSAs often come equipped with dual reference to make use of cross-correlation techniques, this increases their sensitivity for noise measurement. In this sense, for the characterization of ultra-low phase noise sources, it is imperative to use these types of devices for a higher timing sensitivity.

A.3. SIGNAL SOURCE ANALYZER: R&S®FSWP

The Rohde & Schwarz FSWP is a high-performance signal and spectrum analyzer designed for ultra-low phase noise measurements. It is widely used throughout the work in this dissertation so its key role as phase noise measurement tool was important to highlight in this section.

This device features an integrated cross-correlation technique, allowing for a highly sensitive and accurate phase noise characterization of external microwave and RF sources. This section describes the internal methodology used by the R&S®FSWP to measure the phase noise of an external oscillator or signal source [79].

A.3.1. Principle of Operation

The FSWP measures the phase noise of an external source by comparing it to an internal ultra-low-noise reference oscillator using a phase detector. The key steps in this process are detailed as follow based on the whitepaper [129]:

A. Down-conversion to Baseband

The external signal under test is first downconverted to a low intermediate frequency (IF) or baseband using a low-noise mixer. The reference signal for this downconversion is derived from an internal, ultra-low-noise synthesizer, which is locked to a stable frequency source.

B. Phase Detector Processing

The FSWP uses a phase detector to extract the phase difference between the external source and the internal reference. This phase difference is then converted into a baseband voltage signal, proportional to the phase deviation over time.

C. Cross-correlation Technique

To improve measurement sensitivity, the R&S®FSWP employs cross-correlation between two independent phase noise measurement channels. By averaging multiple independent measurements, uncorrelated noise is suppressed, allowing the system to reach sub-femtosecond phase noise sensitivity. This improves the sensitivity by as much as 25 dB, depending on the number of correlations used. The improvement that can be expected is: $\Delta L = 5 \log(n)$, where ΔL represents the improvement in phase noise sensitivity through cross-correlations (in dB) and n the number of correlations. This means that by increasing the number of correlations by a factor of 10, the phase noise of the R&S®FSWP can be reduced by 5 dB. Nevertheless, the analyzer's low-noise internal sources, often require only a few correlations to measure a high-quality oscillator.

D. FFT-Based Phase Noise Analysis

The baseband phase noise signal is analyzed in the frequency domain using an FFT (Fast Fourier Transform). This results in a phase noise PSD plot, typically displayed as SSB $L(f)$ in dBc/Hz.

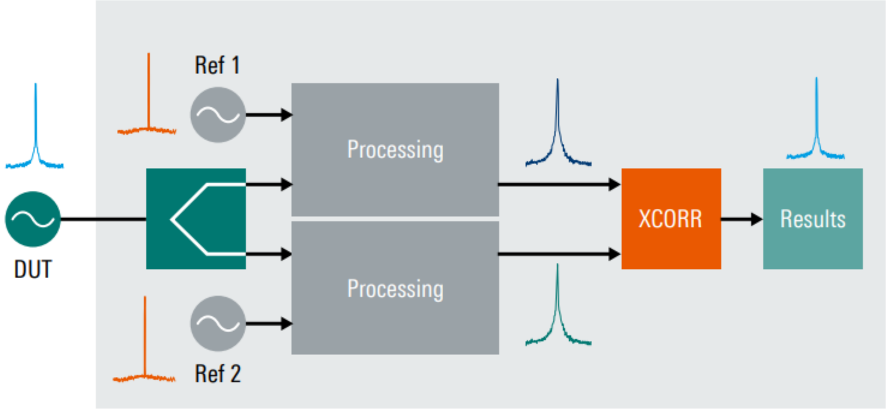

Figure 0-3. Phase noise measurement performed by FSWP using cross-correlations.

Taken from [129]

Figure 0-3 provides a general insight into the internal phase noise measurement scheme inside the FSWP as described before.

A.3.2. R&S®FSWP: Phase Noise Specifications

Figure 0-4 details typical sensitivities, or the noise floor, of the R&S®FSWP at different frequencies, for a single correlation setup.

Table A-1 summarizes the specific values for phase noise sensitivity at 10 GHz where most of the characterization measurements throughout this work are performed.

Table A-1. Phase noise sensitivity with R&S®FSWP (correlations = 1) for 10 GHz input.

RF Input	**Offset from carrier / Phase Noise (dBc/Hz)**										
	0.01Hz	**0.1Hz**	**1Hz**	**10Hz**	**100Hz**	**1kHz**	**10kHz**	**100kHz**	**1MHz**	**10MHz**	**30MHz**
10GHz	+20	-26	-55	-77	-100	-133	-152	-153	-157	-173	-175

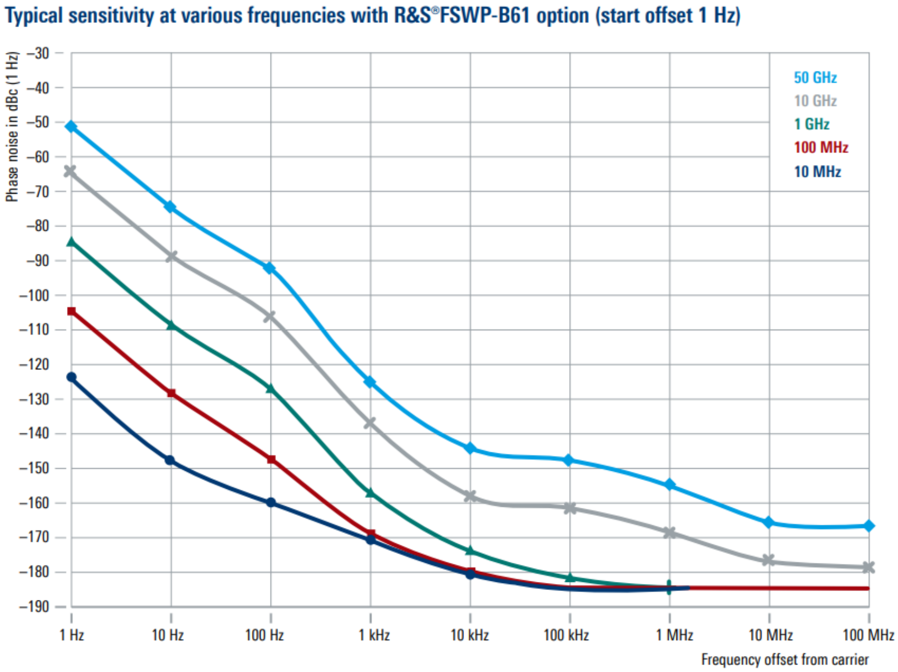

Figure 0-4. Noise floor for phase noise measurement using the R&S®FSWP Signal Source Analyzer at various carrier frequencies.

Taken from [79]

APPENDIX:

INSIGHTS ON MODE-LOCKED LASERS FOR PRESTO

B.1. NOISE IN MODE-LOCKED LASERS

Mode-locked lasers generate ultrashort pulses with stable repetition frequencies, but their performance is fundamentally affected by noise. This noise arises from various sources, including quantum fluctuations, pump laser noise, and environmental factors, leading to deviations in key laser parameters such as pulse timing, optical phase, pulse energy, and center frequency. These fluctuations, in turn, influence the offset and repetition frequencies of the emitted pulse train, which are crucial for applications such as the photonic microwave oscillator developed throughout this dissertation. This appendix manage to give a brief overview on the nature and effects of noise in mode-locked lasers based on [9], [110], [130]. Figure 0-1 shows a graphic representation of these processes and their interactions.

B.1.1. Quantum Noise and Spontaneous Emission

One of the primary noise sources in mode-locked lasers is quantum noise, primarily due to amplified spontaneous emission (ASE). This contributes to intensity and phase fluctuations. ASE affects both the timing jitter and frequency stability of the pulse train, introducing phase noise into the repetition rate and carrier-envelope offset frequency. ASE also couples into pulse energy fluctuations, which subsequently influence the center frequency through Raman scattering and other nonlinear interactions. Additionally, phase noise is impacted by the Kerr effect, which connects intensity variations to phase shifts via self-phase modulation (SPM), altering the optical phase and contributing to timing errors.

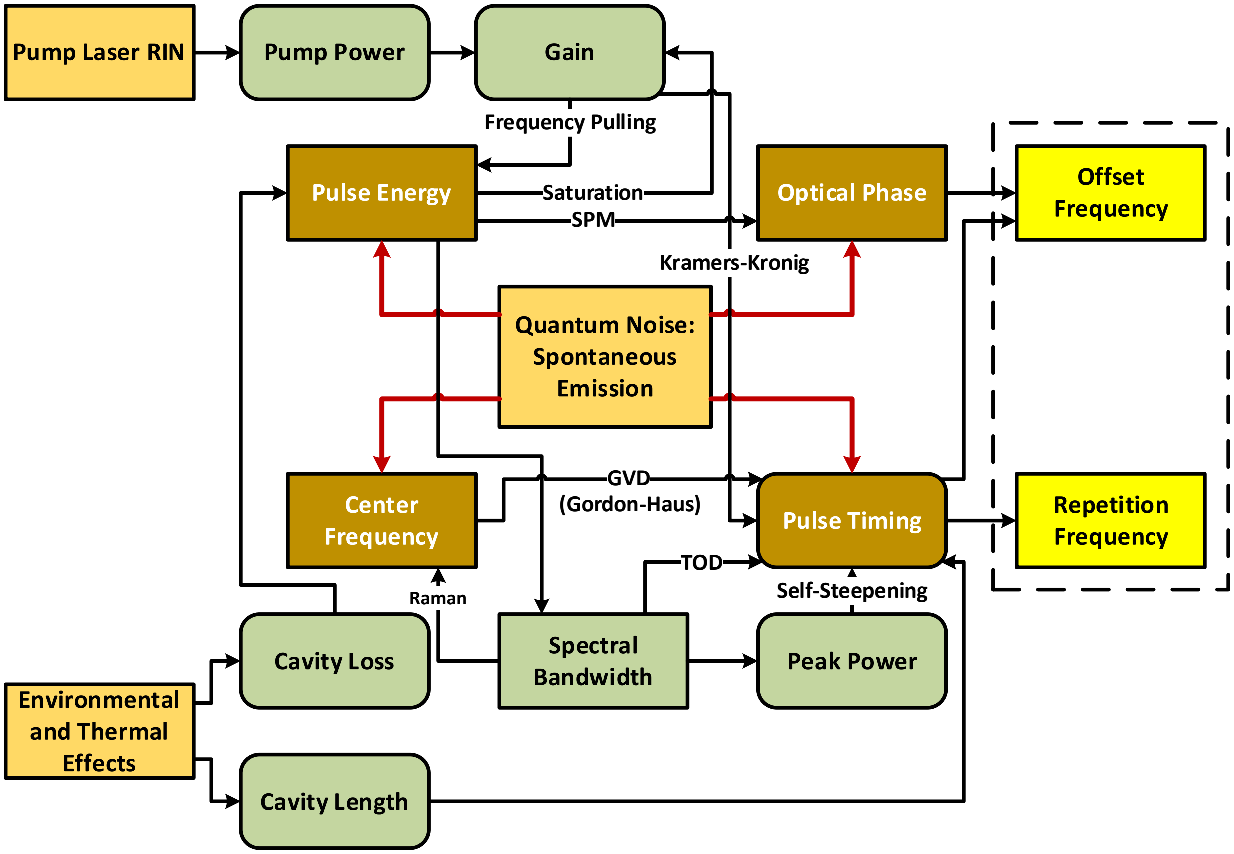

Figure 0-1. Schematic representation of noise sources, coupling mechanisms, and their effects in the timing of mode-locked lasers.

RIN: Relative intensity noise, GVD: Group velocity dispersion, TOD: Third-order dispersion, SPM: self-phase modulation

B.1.2. Timing Jitter and Gordon-Haus Effect

Timing jitter refers to random fluctuations in the arrival time of pulses. It arises due to frequency fluctuations, which affect the pulse propagation speed inside the laser cavity. The Gordon-Haus effect is a well-known mechanism by which frequency noise converts into timing jitter via group velocity dispersion (GVD).

When ASE induces random shifts in the pulse center frequency, the group delay dispersion alters the pulse timing from round trip to round trip, causing an accumulation of timing errors over many cycles. This effect is particularly significant in fiber-based mode-locked lasers, where long interaction lengths enhance dispersion-induced jitter.

B.1.3. Frequency Pulling and Repetition Rate Stability

Frequency pulling refers to the shift of the laser central frequency due to gain and loss interactions within the cavity. If the gain medium has a non-flat spectral response, the laser oscillation frequency drifts toward regions with higher gain. This effect couples with intensity noise and SPM, further impacting the optical phase and repetition frequency.

Repetition frequency fluctuations originate from both cavity length instabilities and nonlinear phase interactions. Cavity length variations, whether due to mechanical vibrations or thermal expansion, change the optical path length and shift the pulse repetition rate. The Kerr nonlinearity also introduces an intensity-dependent shift in the group velocity (self-steepening), which modifies the repetition frequency over time.

B.1.4. Optical Phase Noise and the Kramers-Kronig Relations

The optical phase is susceptible to various noise sources, particularly those influencing the refractive index and gain medium. The Kramers-Kronig relations dictate that any variation in gain will induce a corresponding change in refractive index, leading to frequency and phase noise.

In mode-locked lasers, optical phase noise is linked to pulse energy fluctuations via SPM and saturation effects. Gain saturation plays a critical role by limiting pulse amplification, thereby altering the carrier frequency and phase stability.

B.1.5. Environmental and Thermal Effects

Thermal fluctuations and mechanical vibrations in the laser cavity affect both the repetition frequency and center frequency. These changes alter the effective cavity length, introducing low-frequency noise components into the laser spectrum.

Additionally, environmental effects such as air pressure variations and temperature changes modulate the refractive index of optical components, affecting phase noise and timing jitter. These influences are particularly important for free-space mode-locked lasers, where beam alignment and cavity stability play crucial roles.

B.1.6. Offset and Repetition Frequency Control

The carrier-envelope offset (CEO) frequency and repetition frequency are the two defining parameters of an optical frequency comb. Noise in these frequencies originates from the coupling between timing jitter, pulse energy fluctuations, and optical phase noise.

To stabilize the CEO frequency, active feedback control is typically employed, using techniques like pump power modulation, cavity length adjustment, or extra-cavity actuators such as acousto-optic modulators (AOMs). Similarly, repetition rate stabilization relies on feedback loops that compensate for mechanical and environmental drifts.

B.1.7. Noise Suppression Techniques

To mitigate these noise sources, several strategies are employed:

- Active stabilization: Feedback systems actively correct frequency and timing errors by adjusting the cavity length or gain medium properties.
- Environmental isolation: Vibration and temperature control help minimize mechanical drifts and refractive index variations.
- Dispersion management: Optimized GVD compensation reduces the Gordon-Haus effect, improving long-term timing stability.
- Nonlinear phase compensation: Techniques such as saturable absorbers and Kerr-lens mode-locking minimize phase noise contributions from SPM and self-steepening.

B.2. MODE-LOCKED LASER CHARACTERISTICS

The following are the characteristics of the main commercial optical sources used along the work in the main scope of this dissertation, namely on the implementation and characterization of PRESTO.

B.2.1. MENHIR-1550 (SN 4409001)

This is the main laser used for most of the implementation throughout this work.

Table B-1. Specifications of main MENHIR-1550 laser for PRESTO.

Parameter	Min. Spec.	Specification	Max. Spec.	Unit
Repetition Rate	999.000	999.988	1001.000	MHz
Center Wavelength	1545	1564.0	1570	nm
Power at Main Output	40	44.5	–	mW
Optical Bandwidth	10	13.3	–	nm
Supported Pulse Width	–	194	250	fs
Output Pulse Width	–	511	1000	fs
Polarization (PER)	20	30		dB
Fine Tuning				
Sensitivity	100	146.7	–	Hz/V
Tuning Range	10000	13755	–	Hz
Slow Tuning				
Sensitivity	1000	1500	–	Hz/V
Tuning Range	100000	140000	–	Hz
Monitor Output Power	2	5	–	mW

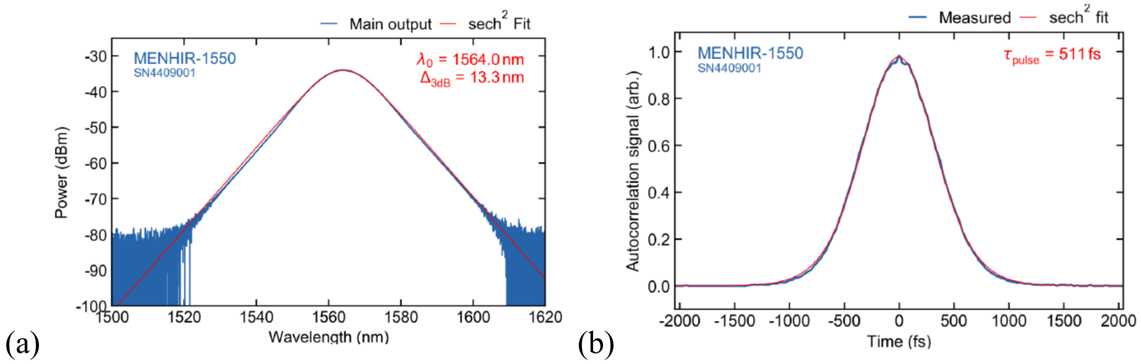

Figure 0-2. Mode-locked laser MENHIR-1550 (SN 4409001): (a) Optical power spectrum, (b) pulse shape and duration at the fiber output.

B.2.2. MENHIR-1550 (SN 4409002)

This is the backup laser, which is also used in the laser timing jitter characterization using BOC as shown in Section 3.1.2.

Table B-2. Specifications of backup MENHIR-1550 laser for laser characterization.

Parameter	**Min. Spec.**	**Specification**	**Max. Spec.**	**Unit**
Repetition Rate	999.000	999.995	1001.000	MHz
Center Wavelength	1545	1562.4	1570	nm
Power at Main Output	40	46.5	–	mW
Optical Bandwidth	10	11.4	–	nm
Supported Pulse Width	–	225	250	fs
Output Pulse Width	–	468	1000	fs
Polarization (PER)	20	28.5		dB
Fine Tuning				
Sensitivity	100	138.7	–	Hz/V
Tuning Range	10000	12978	–	Hz
Slow Tuning				
Sensitivity	1000	1481	–	Hz/V
Tuning Range	100000	139073	–	Hz
Monitor Output Power	2	5	–	mW

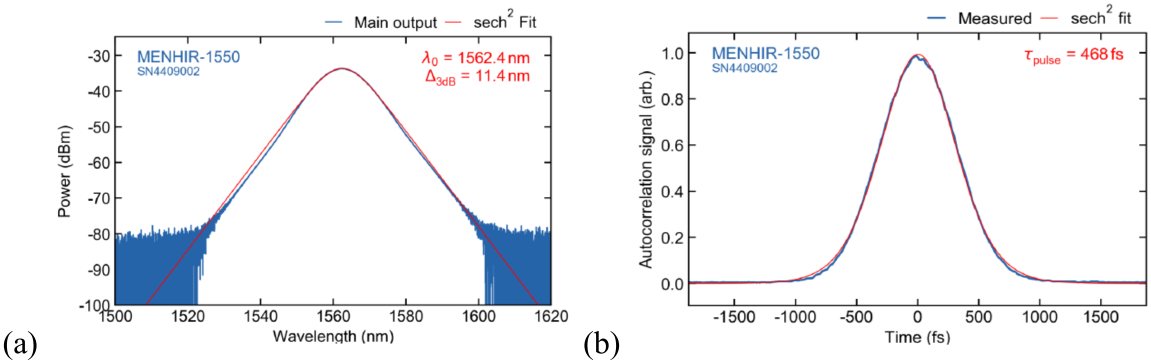

Figure 0-3. Mode-locked laser MENHIR-1550 (SN 4409002): (a) Optical power spectrum, (b) pulse shape and duration at the fiber output.

BIBLIOGRAPHY

[1] C. Rovelli, *El Orden del Tiempo*, 4th ed. 2020.

[2] S. Hawking, *A brief history of time*, Updated and Expanded tenth anniversary ed. New York: Bantam Books, 1998.

[3] P. Banerjee and D. Matsakis, *An Introduction to Modern Timekeeping and Time Transfer*. in Springer Series in Measurement Science and Technology. Cham: Springer Nature Switzerland, 2023. doi: 10.1007/978-3-031-30780-5.

[4] H. Margolis, "A brief history of timekeeping," *Phys. World*, vol. 31, no. 11, pp. 27–30, Nov. 2018, doi: 10.1088/2058-7058/31/11/36.

[5] M. A. Lombardi, T. P. Heavner, and S. R. Jefferts, "NIST Primary Frequency Standards and the Realization of the SI Second," *NCSLI Measure*, vol. 2, no. 4, pp. 74–89, Dec. 2007, doi: 10.1080/19315775.2007.11721402.

[6] T. P. Heavner *et al.*, "First accuracy evaluation of NIST-F2," *Metrologia*, vol. 51, no. 3, pp. 174–182, Jun. 2014, doi: 10.1088/0026-1394/51/3/174.

[7] "On the future redefinition of the second." [Online]. Available: https://www.bipm.org/en/cgpm-2022/resolution-5

[8] A. J. Benedick, J. G. Fujimoto, and F. X. Kärtner, "Optical flywheels with attosecond jitter," *Nature Photon*, vol. 6, no. 2, pp. 97–100, Feb. 2012, doi: 10.1038/nphoton.2011.326.

[9] M. Endo, T. D. Shoji, and T. R. Schibli, "Ultralow Noise Optical Frequency Combs," *IEEE J. Select. Topics Quantum Electron.*, vol. 24, no. 5, pp. 1–13, Sep. 2018, doi: 10.1109/JSTQE.2018.2818461.

[10] T. Fortier and E. Baumann, "20 years of developments in optical frequency comb technology and applications," *Commun Phys*, vol. 2, no. 1, p. 153, Dec. 2019, doi: 10.1038/s42005-019-0249-y.

[11] I. Ushijima, M. Takamoto, M. Das, T. Ohkubo, and H. Katori, "Cryogenic optical lattice clocks," *Nature Photon*, vol. 9, no. 3, pp. 185–189, Mar. 2015, doi: 10.1038/nphoton.2015.5.

[12] N. Huntemann, C. Sanner, B. Lipphardt, Chr. Tamm, and E. Peik, “Single-Ion Atomic Clock with 3 × 10 − 18 Systematic Uncertainty,” *Phys. Rev. Lett.*, vol. 116, no. 6, p. 063001, Feb. 2016, doi: 10.1103/PhysRevLett.116.063001.

[13] M. Schioppo *et al.*, “Ultrastable optical clock with two cold-atom ensembles,” *Nature Photon*, vol. 11, no. 1, pp. 48–52, Jan. 2017, doi: 10.1038/nphoton.2016.231.

[14] W. F. McGrew *et al.*, “Atomic clock performance enabling geodesy below the centimetre level,” *Nature*, vol. 564, no. 7734, pp. 87–90, Dec. 2018, doi: 10.1038/s41586-018-0738-2.

[15] S. M. Brewer *et al.*, “Al + 27 Quantum-Logic Clock with a Systematic Uncertainty below 10 − 18,” *Phys. Rev. Lett.*, vol. 123, no. 3, p. 033201, Jul. 2019, doi: 10.1103/PhysRevLett.123.033201.

[16] A. Aeppli, K. Kim, W. Warfield, M. S. Safronova, and J. Ye, “Clock with 8 × 10 − 19 Systematic Uncertainty,” *Phys. Rev. Lett.*, vol. 133, no. 2, p. 023401, Jul. 2024, doi: 10.1103/PhysRevLett.133.023401.

[17] E. Rubiola, *Phase Noise and Frequency Stability in Oscillators*, 1st ed. Cambridge University Press, 2008. doi: 10.1017/CBO9780511812798.

[18] E. Oelker *et al.*, “Demonstration of 4.8 × 10−17 stability at 1 s for two independent optical clocks,” *Nat. Photonics*, vol. 13, no. 10, pp. 714–719, Oct. 2019, doi: 10.1038/s41566-019-0493-4.

[19] M. Li, T. Hao, W. Li, and Y. Dai, “Tutorial on optoelectronic oscillators,” *APL Photonics*, 2021.

[20] L. Maleki, “The optoelectronic oscillator,” *Nature Photon*, vol. 5, no. 12, pp. 728–730, Dec. 2011, doi: 10.1038/nphoton.2011.293.

[21] Y. K. Chembo, D. Brunner, M. Jacquot, and L. Larger, “Optoelectronic oscillators with time-delayed feedback,” *Rev. Mod. Phys.*, vol. 91, no. 3, p. 035006, Sep. 2019, doi: 10.1103/RevModPhys.91.035006.

[22] D. Eliyahu, D. Seidel, and L. Maleki, “Phase noise of a high performance OEO and an ultra low noise floor cross-correlation microwave photonic homodyne system,” in *2008 IEEE*

International Frequency Control Symposium, Honolulu, HI: IEEE, May 2008, pp. 811–814. doi: 10.1109/FREQ.2008.4623111.

[23] H. Peng, N. Liu, and Z. Chen, "An ultra-low phase noise and spurs injection locked 10 GHz dual-loop optoelectronic oscillator," in *Sixth Symposium on Novel Optoelectronic Detection Technology and Applications*, H. Jiang and J. Chu, Eds., Beijing, China: SPIE, Apr. 2020, p. 383. doi: 10.1117/12.2565416.

[24] H. Peng, N. Liu, X. Xie, and Z. Chen, "Fast automatic frequency calibration assisted phase-locked highly stable optoelectronic oscillator," *Opt. Express*, vol. 29, no. 4, p. 6220, Feb. 2021, doi: 10.1364/OE.416336.

[25] J. Liu *et al.*, "Photonic microwave generation in the X- and K-band using integrated soliton microcombs," *Nat. Photonics*, vol. 14, no. 8, pp. 486–491, Aug. 2020, doi: 10.1038/s41566-020-0617-x.

[26] H. Shu *et al.*, "Microcomb-driven silicon photonic systems," *Nature*, vol. 605, no. 7910, pp. 457–463, May 2022, doi: 10.1038/s41586-022-04579-3.

[27] T. J. Kippenberg, A. L. Gaeta, M. Lipson, and M. L. Gorodetsky, "Dissipative Kerr solitons in optical microresonators," *Science*, vol. 361, no. 6402, p. eaan8083, Aug. 2018, doi: 10.1126/science.aan8083.

[28] I. Kudelin *et al.*, "Photonic chip-based low-noise microwave oscillator," *Nature*, vol. 627, no. 8004, pp. 534–539, Mar. 2024, doi: 10.1038/s41586-024-07058-z.

[29] J. Li, X. Yi, H. Lee, S. A. Diddams, and K. J. Vahala, "Electro-optical frequency division and stable microwave synthesis," *Science*, vol. 345, no. 6194, pp. 309–313, Jul. 2014, doi: 10.1126/science.1252909.

[30] J. Li and K. Vahala, "Small-sized, ultra-low phase noise photonic microwave oscillators at X-Ka bands," *Optica*, vol. 10, no. 1, p. 33, Jan. 2023, doi: 10.1364/OPTICA.477602.

[31] U. Keller, *Ultrafast Lasers: A Comprehensive Introduction to Fundamental Principles with Practical Applications*. in Graduate Texts in Physics. Cham: Springer International Publishing, 2021. doi: 10.1007/978-3-030-82532-4.

[32] S. A. Diddams, K. Vahala, and T. Udem, “Optical frequency combs: Coherently uniting the electromagnetic spectrum,” *Science*, vol. 369, no. 6501, p. eaay3676, Jul. 2020, doi: 10.1126/science.aay3676.

[33] T. Udem, R. Holzwarth, and T. W. Hänsch, “Optical frequency metrology,” vol. 416, 2002.

[34] F. Quinlan, “The Photodetection of Ultrashort Optical Pulse Trains for Low Noise Microwave Signal Generation,” *Laser & Photonics Reviews*, p. 2200773, Oct. 2023, doi: 10.1002/lpor.202200773.

[35] R. Ell *et al.*, “Generation of 5-fs pulses and octave-spanning spectra directly from a Ti:sapphire laser,” *Opt. Lett.*, vol. 26, no. 6, p. 373, Mar. 2001, doi: 10.1364/OL.26.000373.

[36] A. E. H. Oehler, M. C. Stumpf, S. Pekarek, T. Südmeyer, K. J. Weingarten, and U. Keller, “Picosecond diode-pumped 1.5 μm Er,Yb:glass lasers operating at 10–100 GHz repetition rate,” *Appl. Phys. B*, vol. 99, no. 1–2, pp. 53–62, Apr. 2010, doi: 10.1007/s00340-010-3912-2.

[37] H. Xu, Z. Li, P. Guo, L. Dan, and J. Zhao, “Sub-10-Attosecond Timing Jitter Mode-Locked Ti:sapphire Lasers,” in *2022 Joint Conference of the European Frequency and Time Forum and IEEE International Frequency Control Symposium (EFTF/IFCS)*, Paris, France: IEEE, Apr. 2022, pp. 1–2. doi: 10.1109/EFTF/IFCS54560.2022.9850870.

[38] N. V. Nardelli, H. Leopardi, T. R. Schibli, and T. M. Fortier, “Optical and Microwave Metrology at the 10^{-18} Level with an Er/Yb:glass Frequency Comb,” *Laser & Photonics Reviews*, vol. 17, no. 4, p. 2200650, Apr. 2023, doi: 10.1002/lpor.202200650.

[39] T. M. Fortier *et al.*, “Generation of ultrastable microwaves via optical frequency division,” *Nature Photon*, vol. 5, no. 7, pp. 425–429, Jul. 2011, doi: 10.1038/nphoton.2011.121.

[40] N. V. Nardelli *et al.*, “10 GHz generation with ultra-low phase noise via the transfer oscillator technique,” *APL Photonics*, vol. 7, no. 2, p. 026105, Feb. 2022, doi: 10.1063/5.0073843.

[41] M. Giunta *et al.*, “Compact and ultrastable photonic microwave oscillator,” *Opt. Lett.*, vol. 45, no. 5, p. 1140, Mar. 2020, doi: 10.1364/OL.385503.

[42] J. Yao *et al.*, “Optical-Clock-Based Time Scale,” *Phys. Rev. Applied*, vol. 12, no. 4, p. 044069, Oct. 2019, doi: 10.1103/PhysRevApplied.12.044069.

[43] H. Wiedemann, *Particle Accelerator Physics*. in Graduate Texts in Physics. Cham: Springer International Publishing, 2015. doi: 10.1007/978-3-319-18317-6.

[44] R. Appleby, G. Burt, J. Clarke, and H. Owen, *The Science and Technology of Particle Accelerators*, 1st ed. Boca Raton: CRC Press, 2020. doi: 10.1201/9781351007962.

[45] J. C. Bau, G. Daems, J. Lewis, and J. Philippe, "Managing the real-time behaviour of a particle beam factory: the CERN Proton Synchrotron complex and its timing system principles," *IEEE Trans. Nucl. Sci.*, vol. 45, no. 4, pp. 2004–2007, Aug. 1998, doi: 10.1109/23.710979.

[46] C. Pellegrini, A. Marinelli, and S. Reiche, "The physics of x-ray free-electron lasers," *Rev. Mod. Phys.*, vol. 88, no. 1, p. 015006, Mar. 2016, doi: 10.1103/RevModPhys.88.015006.

[47] E. Prat and S. Reiche, "Simple Method to Generate Terawatt-Attosecond X-Ray Free-Electron-Laser Pulses," *Phys. Rev. Lett.*, vol. 114, no. 24, p. 244801, Jun. 2015, doi: 10.1103/PhysRevLett.114.244801.

[48] C. Kupitz *et al.*, "Serial time-resolved crystallography of photosystem II using a femtosecond X-ray laser," *Nature*, vol. 513, no. 7517, pp. 261–265, Sep. 2014, doi: 10.1038/nature13453.

[49] S. M. Keable *et al.*, "Room temperature XFEL crystallography reveals asymmetry in the vicinity of the two phylloquinones in photosystem I," *Sci Rep*, vol. 11, no. 1, p. 21787, Nov. 2021, doi: 10.1038/s41598-021-00236-3.

[50] M. Xin, K. Şafak, and F. X. Kärtner, "Ultra-precise timing and synchronization for large-scale scientific instruments," *Optica*, vol. 5, no. 12, p. 1564, Dec. 2018, doi: 10.1364/OPTICA.5.001564.

[51] J.-F. Cliche and B. Shillue, "Applications of control Precision timing control for radioastronomy maintaining femtosecond synchronization in the atacama large millimeter array," *IEEE Control Syst.*, vol. 26, no. 1, pp. 19–26, Feb. 2006, doi: 10.1109/MCS.2006.1580149.

[52] H. Schuh and D. Behrend, "VLBI: A fascinating technique for geodesy and astrometry," *Journal of Geodynamics*, vol. 61, pp. 68–80, Oct. 2012, doi: 10.1016/j.jog.2012.07.007.

[53] L. I. Gurvits, "Space VLBI: from first ideas to operational missions," *Advances in Space Research*, vol. 65, no. 2, pp. 868–876, Jan. 2020, doi: 10.1016/j.asr.2019.05.042.

[54] L. I. Gurvits, “A Brief History of Space VLBI,” in *2023 8th IEEE History of Electrotechnology Conference (HISTELCON)*, Sep. 2023, pp. 171–174. doi: 10.1109/HISTELCON56357.2023.10365962.

[55] J. A. Scheer, “Coherent radar system performance estimation,” in *IEEE International Conference on Radar*, Arlington, VA, USA: IEEE, 1990, pp. 125–128. doi: 10.1109/RADAR.1990.201149.

[56] R. Li *et al.*, “Demonstration of a microwave photonic synthetic aperture radar based on photonic-assisted signal generation and stretch processing,” *Opt. Express*, vol. 25, no. 13, p. 14334, Jun. 2017, doi: 10.1364/OE.25.014334.

[57] F. Zhang *et al.*, “Photonics-based broadband radar for high-resolution and real-time inverse synthetic aperture imaging,” *Opt. Express*, vol. 25, no. 14, p. 16274, Jul. 2017, doi: 10.1364/OE.25.016274.

[58] S. Pan, “Microwave Photonic Radars,” *JOURNAL OF LIGHTWAVE TECHNOLOGY*, vol. 38, no. 19, 2020.

[59] R. Sahu, W. Hease, A. Rueda, G. Arnold, L. Qiu, and J. M. Fink, “Quantum-enabled operation of a microwave-optical interface,” *Nat Commun*, vol. 13, no. 1, p. 1276, Mar. 2022, doi: 10.1038/s41467-022-28924-2.

[60] F. Lecocq, F. Quinlan, K. Cicak, J. Aumentado, S. A. Diddams, and J. D. Teufel, “Control and readout of a superconducting qubit using a photonic link,” *Nature*, vol. 591, no. 7851, pp. 575–579, Mar. 2021, doi: 10.1038/s41586-021-03268-x.

[61] T. R. Schibli *et al.*, “Attosecond active synchronization of passively mode-locked lasers by balanced cross correlation,” *Opt. Lett.*, vol. 28, no. 11, p. 947, Jun. 2003, doi: 10.1364/OL.28.000947.

[62] L. A. Jiang, S. T. Wong, M. E. Grein, E. P. Ippen, and H. A. Haus, “Measuring timing jitter with optical cross correlations,” *IEEE J. Quantum Electron.*, vol. 38, no. 8, pp. 1047–1052, Aug. 2002, doi: 10.1109/JQE.2002.800993.

[63] J. Kim, J. Chen, J. Cox, and F. X. Kärtner, “Attosecond-resolution timing jitter characterization of free-running mode-locked lasers,” *Opt. Lett.*, vol. 32, no. 24, p. 3519, Dec. 2007, doi: 10.1364/OL.32.003519.

[64] K. Shafak, “Large-Scale L2RF Synchronization for Attosecond PS Facilities,” PhD Thesis, University of Hamburg, Hamburg, 2017.

[65] K. Şafak *et al.*, “Large-Scale Turnkey Timing Distribution System for Attosecond Photon Science Facilities,” in *Conference on Lasers and Electro-Optics*, San Jose, California: OSA, 2017, p. JTu4L.3. doi: 10.1364/CLEO_AT.2017.JTu4L.3.

[66] M. Xin *et al.*, “Breaking the Femtosecond Barrier in Multi-Kilometer Timing Synchronization Systems,” *IEEE J. Select. Topics Quantum Electron.*, vol. 23, no. 3, pp. 97–108, May 2017, doi: 10.1109/JSTQE.2016.2614676.

[67] H. P. H. Cheng *et al.*, “Commissioning of a Fully-Automated, Pulsed Optical Timing Distribution System at Dalian Coherent Light Source,” in *Conference on Lasers and Electro-Optics*, San Jose, California: OSA, 2018, p. JW2A.138. doi: 10.1364/CLEO_AT.2018.JW2A.138.

[68] M. Y. Peng, “Sub-Femtosecond Optical Timing Distribution for Next-Generation Light Sources.”

[69] M. Xin *et al.*, “Attosecond precision multi-kilometer laser-microwave network,” *Light Sci Appl*, vol. 6, no. 1, pp. e16187–e16187, Jul. 2016, doi: 10.1038/lsa.2016.187.

[70] P. T. Callahan, K. Safak, P. Battle, T. D. Roberts, and F. X. Kärtner, “Fiber-coupled balanced optical cross-correlator using PPKTP waveguides,” *Opt. Express*, vol. 22, no. 8, p. 9749, Apr. 2014, doi: 10.1364/OE.22.009749.

[71] K. Şafak, M. Xin, P. T. Callahan, M. Y. Peng, and F. X. Kärtner, “All fiber-coupled, long-term stable timing distribution for free-electron lasers with few-femtosecond jitter,” *Structural Dynamics*, vol. 2, no. 4, p. 041715, Jul. 2015, doi: 10.1063/1.4922747.

[72] J. Kim, F. X. Kärtner, and M. H. Perrott, “Femtosecond synchronization of radio frequency signals with optical pulse trains,” *Opt. Lett.*, vol. 29, no. 17, p. 2076, Sep. 2004, doi: 10.1364/OL.29.002076.

[73] J. Kim, F. X. Kärtner, and F. Ludwig, “Balanced optical-microwave phase detectors for optoelectronic phase-locked loops,” *Opt. Lett.*, vol. 31, no. 24, p. 3659, Dec. 2006, doi: 10.1364/OL.31.003659.

[74] K. J. Williams and R. D. Esman, “Nonlinearities in p-i-n microwave Photodetectors,” 1996.

[75] W. Zhang, T. Li, M. Lours, S. Seidelin, G. Santarelli, and Y. Le Coq, “Amplitude to phase conversion of InGaAs pin photo-diodes for femtosecond lasers microwave signal generation,” *Appl. Phys. B*, vol. 106, no. 2, pp. 301–308, Feb. 2012, doi: 10.1007/s00340-011-4710-1.

[76] R. P. Scott, C. Langrock, and B. H. Kolner, “High-dynamic-range laser amplitude and phase noise measurement techniques,” *IEEE J. Select. Topics Quantum Electron.*, vol. 7, no. 4, pp. 641–655, Sep. 2001, doi: 10.1109/2944.974236.

[77] M. Y. Peng, A. Kalaydzhyan, and F. X. Kärtner, “Balanced optical-microwave phase detector for sub-femtosecond optical-RF synchronization,” *Opt. Express*, vol. 22, no. 22, p. 27102, Nov. 2014, doi: 10.1364/OE.22.027102.

[78] M. Lessing, H. S. Margolis, C. T. A. Brown, P. Gill, and G. Marra, “Suppression of amplitude-to-phase noise conversion in balanced optical-microwave phase detectors,” *Opt. Express*, vol. 21, no. 22, p. 27057, Nov. 2013, doi: 10.1364/OE.21.027057.

[79] “R&S®FSWP PHASE NOISE ANALYZER AND VCO TESTER: Specifications.” [Online]. Available: https://scdn.rohde-schwarz.com/ur/pws/dl_downloads/pdm/cl_brochures_and_datasheets/specifications/3683_7719_22/FSWP_specs_en_3683-7719-22_v0600.pdf

[80] L. Kang and B. H. Kolner, “Characterization of AM-to-PM Conversion in Silicon p-i-n Photodiodes,” *IEEE Photon. Technol. Lett.*, vol. 31, no. 13, pp. 1001–1004, Jul. 2019, doi: 10.1109/LPT.2019.2914607.

[81] K. Jung and J. Kim, “Characterization of timing jitter spectra in free-running mode-locked lasers with 340 dB dynamic range over 10 decades of Fourier frequency,” *Opt. Lett.*, vol. 40, no. 3, p. 316, Feb. 2015, doi: 10.1364/OL.40.000316.

[82] D. Hou, C.-C. Lee, Z. Yang, and T. R. Schibli, “Timing jitter characterization of mode-locked lasers with <1 zs/√Hz resolution using a simple optical heterodyne technique,” *Opt. Lett.*, vol. 40, no. 13, p. 2985, Jul. 2015, doi: 10.1364/OL.40.002985.

[83] K. Şafak, M. Xin, Q. Zhang, S.-H. Chia, O. D. Mücke, and F. X. Kärtner, “Jitter analysis of timing-distribution and remote-laser synchronization systems,” *Opt. Express*, vol. 24, no. 19, p. 21752, Sep. 2016, doi: 10.1364/OE.24.021752.

[84] M. Xin, K. Şafak, M. Y. Peng, P. T. Callahan, and F. X. Kärtner, “One-femtosecond, long-term stable remote laser synchronization over a 35-km fiber link,” *Opt. Express*, vol. 22, no. 12, p. 14904, Jun. 2014, doi: 10.1364/OE.22.014904.

[85] E. Rubiola, E. Salik, S. Huang, N. Yu, and L. Maleki, “Photonic-delay technique for phase-noise measurement of microwave oscillators,” *J. Opt. Soc. Am. B*, vol. 22, no. 5, p. 987, May 2005, doi: 10.1364/JOSAB.22.000987.

[86] D. Kwon *et al.*, “Reference-free, high-resolution measurement method of timing jitter spectra of optical frequency combs,” *Sci Rep*, vol. 7, no. 1, p. 40917, Jan. 2017, doi: 10.1038/srep40917.

[87] K. Jung and J. Kim, “All-fibre photonic signal generator for attosecond timing and ultralow-noise microwave,” *Sci Rep*, vol. 5, no. 1, p. 16250, Nov. 2015, doi: 10.1038/srep16250.

[88] K. Şafak *et al.*, “Extreme-Timing-Resolution with Waveguide-Based Balanced Optical Cross-Correlators,” in *Conference on Lasers and Electro-Optics*, San Jose, California: Optica Publishing Group, 2022, p. STh5N.3. doi: 10.1364/CLEO_SI.2022.STh5N.3.

[89] B. E. A. Saleh and M. C. Teich, *Fundamentals of Photonics*, 1st ed. Wiley, 1991. doi: 10.1002/0471213748.

[90] F. Quinlan, T. M. Fortier, H. Jiang, and S. A. Diddams, “Analysis of shot noise in the detection of ultrashort optical pulse trains,” *J. Opt. Soc. Am. B*, vol. 30, no. 6, p. 1775, Jun. 2013, doi: 10.1364/JOSAB.30.001775.

[91] F. Quinlan *et al.*, “Exploiting shot noise correlations in the photodetection of ultrashort optical pulse trains,” *Nature Photon*, vol. 7, no. 4, pp. 290–293, Apr. 2013, doi: 10.1038/nphoton.2013.33.

[92] E. Rubiola, E. Salik, Nan Yu, and L. Maleki, “Flicker noise in high-speed p-i-n photodiodes,” *IEEE Trans. Microwave Theory Techn.*, vol. 54, no. 2, pp. 816–820, Feb. 2006, doi: 10.1109/TMTT.2005.863062.

[93] O. Llopis, S. Azaizia, K. Saleh, A. A. Slimane, and A. Fernandez, “Photodiode 1/f noise and other types of less known baseband noises in optical telecommunications devices,” in *2013 22nd International Conference on Noise and Fluctuations (ICNF)*, Montpellier, France: IEEE, Jun. 2013, pp. 1–4. doi: 10.1109/ICNF.2013.6579014.

[94] J. Kim and F. X. Kärtner, “Microwave signal extraction from femtosecond mode-locked lasers with attosecond relative timing drift,” *Opt. Lett.*, vol. 35, no. 12, p. 2022, Jun. 2010, doi: 10.1364/OL.35.002022.

[95] R. Bouchand, D. Nicolodi, X. Xie, C. Alexandre, and Y. Le Coq, “Accurate control of optoelectronic amplitude to phase noise conversion in photodetection of ultra-fast optical pulses,” *Opt. Express*, vol. 25, no. 11, p. 12268, May 2017, doi: 10.1364/OE.25.012268.

[96] Y. Hu *et al.*, “Computational Study of Amplitude-to-Phase Conversion in a Modified Unitraveling Carrier Photodetector,” *IEEE Photonics J.*, vol. 9, no. 2, pp. 1–11, Apr. 2017, doi: 10.1109/JPHOT.2017.2682251.

[97] X. Xie, J. Zang, A. Beling, and J. Campbell, “Characterization of Amplitude Noise to Phase Noise Conversion in Charge-Compensated Modified Unitravelling Carrier Photodiodes,” *J. Lightwave Technol.*, vol. 35, no. 9, pp. 1718–1724, May 2017, doi: 10.1109/JLT.2016.2641967.

[98] J. Davila-Rodriguez *et al.*, “Optimizing the linearity in high-speed photodiodes,” *Opt. Express*, vol. 26, no. 23, p. 30532, Nov. 2018, doi: 10.1364/OE.26.030532.

[99] F. J. Effenberger and A. M. Joshi, “Ultrafast, dual-depletion region, InGaAs/InP p-i-n detector,” *J. Lightwave Technol.*, vol. 14, no. 8, pp. 1859–1864, Aug. 1996, doi: 10.1109/50.532024.

[100] Y. Muramoto, Y. Hirota, K. Yoshino, H. Ito, and T. Ishibashi, “Uni-travelling-carrier photodiode module with bandwidth of 80 GHz,” *Electron. Lett.*, vol. 39, no. 25, pp. 1851–1852, Dec. 2003, doi: 10.1049/el:20031158.

[101] A. Beling, X. Xie, and J. C. Campbell, “High-power, high-linearity photodiodes,” *Optica*, vol. 3, no. 3, p. 328, Mar. 2016, doi: 10.1364/OPTICA.3.000328.

[102] Q. Li *et al.*, “High-Power Evanescently Coupled Waveguide MUTC Photodiode With >105-GHz Bandwidth,” *J. Lightwave Technol.*, vol. 35, no. 21, pp. 4752–4757, Nov. 2017, doi: 10.1109/JLT.2017.2759210.

[103] Z. Li, H. Pan, H. Chen, A. Beling, and J. C. Campbell, “High-Saturation-Current Modified Uni-Traveling-Carrier Photodiode With Cliff Layer,” *IEEE J. Quantum Electron.*, vol. 46, no. 5, pp. 626–632, May 2010, doi: 10.1109/JQE.2010.2046140.

[104] F. Quinlan *et al.*, “Optical amplification and pulse interleaving for low-noise photonic microwave generation,” *Opt. Lett.*, vol. 39, no. 6, p. 1581, Mar. 2014, doi: 10.1364/OL.39.001581.

[105] E. Portuondo-Campa, G. Buchs, S. Kundermann, L. Balet, and S. Lecomte, “Ultra-low phase-noise microwave generation using a diode-pumped solid-state laser based frequency comb and a polarization-maintaining pulse interleaver,” *Opt. Express*, vol. 23, no. 25, p. 32441, Dec. 2015, doi: 10.1364/OE.23.032441.

[106] M. Giunta, B. Rauf, A. Fricke, D. Schmidt, and R. Holzwarth, “10 GHz output signal from an optical clockwork supporting 10-20-level stability in 1000 s,” 2023.

[107] J. Kim, I. Jeon, D. Kim, and D. Kwon, “All-Fiber Photonic, Ultralow-Noise, Robust Optical and Microwave Signal Generators for FELs and UED,” *Proceedings of the 39th Free Electron Laser Conference*, vol. FEL2019, p. 3 pages, 1.467 MB, 2019, doi: 10.18429/JACOW-FEL2019-WEP030.

[108] J. Kim and D. Kwon, “Compact and Ultra-Stable Fiber-Photonic Stabilization Methods of Optical Frequency Combs,” in *2022 IEEE Photonics Society Summer Topicals Meeting Series (SUM)*, Cabo San Lucas, Mexico: IEEE, Jul. 2022, pp. 1–2. doi: 10.1109/SUM53465.2022.9858241.

[109] K. Shafak, A. Dai, and F. X. Kaertner, “Method and Apparatus for Controlling a Pulse Repetition Rate of a Pulsed Laser beam, and Pulsed Laser Oscillator with Stabilized Pulse Repetition Rate,” US 2022/0352687 A1

[110] H. A. Haus and A. Mecozzi, “Noise of mode-locked lasers,” *IEEE J. Quantum Electron.*, vol. 29, no. 3, pp. 983–996, Mar. 1993, doi: 10.1109/3.206583.

[111] T. Li *et al.*, “Low vibration sensitivity fiber spools for laser stabilization,” in *2011 Joint Conference of the IEEE International Frequency Control and the European Frequency and Time Forum (FCS) Proceedings*, San Francisco, CA, USA: IEEE, May 2011, pp. 1–3. doi: 10.1109/FCS.2011.5977897.

[112] S. Knudsen, A. B. Tveten, and A. Dandridge, “Measurements of fundamental thermal induced phase fluctuations in the fiber of a Sagnac interferometer,” *IEEE Photon. Technol. Lett.*, vol. 7, no. 1, pp. 90–92, Jan. 1995, doi: 10.1109/68.363366.

[113] J. Huang *et al.*, “Vibration-insensitive fiber spool for laser stabilization,” *Chin. Opt. Lett.*, vol. 17, no. 8, p. 081403, 2019, doi: 10.3788/COL201917.081403.

[114] B. Osunluk, S. Ogut, and E. Ozbay, “Thermally induced bias errors for a fiber coil with practical quadrupole winding,” in *2017 IEEE International Symposium on Inertial Sensors and Systems (INERTIAL)*, Kauai, HI, USA: IEEE, Mar. 2017, pp. 152–155. doi: 10.1109/ISISS.2017.7935682.

[115] S. Minakuchi *et al.*, “Thermal Strain in Lightweight Composite Fiber-Optic Gyroscope for Space Application,” *J. Lightwave Technol.*, vol. 33, no. 12, pp. 2658–2662, Jun. 2015, doi: 10.1109/JLT.2014.2375198.

[116] E. V. Dranitsyna, D. A. Egorov, A. A. Untilov, G. B. Deineka, I. A. Sharkov, and I. G. Deineka, “Reducing the effect of temperature variations on FOG output signal,” *Gyroscopy Navig.*, vol. 4, no. 2, pp. 92–98, Apr. 2013, doi: 10.1134/S2075108713020041.

[117] G. P. Agrawal, *Nonlinear fiber optics*, Sixth edition. London: Academic Press, an imprint of Elsevier, 2019.

[118] W. H. Glenn, “Noise in interferometric optical systems: an optical Nyquist theorem,” *IEEE J. Quantum Electron.*, vol. 25, no. 6, pp. 1218–1224, Jun. 1989, doi: 10.1109/3.29251.

[119] V. Michaud-Belleau *et al.*, “Fundamental thermal noise in antiresonant hollow-core fibers,” *Phys. Rev. A*, vol. 106, no. 2, p. 023501, Aug. 2022, doi: 10.1103/PhysRevA.106.023501.

[120] S. Foster, “Dynamical noise in single-mode distributed feedback fiber lasers,” *IEEE J. Quantum Electron.*, vol. 40, no. 9, pp. 1283–1293, Sep. 2004, doi: 10.1109/JQE.2004.833240.

[121] K. H. Wanser, “Fundamental phase noise limit in optical fibres due to temperature fluctuations,” *Electronics Letters*, vol. 28, no. 1, pp. 53–54, Jan. 1992, doi: 10.1049/el:19920033.

[122] Y. Li *et al.*, “Thermal phase noise in giant interferometric fiber optic gyroscopes,” *Opt. Express*, vol. 27, no. 10, p. 14121, May 2019, doi: 10.1364/OE.27.014121.

[123] L. Duan, “General treatment of the thermal noises in optical fibers,” *Phys. Rev. A*, vol. 86, no. 2, p. 023817, Aug. 2012, doi: 10.1103/PhysRevA.86.023817.

[124] S. Foster, “Low-frequency thermal noise in optical fiber cavities,” *Phys. Rev. A*, vol. 86, no. 4, p. 043801, Oct. 2012, doi: 10.1103/PhysRevA.86.043801.

[125] R. E. Bartolo, A. B. Tveten, and A. Dandridge, “Thermal Phase Noise Measurements in Optical Fiber Interferometers,” *IEEE J. Quantum Electron.*, vol. 48, no. 5, pp. 720–727, May 2012, doi: 10.1109/JQE.2012.2190717.

[126] J. Dong, J. Huang, T. Li, and L. Liu, “Observation of fundamental thermal noise in optical fibers down to infrasonic frequencies,” *Applied Physics Letters*, vol. 108, no. 2, p. 021108, Jan. 2016, doi: 10.1063/1.4939918.

[127] “G.652: Characteristics of a single-mode optical fiber and cable.” [Online]. Available: https://www.itu.int/rec/T-REC-G.652-201611-I/en

[128] D. Kwon and J. Kim, “All-fiber interferometer-based repetition-rate stabilization of mode-locked lasers to 10^−14-level frequency instability and 1-fs-level jitter over 1 s,” *Opt. Lett.*, vol. 42, no. 24, p. 5186, Dec. 2017, doi: 10.1364/OL.42.005186.

[129] P. Denisowski, “Understanding Phase Noise Measurement Techniques.” [Online]. Available: https://www.rohde-schwarz.com/us/products/test-and-measurement/analyzers/signal-spectrum-analyzers/white-paper-understanding-phase-noise-measurement-techniques-register_255398.html

[130] R. Paschotta, “Timing jitter and phase noise of mode-locked fiber lasers,” *Opt. Express*, vol. 18, no. 5, p. 5041, Mar. 2010, doi: 10.1364/OE.18.005041.